Cracking Behaviour of Glass Fibre-Reinforced Polymers under Combined Compression-Shear Cyclic Loading

by

Brent McCleave

A thesis

presented to the University of Waterloo

in fulfillment of the

thesis requirement for the degree of

Master of Applied Science

in

Mechanical and Mechatronics Engineering

Waterloo, Ontario, Canada, 2018

Author's Declaration

I hereby declare that I am the sole author of this thesis. This is a true copy of the thesis, including any required final revisions, as accepted by my examiners.

I understand that my thesis may be made electronically available to the public.

Abstract

A ply-level investigation into the cracking behaviour of E-glass/epoxy laminates under cyclic multiaxial loading was performed. Two laminate types were subjected to combined transverse compression-shear loading: multidirectional laminates with generalized layups $[0_2/\theta_2/0_2/-\theta_2]_S$ and tubular laminates with layup $[0_F/90]_S$. Unidirectional and woven prepregs were obtained from Composite Materials Italy and manufactured into panels and cylinders at the National Research Council in Ottawa, Ontario, Canada.

A series of quasistatic tests were performed to determine the in-plane strengths and elastic constants of the unidirectional lamina. From these data, multidirectional laminates $[0_2/\theta_2/0_2/-\theta_2]_S$ were designed such that their off-axis plies (θ, $-\theta$) experience identical biaxial states of stress as the transverse plies (90°) in the tubes by virtue of shear extension coupling.

Standard practises for specimen preparation and experimental setup were developed during this investigation. A method for preparing tubular specimens to prevent the application of bending loads during testing was established, along with the design and machining of fixtures for the same. Additionally, a method for visualizing the entire surface of the tubular specimens for crack initiation measurements was developed.

Three ratios of ply-level shear stress to transverse compressive stress were considered (0.00, 0.21, 0.40), each being studied between 60% and 80% of the nominal ultimate transverse compressive strength of the ply. Measurements of crack initiation (i.e. ply failure) lifetime were obtained by *in situ* optical visualization, wherein lighting apparatus were used to highlight sub-critical cracks within the semi-transparent composite specimens.

Several qualitative conclusions were established in this investigation. First and foremost, it was demonstrated that sub-critical cracks can be observed in compression-compression fatigue, and that the visibility of the cracks varies with the magnitudes of the combined load and torque. This contrasts with initial conjecture that compressed cracks would be invisible. Similarly, experimental results demonstrated that the stiffness of a laminate with compression cracks decreased over the lifetime of the specimen. Stress-life data indicated that as with tension-shear loading, the increasing presence of shear stress in compression-shear loading noticeably decreases the lifetime of a ply. It was also observed in initial tests that the combination of a multiaxial compressive stress state and the *in situ* constraining effects of adjacent plies within a laminate can increase the *in situ* transverse compressive strength and shear strength of a ply beyond is theoretical value by more than 50%.

Delays and experimental complications have prevented this investigation from being concluded presently, however the standard practises established in this investigation will aid the efforts by additional contributors to accomplish its objectives more quantitatively. The additional work required comprises two elements: the additional testing of specimens to obtain ply failure data and laminate stiffness degradation data, and the comparison of data obtained from the two different specimen types.

Acknowledgements

The writing of this thesis and the work it encompasses could not have been done without the support I received from mentors, friends and family.

My supervisors, Dr. John Montesano and Dr. Hamid Jahed, provided me with both their guidance and patience as I waded through the unfamiliar waters of experimentation.

Our collaborators at the National Research Council, Meysam Rahmat and Alex Naftel, were instrumental to this project for their manufacturing of the specimens used in this investigation.

Andrew Urschel, Brian Shuh, and Graeme Adair, the Engineering Machine Shop Technicians, were excellent mentors who helped hone my design and machining skills.

My parents, Anne and Michael McCleave, were incredibly supportive and reminded me that I do need to eat and sleep occasionally.

Finally, I owe special thanks to Noorin Samji, for her unending love, encouragement and patience over these long two years.

Table of Contents

List of Figures

List of Tables

List of Symbols

A, A_{ij}	Extensional stiffness matrix and its constituent elements [N/m]
B, B_{ij}	Coupling stiffness matrix and its constituent elements [N]
b	Width of a rectangular laminate beam [m]
C, C_{90}	Circumference of a laminate tube at radii R and R_{90}, respectively [m]
D, D_{ij}	Bending stiffness matrix and its constituent elements [N · m]
D^*, D^*_{ij}	Inverted bending stiffness matrix and its constituent elements [$(\mathrm{N} \cdot \mathrm{m})^{-1}$]
E	Elastic modulus of an isotropic material [Pa]
E_1, E_2, E_3	Extensional moduli of a lamina (in-plane longitudinal, in-plane transverse, out-of-plane transverse, respectively) [Pa]
F_{1C}	Ultimate longitudinal compressive strength [Pa]
F_{1T}	Ultimate longitudinal tensile strength [Pa]
F_{2C}	Ultimate transverse compressive strength [Pa]
F_{2T}	Ultimate transverse tensile strength [Pa]
F_6	Ultimate shear strength [Pa]
f_{img}, f_{load}	Frequencies of images capturing and cyclic loading, respectively [Hz]
G	Shear modulus of an isotropic material [Pa]
G_{12}, G_{13}, G_{23}	Shear moduli of a lamina (in-plane longitudinal, out-of-plane longitudinal, and out-of-plane transverse, respectively) [Pa]
$h_0 \dots h_k$	Ply boundary heights relative to laminate midplane [m]
I	Cross-sectional moment of inertia [m^4]
J	Polar moment of inertia [m^4]
K	Effective length parameter [ ]
k^0_x, k^0_y, k^0_{xy}	Laminate mid-plane curvatures [m^{-1}]
L	Laminate beam length [m]
M	Applied moment per unit width or circumference [N]
m	Tube buckling mode (number of axial half-waves) [ ]
N	Applied force per unit width or circumference [N/m]
N_C, N_R	Crack initiation lifetime and specimen rupture lifetimes [Cycles]
N_P	Normalized crack propagation lifetime [ ]

n	Tube buckling mode (number of circumferential waves) [ ]
P	Applied axial load [N]
P_{2C}, P_{2T}, P_6	Applied axial loads which induce ultimate stresses F_{2C}, F_{2T}, and F_6, respectively. [N]
Q, Q_{ij}	Reduced stiffness matrix and its constituent elements [Pa]
$\overline{Q}, \overline{Q}_{ij}$	Transformed reduced stiffness matrix and its constituent elements [Pa]
R, R_i, R_o	Mean, inner, and outer radii of tubular specimens [m]
R_{90}	Outermost radius of the 90° unidirectional plies in tubular specimens [m]
S_{22}, S_{33}, S_{23}	Hoop, axial, and in-plane shear stresses in the Abaqus tube model [Pa]
T	Applied torsion [N · m]
T_1, T_{1ij}	Ply stress transformation matrix and its constituent elements [ ]
T_2, T_{2ij}	Ply strain transformation matrix and its constituent elements [ ]
T_6	Applied torsion which induce static shear failure [N · m]
t	Laminate thickness [m]
t_{90}, t_f	Ply thickness in transverse and fabric plies in tubes, respectively [m]
$U_1 \ldots U_5$	Stiffness invariants [Pa]
V_F	Fibre volume fraction [%]
β	A tube buckling parameter in NASA paper [ ]
$\varepsilon_1,\ \varepsilon_2,\ \gamma_{12}$	Ply strain in the longitudinal, transverse, and shear directions [ ]
$\varepsilon_x^0,\ \varepsilon_y^0,\ \gamma_{xy}^0$	Mid-plane strains [ ]
$\sigma_x,\ \sigma_y,\ \sigma_{xy}$	Ply strain in the x, y and shear directions [ ]
ζ_1, ζ_2	Halpin-Tsai parameters [ ]
$\lambda_1,\ \lambda_2,\ \lambda_{12}$	Biaxiality ratios [ ]
μ	A tube buckling parameter in NASA paper [ ]
ν_{12}, ν_{21}	Major and minor Poisson's ratios [ ]
ρ	Radius between the centre of a circular cross-section and the location of shear stress evaluation [m]
$\sigma_1, \sigma_2, \sigma_6$	Ply stress in the longitudinal, transverse, and shear directions (superscript 0 and A indicate values of zero-degree and angled plies, respectively) [Pa]
$\sigma_x, \sigma_y, \sigma_{xy}$	Ply stress in the x, y and shear directions (superscript 0 and A indicate values of zero-degree and angled plies, respectively) [Pa]

1 Introduction

1.1 Project Background and Motivation

Composites are materials composed of multiple constituent materials which retain their individual properties, in contrast to homogenous-mixture materials such as alloys. They are heterogeneous (generally bi-phasic), containing a single continuous material (the *matrix*) which envelopes one or more dispersed materials (the *filler*). Fillers come in a variety of forms, including long and short fibres, spherical particles, or microscale platelets [1]. Reinforced concrete is an example of a composite material, wherein the natively poor tensile strength of concrete is improved by incorporating rebar, which endures the brunt of the applied tensile forces due to its high stiffness [2].

Fibre-reinforced polymers (FRPs) are a subtype of composite material, containing typically carbon (CFRPs), glass (GFRPs), or natural fibres (NFRPs) within a polymer matrix (either thermoset or thermoplastic) [1]. FRPs generally come in the form of individual plies, which are stacked on top of one another in a variety of orientations, forming multidirectional laminates. With the strength of the individual plies being greatest in the direction of the fibre orientation, the stacking of multiply-oriented plies gives the composite laminate high strength in a variety of directions.

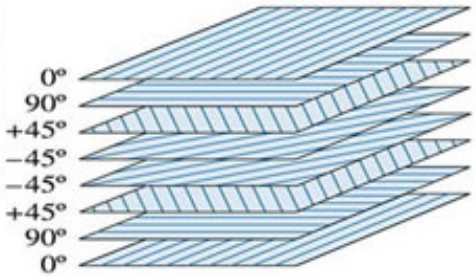

Figure 1. Stacking sequence of individual FRP plies within a laminate [3].

The high strength-to-weight ratio, excellent inherent fatigue properties and ability to tailor FRP composite materials for specific applications makes them attractive materials for primary structural applications. Historically, composites were used in lightweight structures such as hockey sticks and bicycles. More recently, composite materials have been incorporated into primary structural components, such as wind turbine blades [4]. Increasing regulations on vehicle fuel economy and greenhouse gas emissions such as the Corporate Average Fuel Economy (CAFE) standards have brought lightweight composite vehicle structures centre-stage [5]. Vehicles such as the high-performance McLaren 570S, the luxurious Aston Martin One-77, and the comparatively pedestrian BMW i3 feature carbon fibre monocoque designs to improve performance and fuel economy [6–8]. The Boeing 787 Dreamliner is approximately 50% composite by mass, primarily carbon fibre (Figure 2), making up most of the volume of the aircraft (excluding engines, rudders, and other miscellaneous components) [9].

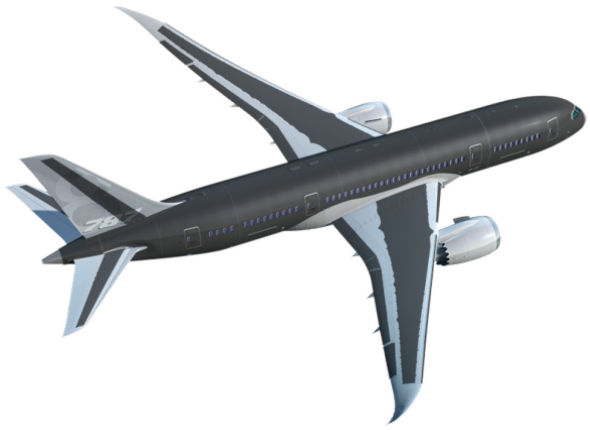

Figure 2. Distribution of carbon fibre laminates in the Boeing 787 Dreamliner (black) [9].

However, beyond their light weight and impressive properties, FRPs have disadvantages as well. Their complex structures and processing parameters require more advanced, labour-intensive, costly manufacturing methods. FRPs, especially carbon fibre, are very stiff and brittle, so the creation of complex components must involve methods beyond simple stamping, casting or forging. Because polymers cannot be welded, complex parts

must be produced using more complex single-component techniques, by using adhesives in place of welding, or using mechanical fasteners such as screws and rivets (provided that sufficient care is taken not the damage the laminate during drilling) [10]. Thermoplastic composites can be melted together into a single component, though this is not true of cured thermosets [11].

The complexities of designing FRP structures is another significant hurdle to their widespread use. Their microstructures, orthotropic behaviors, and the interactions of their constituent materials all complicate the design process. Without a thorough understanding of these elements, the development of robust predictive models is difficult, and results in conservative designs which ultimate increase the weight and cost of the structure [12]. This is especially significant in the case of fatigue loading, wherein even minute elements of a material's behavior can cause cumulative damage over a structure's lifetime.

Consequently, the overarching goal of research in the field of composites is to develop a thorough understanding of how they behave and understanding the mechanisms by which they fail. However, unlike with traditional structural materials (i.e. homogeneous, and typically isotropic materials such as alloys), the mechanical properties of FRP composites cannot easily be ascertained by standard testing procedures, which focus on entire laminates rather than individual plies. The problem can be summarized thusly:

> *The mechanical behaviour of a composite material tested in a particular configuration cannot be extrapolated to provide insight into either the behaviour of other composites in the same configuration, or the same composite in a different configuration.*

In order to develop high-fidelity models that can accurately predict the behaviour of composite laminate structures over their service lives, the underlying damage mechanisms of these materials must be understood. This includes studying the cumulative effects of the different components of multiaxial stresses, as well as their interactions. It is therefore critical to engage in a bottom-up approach to physical characterization, whereby observations on the microscale must be made to complement behaviour of FRPs on the macroscale. In this way, the macroscale behavior of a laminate can be deconvoluted into disparate elements that can each be studied and incorporated into predictive models.

One element that can be deconvoluted from macroscale FRP behaviour is the contribution of cyclic transverse compression to laminate failure. While individual FRP plies are strongest in the fibre direction, and stronger still in fibre-direction tension than in compression, FRP laminates comprise stacks of arbitrarily-oriented plies, whose orientations relative to applied loads can introduce transverse compressive stresses within those plies. Consequently, it is desirable to investigate the mechanisms of transverse compression on ply failure, since damage – and ultimately the cascading failure of individual plies – ultimately leads to laminate structure failure.

The study of composite materials in compressive stress modes, especially transverse compressive stress modes, is limited in the literature. There are a variety of experimental complications which reduce the prevalence of experimental compressive studies. Examples include the design of specimens and fixtures to prevent buckling, and the non-linearity of some materials in compression [13]. Additionally, the sensitivity of laminate behaviour to voids, fibre misalignments and other defects is noticeably greater in compression than in tension [14].

Consequently, this experimental investigation was performed to begin filling in the gaps present in the literature, so that the contributions of transverse compression to ply failure can be incorporated into high-fidelity models of laminate structures.

1.2 Research Objective

The goal of this work is to study the fatigue behaviour of GFRP composite laminates under combined transverse compression-shear loading, with the focus being on the characteristic cracking behaviour of the individual plies through an experimental test program. This goal can be subdivided into four primary objectives. The first objective is to characterize the stress-life behaviour of individual plies within a laminate, which varies depending on the states of cyclic multiaxial stress the plies experience. Second, the mechanisms of damage must be evaluated, specifically the initiation, propagation, and multiplication of cracks within a ply during cyclic loading. Third, the effects of damage on the degradation of overall laminate stiffness must be characterized. The final objective is to determine the effects of specimen geometry on damage behaviour (including factors such as ply thickness, ply curvature, and the orientation of the cracked ply or its adjacent plies).

With the study of compressive crack behaviour being something of a novelty in the literature, an additional objective of this research is to establish standard methods to carry out such an investigation. This includes the design of specimens and testing methods to introduce desired states of stress, the consideration of testing apparatus required, and the methods to characterize damage under combined compression and shear.

1.3 Project Outline and Scope

The evaluation of ply failure under a given stress state will be carried out in two different types of GFRP laminates. Tubular specimens will be compressed and twisted to introduce specific ratios of transverse compressive stress and shear stress. Flat coupons with angled internal plies will be axially compressed, introducing the same predetermined ratio of stresses in their off-axis plies. Due to the translucency of GFRPs, the initiation of ply cracks will be performed visually, using cameras and a lighting apparatus which highlights cracks within the semi-transparent material. A comparison of cracking behavior between the two specimen types can be made to determine any geometric effects on ply failure, such as the curvature of the laminate, the effects of neighbouring ply orientation, or the effects of ply thickness.

2 Theoretical Background and Literature Review

2.1 Overview of Composite Laminate Behaviour

The behaviour of the composite laminates in this investigation were modelled analytically using Classical Laminate Theory, wherein the behaviour of an entire laminate stack is modelled as a system of linear equations, each describing a single Hookean ply, or *lamina*. Section 2.1.1 details the theory and its physical bases, and Section 2.1.2 discusses the nature of multiaxial states of plane stress within an arbitrary laminate. The application of this model to the specific laminates considered in this investigation is discussed at length in Chapter 3.

2.1.1 Classical Laminate Theory

2.1.1.1 Lamina Properties

The basis of a laminate is an individual lamina. Figure 3 illustrates an arbitrary plane stress state on an orthotropic lamina, as well as the local and global coordinate systems considered in the laminate analysis.

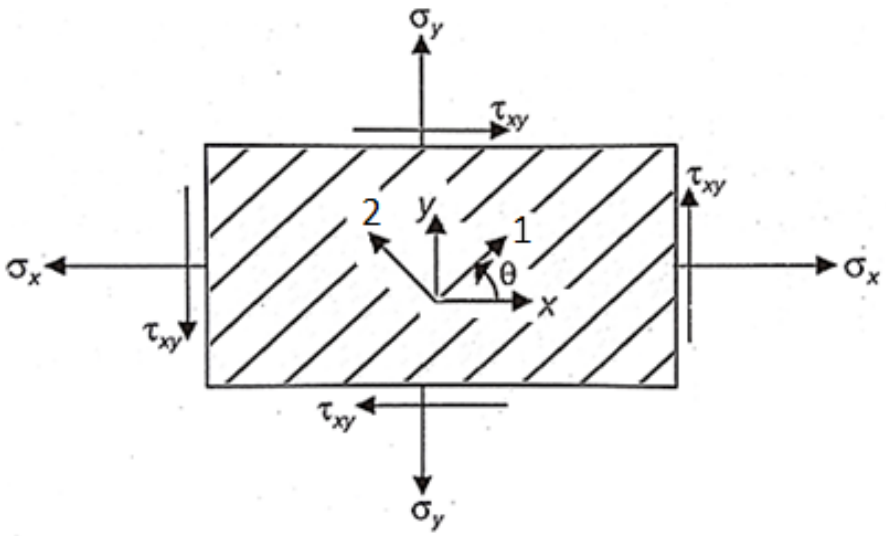

Figure 3. Plane stress in a generally orthotropic lamina [1].

In the case of a simple unidirectionally-loaded lamina, an external load is applied on the universal x or y axis, while stresses and strains are calculated along the local fibre axes L and T (longitudinal and transverse directions, relative to the fibre direction). In this report, all direction-dependant notation referring to the longitudinal and transverse directions will use subscript 1 and 2 respectively (e.g. the longitudinal extensional modulus E_1, or transverse ply stress σ_2). Similarly, the in-plane shear "direction" within the local coordinate system will be referenced using a subscript 12 or 6 (e.g. shear modulus G_{12} or shear stress σ_6). In the universal coordinate system, shear will be referred to using a subscript xy. Notation with subscript 3 refers to out-of-plane values (e.g. out-of-plane extensional modulus E_3).

The material properties of a unidirectional continuous fibre-reinforced composite can be calculated using the elastic properties of its constituent materials and their respective volume fractions. In the case of the longitudinal modulus and major Poisson's ratio, a weighted average (referred to as the *rule of mixtures*) accurately predicts the properties of a composite, while semi-empirical formulas developed by Halpin and Tsai are required to accurately determine the transverse and shear moduli [1].

$$E_1 = E_f V_f + E_m V_m \tag{1}$$

$$E_2 = E_m \left(\frac{1 + \zeta_1 \eta_1 V_f}{1 - \eta_1 V_f} \right) \qquad \eta_1 = \frac{E_f - E_m}{E_f + \zeta_1 E_m} \qquad \zeta_1 = 2\frac{a}{b} \tag{2}$$

$$G_6 = G_m \left(\frac{1 + \zeta_2 \eta_2 V_f}{1 - \eta_2 V_f} \right) \qquad \eta_2 = \frac{G_f - G_m}{G_f + \zeta_2 G_m} \qquad \zeta_2 = 1 \tag{3}$$

$$\nu_{12} = \nu_f V_f + \nu_m V_m \tag{4}$$

$$\nu_{21} = \nu_{12} \frac{E_2}{E_1} \tag{5}$$

where E, G, ν, and V are the directional moduli, shear moduli, Poisson's ratio and volume fraction of the matrix (subscript m) and fibres (subscript f) respectively. The parameter ζ_1 is a measure of fibre geometry, where a/b is the cross-sectional aspect ratio of the fibres (assumed to be 1 for perfectly cylindrical fibres with circular cross-sections). The parameter ζ_2 is an empirical constant not directly correlated with any physical characteristic of the composite.

Classical laminate theory makes the following assumptions:

- The matrix and fibres are isotropic
- The matrix and fibres are perfectly bonded
- There is no intermediate layer at the fibre-matrix boundary
- The fibres are uniformly distributed within the matrix
- The fibres are perfectly cylindrical ($\zeta_1 = 2$)
- There are no matrix voids or other defects in the constituent materials
- The behaviour of the lamina and its constituent materials is within the linear-elastic regime
- Moduli exhibit the same value in compression and tension
- The laminate is a thin rectangular plate with uniform thickness.

The reduced stiffness matrix Q represents the properties of a given ply within its own local coordinate system. Consequently, Q is the same for all plies comprising the same material, regardless of orientation.

$$Q_{ij} = \begin{bmatrix} Q_{11} & Q_{12} & 0 \\ Q_{12} & Q_{22} & 0 \\ 0 & 0 & Q_{66} \end{bmatrix} \tag{6}$$

$$Q_{11} = \frac{E_1}{1 - \nu_{12}\nu_{21}}$$

$$Q_{22} = \frac{E_2}{1 - \nu_{12}\nu_{21}}$$

$$Q_{12} = \frac{\nu_{12}E_2}{1 - \nu_{12}\nu_{21}}$$

$$Q_{66} = G_{12}$$

The transformed reduced stiffness matrix $\overline{Q}$ represents the stiffness of a given ply in at an arbitrary angle θ relative to an existing universal axis.

$$\overline{Q}_{ij} = \begin{bmatrix} \overline{Q}_{11} & \overline{Q}_{12} & \overline{Q}_{16} \\ \overline{Q}_{12} & \overline{Q}_{22} & \overline{Q}_{26} \\ \overline{Q}_{16} & \overline{Q}_{26} & \overline{Q}_{66} \end{bmatrix} \tag{7}$$

The $\overline{Q}$ matrix can be calculated with an extensive series of calculations [1], though was rederived by Tsai and Pagano using a series of stiffness invariants U, which reduce the complexity of calculating $\overline{Q}$ for numerous angles [15]:

$$\bar{Q}_{11} = U_1 + U_2 \cos 2\theta + U_3 \cos 4\theta \tag{8}$$

$$\bar{Q}_{12} = \ U_4 - U_3 \cos 4\theta$$

$$\bar{Q}_{22} = U_1 - U_2 \cos 2\theta + U_3 \cos 4\theta$$

$$\bar{Q}_{16} = \frac{1}{2} U_2 \sin 2\theta + U_3 \sin 4\theta$$

$$\bar{Q}_{26} = \ \frac{1}{2} U_2 \sin 2\theta - U_3 \sin 4\theta$$

$$\bar{Q}_{66} = U_5 - U_3 \cos 4\theta$$

$$U_1 = \frac{3Q_{11} + 3Q_{22} + 2Q_{12} + 4Q_{66}}{8}$$

$$U_2 = \frac{Q_{11} - Q_{22}}{2}$$

$$U_3 = \frac{Q_{11} + Q_{22} - 2Q_{12} - 4Q_{66}}{8}$$

$$U_4 = \frac{Q_{11} + Q_{22} + 6Q_{12} - 4Q_{66}}{8}$$

$$U_5 = \frac{Q_{11} + Q_{22} - 2Q_{12} + 4Q_{66}}{8}$$

The $\bar{Q}_{16}$ and $\bar{Q}_{26}$ correspond to shear extension coupling, wherein a ply will experience shear due off-axis loading of the specimen (the orientation of the fibres relative to the direction of loading). The terms $\bar{Q}_{16}$ and $\bar{Q}_{26}$ will therefore be 0 in the 0° and 90° plies, and non-zero in all off-axis plies. However, in an angled ply, the stiffness values $\bar{Q}_{16}$ and $\bar{Q}_{26}$ of that ply change with its angle, resulting in changing values of shear stress based on arbitrary longitudinal or transverse compressive strain, respectively. Consequently, the force applied to the laminate introduces transverse compressive stress to the off-axis ply via its $\bar{Q}_{12}$ and $\bar{Q}_{22}$ stiffness terms, and additionally introduces shear stress via its $\bar{Q}_{16}$ and $\bar{Q}_{26}$ stiffness terms.

2.1.1.2 Laminate Properties

The properties of a laminate can be calculated using the elastic properties and stacking order, or *layup*, of its constituent plies. The layup of a laminate describes the orientation of a laminate's plies relative to the direction in which the laminate is loaded. The Classical Laminate Theory framework is sufficiently general to describe laminates containing multiple materials with multiple ply thicknesses.

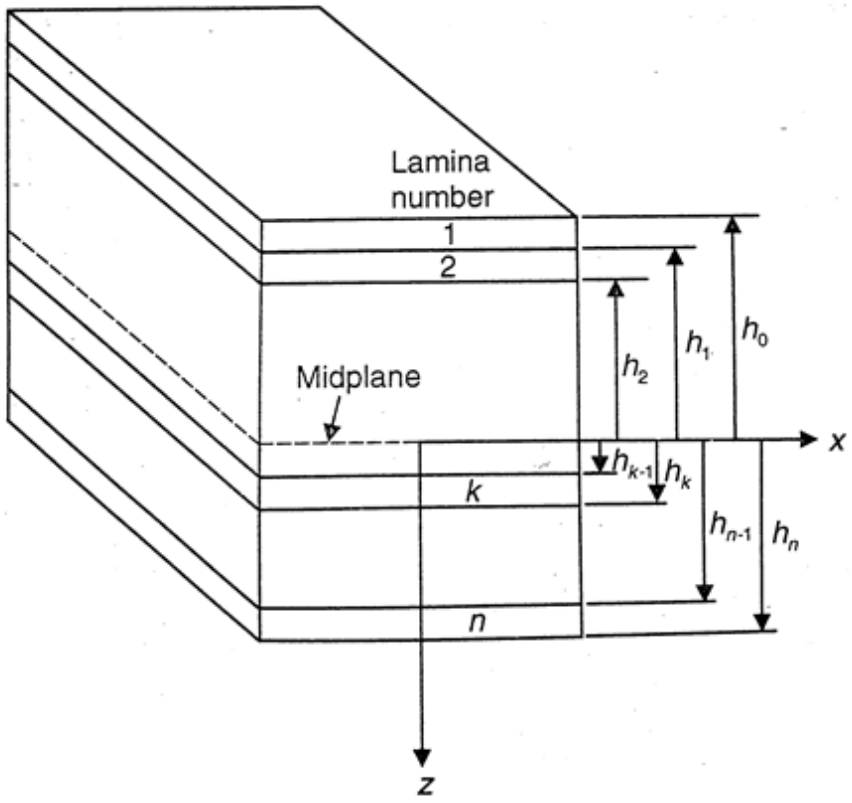

Figure 4. Geometry of an arbitrary laminate [1].

The stiffness matrices A, D, and B of a fibre-reinforced laminate correspond to the extensional stiffness of the laminate against in-plane stresses, the bending stiffness of the laminate against out-of-plane moments, and the coupling of in-plane and out-of-plane stresses respectively. In symmetric laminates such as those considered in this investigation, $B_{ij} = 0$.

$$A_{ij} = \sum_{k=1}^{n} \left[\bar{Q}_{ij}\right]_k (h_k - h_{k-1}) \tag{9}$$

$$B_{ij} = \frac{1}{2} \sum_{k=1}^{n} \left[\bar{Q}_{ij}\right]_k (h_k^2 - h_{k-1}^2) \tag{10}$$

$$D_{ij} = \frac{1}{3} \sum_{k=1}^{n} \left[\bar{Q}_{ij}\right]_k (h_k^3 - h_{k-1}^3) \tag{11}$$

The A, D, and B matrices are typically combined into a single stiffness matrix describing all the constitutive equations that govern the stress-strain behaviour of a laminate.

$$\begin{Bmatrix} N \\ M \end{Bmatrix} = \begin{bmatrix} A & B \\ B & D \end{bmatrix} \begin{Bmatrix} \varepsilon^0 \\ k^0 \end{Bmatrix} \tag{12}$$

where N and M are applied forces and moments per unit width of the specimen (or per unit circumference in the case of the tubular specimens), ε^0 are midplane strains, and k^0 are the midplane curvatures as defined below:

$$N = \begin{bmatrix} N_x \\ N_y \\ N_{xy} \end{bmatrix} \qquad N_x = \int_{-\frac{h}{2}}^{\frac{h}{2}} \sigma_x dz \qquad N_y = \int_{-\frac{h}{2}}^{\frac{h}{2}} \sigma_y dz \qquad N_{xy} = \int_{-\frac{h}{2}}^{\frac{h}{2}} \sigma_{xy} dz \tag{13}$$

$$M = \begin{bmatrix} M_x \\ M_y \\ M_{xy} \end{bmatrix} \qquad M_x = \int_{-\frac{h}{2}}^{\frac{h}{2}} \sigma_x z dz \qquad M_y = \int_{-\frac{h}{2}}^{\frac{h}{2}} \sigma_y z dz \qquad M_{xy} = \int_{-\frac{h}{2}}^{\frac{h}{2}} \sigma_{xy} z dz \tag{14}$$

$$\begin{Bmatrix} \varepsilon_x^0 \\ \varepsilon_y^0 \\ \varepsilon_{xy}^0 \end{Bmatrix} = \begin{Bmatrix} \dfrac{\partial u_o}{\partial x} \\ \dfrac{\partial v_o}{\partial y} \\ \dfrac{\partial u_o}{\partial y} + \dfrac{\partial v_o}{\partial x} \end{Bmatrix} \qquad \begin{Bmatrix} k_x^0 \\ k_y^0 \\ k_{xy}^0 \end{Bmatrix} = - \begin{Bmatrix} \dfrac{\partial^2 w_o}{\partial x^2} \\ \dfrac{\partial^2 w_o}{\partial y^2} \\ 2\dfrac{\partial^2 w_o}{\partial x \partial y} \end{Bmatrix} \tag{15}$$

where u_0, v_0, and w_0 are midplane displacements in the x, y, and z directions respectively, as shown in Figure 5, which illustrates the out-of-plane bending deformation of a laminate.

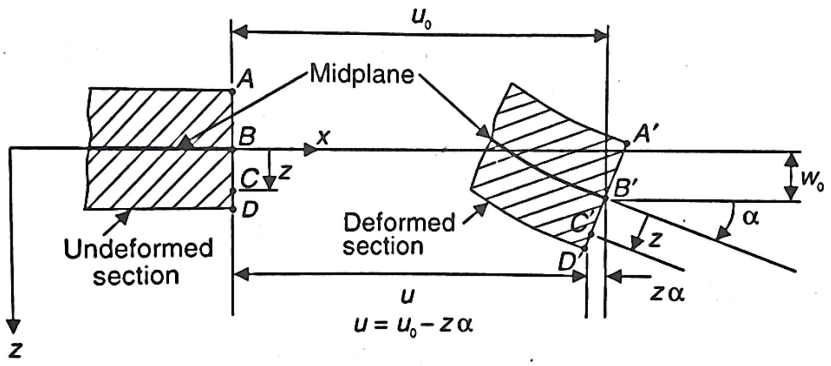

Figure 5. Deformation of a plane in the *xz* plane [1].

From the definitions of midplane strain and curvature, the final expressions for in-plane strains and stresses of any arbitrary ply k within a laminate can be determined, and incorporated into the constitutive stress-strain equation for a classical laminate.

$$\begin{Bmatrix} \varepsilon_x \\ \varepsilon_y \\ \varepsilon_{xy} \end{Bmatrix} = \begin{Bmatrix} \varepsilon_x^0 \\ \varepsilon_y^0 \\ \varepsilon_{xy}^0 \end{Bmatrix} + z \begin{Bmatrix} k_x^0 \\ k_y^0 \\ k_{xy}^0 \end{Bmatrix} \tag{16}$$

$$\begin{Bmatrix} \sigma_x \\ \sigma_y \\ \sigma_{xy} \end{Bmatrix}_k = \left[\bar{Q}\right]_k \begin{Bmatrix} \varepsilon_x \\ \varepsilon_y \\ \varepsilon_{xy} \end{Bmatrix}_k \tag{17}$$

$$\begin{Bmatrix} \sigma_1 \\ \sigma_2 \\ \sigma_6 \end{Bmatrix}_k = [T_1]_k \begin{Bmatrix} \sigma_x \\ \sigma_y \\ \sigma_{xy} \end{Bmatrix}_k \tag{18}$$

$$\begin{Bmatrix} \varepsilon_1 \\ \varepsilon_2 \\ \gamma_{12} \end{Bmatrix}_k = [T_2]_k \begin{Bmatrix} \varepsilon_x \\ \varepsilon_y \\ \gamma_{xy} \end{Bmatrix}_k \tag{19}$$

where T_1 and T_2 are the stress and strain transformation matrices, respectively, defined below:

$$T_1 = \begin{bmatrix} \cos\theta & \sin\theta & 2\sin\theta\cos\theta \\ \sin\theta & \cos\theta & -2\sin\theta\cos\theta \\ -\sin\theta\cos\theta & \sin\theta\cos\theta & cos^2\,\theta - \sin^2\theta \end{bmatrix} \tag{20}$$

$$T_2 = \begin{bmatrix} \cos\theta & \sin\theta & \sin\theta\cos\theta \\ \sin\theta & \cos\theta & -\sin\theta\cos\theta \\ -2\sin\theta\cos\theta & 2\sin\theta\cos\theta & cos^2\,\theta - \sin^2\theta \end{bmatrix} \tag{21}$$

2.1.2 Ply-level Stress States

This investigation aims to study the effects of specific stress states in both flat and tubular laminate specimens. A combination of transverse compressive stress and shear stress can be applied to a tube by means of combined axial and torsional loading. However, without complex equipment and fixtures, rectangular laminates can only be loaded axially. Consequently, the loading of rectangular laminates must employ *shear extension coupling*, a mechanism which introduces internal shear stresses into an off-axis ply based on its relative orientation to the direction of loading (see Section 2.1.1.1)

For a laminate with layup $[0/\theta_2/0/-\theta_2]_S$, Figure 6 illustrates normalized values of longitudinal, transverse and shear stresses within an off-axis ply subjected to an arbitrary compressive stress σ_x. Within a given ply in a laminate, a state of stress can be conveniently defined as a ratio of the various in-plane stresses the ply experiences, referred to as a *biaxiality ratios*:

$$\lambda_1 = \frac{\sigma_2}{\sigma_1} \quad \lambda_2 = \frac{\sigma_6}{\sigma_1} \quad \lambda_{12} = \frac{\sigma_6}{\sigma_2} \tag{22}$$

Figure 7 illustrates the biaxiality ratios as a function of off-axis angle θ in the laminate computed in Figure 6. From these data, the angle θ of the off-axis coupon plies can be correlated with a specific stress state in the tubes, allowing for the calculation of applied axial loads to the coupons that will accurately simulate the axial and torsional loading conditions of the tubes.

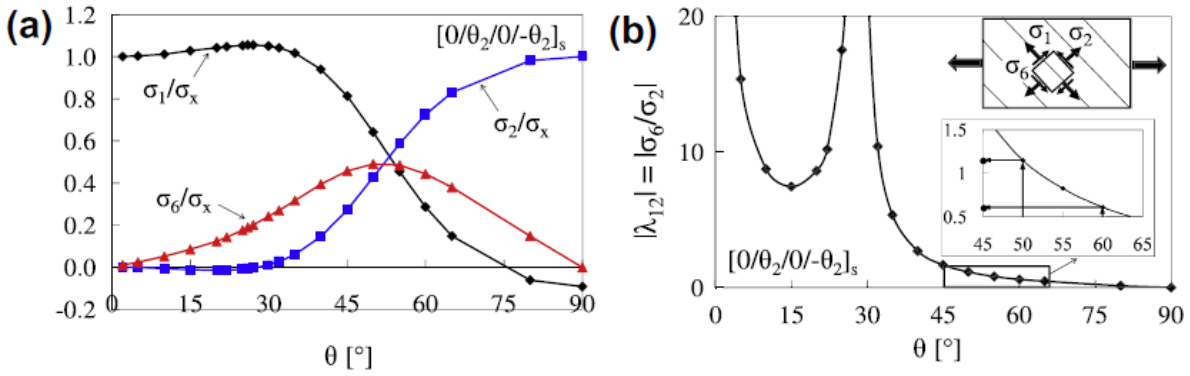

Figure 6. (a) Normalized stresses in an arbitrary off-axis ply in a $[0/\theta_2/0/-\theta_2]_S$ laminate, and (b) values of λ_{12} as a function of off-axis ply angle. Elastic constants given in Ref. [16].

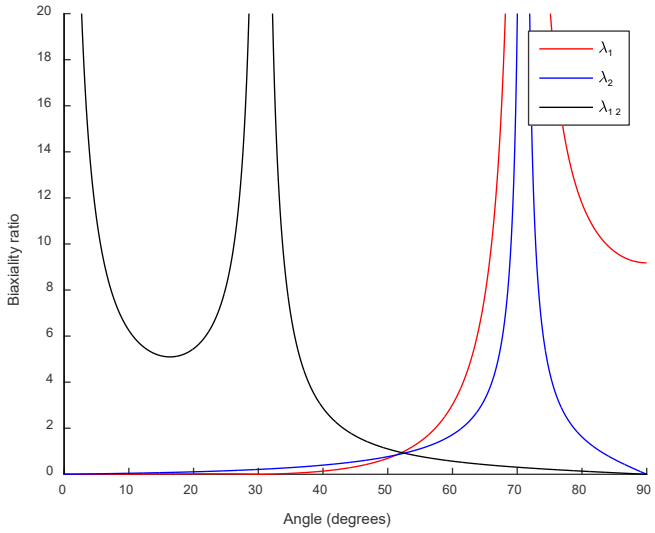

Figure 7. Biaxiality ratios in an arbitrary off-axis ply in a $[0/\theta_2/0/-\theta_2]_S$ laminate subject to compressive loading. Elastic constants given in Ref. [16].

As demonstrated in Refs. [16–18], transverse and shear stresses dominate the fatigue behaviour of unidirectional fibre-reinforced composites. Additionally, while longitudinal stress σ_1 will occur internally due to shear extension coupling, it does not play a significant part in the sub-critical damage mechanisms of the off-axis plies due to the extremely high longitudinal strengths of the plies. For these reasons, further use of the term *biaxiality ratio* in this document will refer specifically to the value λ_{12} unless specified otherwise. It is worth noting, however, that the value of σ_1 in the 0° plies is much larger and could introduce sub-critical damage in the 0° plies, which can diminish their constraining effects on the off-axis plies.

2.2 Overview of the Fatigue Response of Composite Laminates

2.2.1 Cyclic Loading

When designing structures, it is not only critical to evaluate the ultimate strength of the material used, but its ability to endure stresses over a working lifetime. To evaluate the endurance of a component or the materials within it, representative specimens are loaded or strained multiple times until the specimen meets a predetermined failure criterion.

Figure 7 shows the plot of an arbitrary applied cyclic stress over time. The most basic types of cyclic loading have static upper and lower limits σ_{max} and σ_{min} on the applied stresses, though variable amplitude loading is also studied.

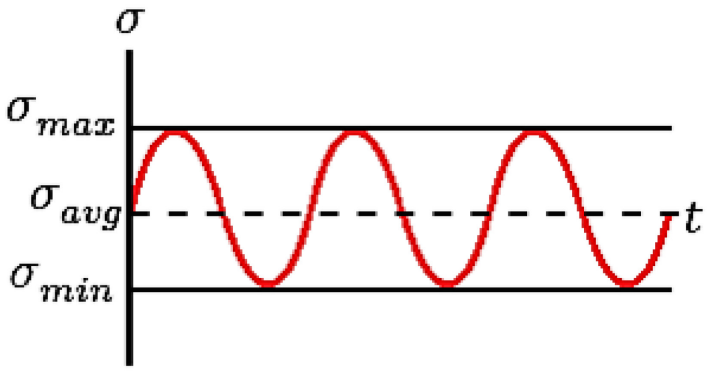

Figure 8. General diagram of cyclic loading.

Depending on the nature of the test, cyclic loading can be purely tensile (T-T), purely compressive (C-C), or oscillate between the two (T-C). The stress ratio, or *R ratio*, of a constant-amplitude fatigue test is defined as:

$$R = \frac{\sigma_{min}}{\sigma_{max}} \quad , \qquad where \begin{Bmatrix} 0 < R < 1 & (T-T) \\ R < 0 & (T-C) \\ R > 1 & (C-C) \end{Bmatrix} \tag{23}$$

With each successive instance of applied stress (each *cycle*), the material undergoes microscope damage which diminishes its elastic properties. Depending on the magnitude of the stress and how that stress compares to the ultimate strength of the material, damage progresses at different rates. This continues until the final cycle, at which point the cumulative damage within a specimen causes catastrophic failure.

The fatigue behaviour of materials or structures is most generally conveyed in a Wöhler curve or *stress-life curve* (S-N curve) relating a material's lifetime to the normalized applied stress (relative the material's strength). Fatigue data exhibits substantial scatter due to numerous sources of variation such as material microstructure, material processing parameters, microscopic defects and specimen misalignment. As a result, fatigue testing requires a very large sample size, with lifetimes being related to normalized stresses using a logarithmic model.

If the cyclic load applied is sufficiently small to not induce internal damage even at material defects and in zones with stress concentrations, the material is said to have an infinite lifetime at that stress, marking that stress as at or below the *endurance limit*.

The degradation of material properties typifies the behaviour of damage, which ultimately leads to catastrophic failure. In metals, damage initiation typically occurs at a defect or a region within a stress concentration zone (internal due to microscale properties like grain boundaries, or externally applied due to the shape of the specimen or external pressure).

2.2.2 Damage Mechanics

A critical element to the understanding of material degradation are the processes by which it experiences *damage*, wherein minute cracks diminish the properties of a material from those of its initial undamaged state. In metals, damage initiates at a single point, generally a defect or a region within a stress concentration zone. As the local stress in that area exceeds the strength of the material (or the reduced strength of the defective zone), a crack appears. In quasistatic loading, this crack would propagate extremely quickly throughout the entire specimen, as the stresses at the crack tip continue to increase drastically. In cyclic loading however, the crack opens only slightly, closes, and reopens again, lengthening it by a minute distance each cycle until it reaches its critical length, where it propagates unstably causing specimen failure.

In FRP composites, the manner in which damage occurs is markedly different, varying with the local state of stress relative to the orientations of each of a laminate's plies. In FRP laminates, damage initiates at multiple locations throughout the specimen, either within the matrix itself, or at the fibre-matrix interface. With each passing cycle, these microscale damage sites expand, and eventually coalesce into intra-ply cracks, which exclusively propagate along the direction of the fibres. As depicted in Figure 9, ply cracks typically traverse the entire width of the specimen (especially in brittle thermoset matrices), and the cracks encompass the entire thickness of the ply, as their out-of-plane growth is arrested by the orientation of the fibres in adjacent plies.

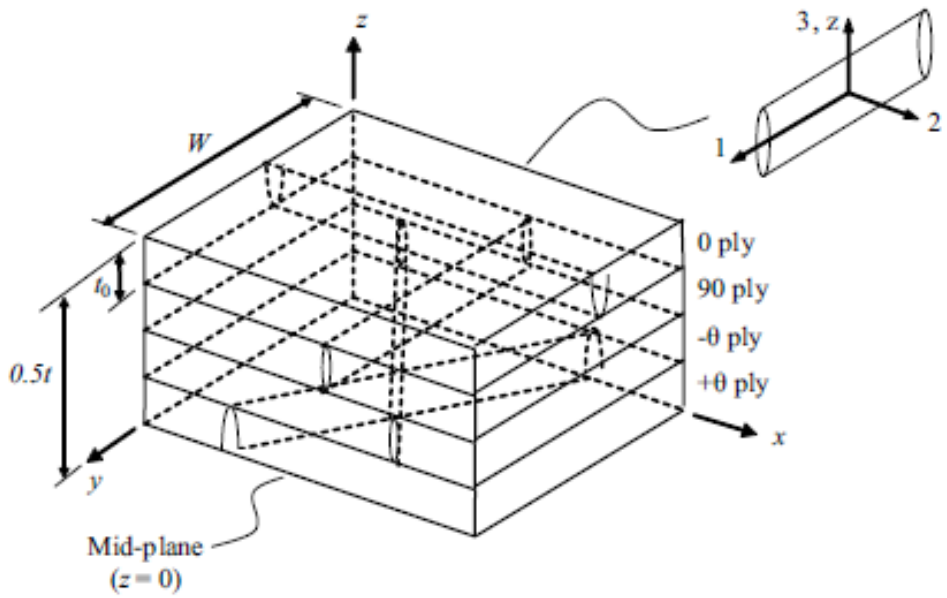

Figure 9. Schematic of cracking in multiple plies within a laminate [19].

Depending on the state of stress in each ply, the number of cracks in the laminate can differ. As the number of cracks increase, this affects the properties of the laminate, especially its stiffness, prior to ultimate failure. Damage can manifest as a single dominant crack in one ply, multiple cracks within one ply, or multiple ply cracks in multiple plies. When cracks end at the edge of a ply, further loading can cause the crack to initiate delamination, a larger-scale critical damage mechanism which involves the separation of adjacent plies.

When a ply experiences cracking, local stresses in the area around the crack are reduced, with the loads being transferred to the adjacent plies. As plies experience crack multiplication, the cracks begin to interact, creating regions which can sustain only the most minimal loads.

2.3 Literature Review

This section provides a brief overview of the state of the art of research in the field of composite laminates.

2.3.1 Studies in Multiaxial Fatigue in Unidirectional Laminates

The study of composite materials and their applications as high-performance materials has been underway for decades at institutions all over the world. Within the specific realm of glass fibre-reinforced polymers (GFRPs), publications have focused on areas including, but not limited to:

- Mechanical loading relative to fibre direction (static, fatigue, normal, shear, bending, internal tube pressure, etc.) [16–18,20–54]
- Failure criteria [52,55]
- Temperature effects [56–59]
- Constraining effects of damaged and undamaged adjacent plies [18,24,26,38,48]
- Fibre-matrix interactions [58,60,61]
- Notches and defects [33,44–46,49,54]

With each additional publication, more insight into the behaviour of laminates is gained, facilitating the development of more accurate predictive models. This section briefly presents the work of several groups which contributed to the fields above. Section 2.3.2 then provides a more thorough review of works in the field of damage mechanics specifically.

The Owen group at the University of Nottingham investigated the fatigue properties of thin-walled tubes under combinations of axial loading and internal pressure (applied by means of oil injection within the tube) [1,2,6]. The tubes comprised glass fabric-reinforced epoxy, with the fabric being either woven or a randomly-oriented non-woven mat, and were prepared by mandrel wrapping and compression against a roller. Flat specimens of similar layup were tested as well under axial and shear loading (static and cyclic). Fatigue properties were quantified primarily using S-N curves and constant-life curves, which compared the lifetimes of composites with different fibre orientation. Multiaxial load states were characterized by counter plots defining ratios between σ_1, σ_2, and σ_6. Overall, robust empirical conclusions were difficult to draw despite extensive experimentation.

Krishnan *et al.* studied the effects of fibre winding angle on the first-ply failure modes of laminate tubes subject to varying combinations of cyclic axial and hoop stress. Different failure modes were observed under different stress ratios and failure envelopes for the different winding angles were constructed. [52]

Dong *et al.* at Peking University used a modification of Puck's criterion to predict failure of an FRP laminate with an arbitrary stacking sequence using iterative residual strength and stiffness predictions and non-linear damage accumulation models [45].

2.3.2 Studies in Damage Mechanics

Damage is any phenomenon which weakens a material over the course of its lifetime. However, damage can take several forms. In composite laminates, the most basic form of damage is ply cracking, which can reduce the stiffness of a material over time, though it does not specifically cause ultimate failure. Consequently, ply cracking is generally

referred to as *sub-critical damage*, in contrast to damage modes such as delamination and fibre failure which rapidly lead to catastrophic failure.

Publications in the field of damage mechanics generally fall into three different categories:

- Investigation of loading and other factors which contribute to the initiation, multiplication, and propagation of intralaminar cracks [62]
- Investigation of how sub-critical damage diminishes the behaviour of composite laminates [19,55,63–67]
- Investigation of how sub-critical damage progresses towards larger-scale damage mechanisms and ultimate laminate failure (i.e. damage tolerance) [68]

Within these subdivisions, investigations can be computational (i.e. analytical vs. numerical methods), experimental, or a mixture of the two, which generally take the form of the developing semi-empirical models of damage behaviour.

2.3.2.1 Computational Micromechanics

A wide variety of publications in the literature have focused on the development of models to predict the behaviour of damaged composite structures. The field of computational micromechanics is a comparatively recent field of study, made possible by advanced computational methods, specifically finite element analysis. This typically involves the application of specific stress states to *representative volume elements* (RVEs) which, when combined with periodic boundary conditions, represent an arbitrary volume with a laminate.

Publications by Montesano and Singh focus on the development of multi-scale models to predict the detrimental effects of sub-critical damage on laminate stiffness. RVEs representing symmetric laminates containing ply cracks in all on-axis and off-axis plies were simulated under a range of multiaxial stress states. The results accurately represented damage observed in experimental and other computational works. Further improvements considered statistical variations in the crack density-dependant critical strain energy release rate, a parameter previously obtained empirically [19,67].

Publications from the LLorca group at the IMDEA-Materiales institute have delved into the microstructural failure surfaces of glass-epoxy and carbon-epoxy laminates under transverse compression, tension, and out-of-plane shear. Specifically, the works focused on the effects of fibre-matrix interface strength on damage mechanisms in the RVE. In compression, the dominating damage mechanisms were interfacial debonding and shear band formation, which occurred in laminates with strong and weak interfaces respectively. Laminates with weak interfaces fractured due to the initiation and propagation of interfacial cracks in transverse tension, and matrix cracks in transverse shear, while laminates with strong interfaces in transverse tension and transverse shear failed due to the plastic deformation inherent to the matrix. Comparison of these findings to existing failure criteria suggests that matrix and interface strength play a more prevalent role under transverse loading than previously considered [69,70].

2.3.2.2 Experimental and Semi-Empirical Studies

In the early 1990s, the Tamuzs group at the Institute of Polymer Mechanics in Riga produced a series of publications regarding the effects of a variety of biaxial fatigue load states on glass fibre and fabric-reinforced epoxy tubes [8,9,11,13,47]. These publications studied combinations of torsional and axial fatigue (compression and tension) on a variety of multi-directional laminates, which were prepared via mandrel wrapping with a binding agent impregnated within the matrix to prevent interlaminar void formation. Normal loads were applied cyclically, while shear stresses appeared as either static or cyclic loads. S-N curves were used to quantify fatigue properties. Crack angles and surface profiles for the different loading conditions were documented post mortem by eye. It was demonstrated that in-plane shear stresses, applied statically or cyclically greatly reduced the fatigue properties of all composites tested, particularly in the case of combined compression-torsion loading.

Studies on microscale and macroscale damage evolution were performed by the Fujii group at Doshisha University [14–16]. Tubular specimens comprised a plain-woven glass-reinforcement in epoxy (with an equivalent weft and warp), prepared via wet-winding. In several publications, specimens were notched using a drill or diamond blade to induce regions of crack initiation for study. Tubes were subjected to combinations of tension and torsion fatigue loading. Fatigue behaviour was characterized using S-N curves and stiffness degradation plots. A CCD camera and a microscope were used to perform *in situ* and *ex situ* crack profiling. It was observed that the notch caused failure much earlier in specimens with high shear stress, and that fracture surfaces run perpendicular and parallel to the tube axis in cases of fatigue and static loading respectively.

The Quaresimin group at the University of Padova has produced a series of publications focusing on the characterization of sub-critical damage mechanisms in laminate tubes under multiaxial fatigue loading [17,18,51]. Tubular specimens comprising transverse plies sandwiched by crack-stabilizing woven plies were subjected to tension/torsion loading (without glass fabric, crack initiation immediately led to specimen failure due to unstable propagation). S-N curves, stiffness reduction measurements, and Paris-like curves were made to quantify general fatigue properties, which verified the dominating effects of shear loading on fatigue life. Crack profiling was performed *in situ* by lock-in analysis and visually (taking advantage of the glass/epoxy transparency), as well as *ex situ* via SEM, which suggested that matrix-fibre debonding may be a significant damage mechanism, and that shear stress is the dominating contributor to failure.

2.3.3 Sparse Fields of Study of in the Literature

The breadth of areas studied is far-reaching, though there are many areas in which the number of publications is limited. Of particular relevance to this investigation is the lack of experimental works on transverse compressive damage mechanisms. This is likely due to the inherent challenges associated with compression testing (e.g. buckling and the design of compressive fixtures), non-linear elastic behaviour often observed in compression, and the increased sensitivity of compressive behavior to factors such as fibre misalignment and defects.

Beyond transverse compressive loading, the existing literature has several knowledge gaps that must be addressed with further study. First, and most fundamentally, there is a distinct lack of comprehension of ply-level properties and their influence on sub-critical damage mechanisms, and the influence of these mechanisms on material properties and lifetime. This knowledge is crucial for developing accurate damage-based models, which

are required to predict the complex deformational response of laminates under multiaxial loads. Consequently, a bottom-up approach to their characterization is necessary for accurate description. Despite their prevalence in the literature, S-N curves alone are not sufficient to provide insight into the complexities of micro-mechanical composite behaviour.

Using both experimental techniques and computational simulations, research must be performed to develop constitutive relationships that can predict the degradation of bulk composite properties caused by sub-critical damage mechanisms, and simulation models that can predict the evolution of these damage mechanisms under multiaxial cyclic loads.

The first major building block of these models is the understanding of sub-critical damage mechanisms, which are typically intralaminar ply cracks, which are known to cause notable degradation of the laminate properties. Fibre fracture and inter-ply delamination cracks typically constitute catastrophic failure of a composite, and therefore constitute critical rather than sub-critical damage mechanisms.

Using a variety of crack characterization methods, it is necessary to correlate sub-critical damage mechanisms and their effects on laminate properties with different applied loads. From a numerical perspective, the degree of cracking must be correlated to the different applied stress states. Depending on the specimen geometry, cracking can be quantified in numerous different ways, including crack opening displacement (COD) and crack sliding displacement (CSD), crack growth rate (CGR), and strain energy release rate (SERR). Plots characterizing volumetric crack growth or crack density as a function of lifetime can also be presented in addition to plots of effective modulus as a function of lifetime. From these data, equations for crack growth rate (volumetric or temporal) as a function of existing crack size could be obtained. If such relationships can be determined,

simulation data can be used to incorporate material properties such as constraining effects of other plies. In addition to damage mechanisms, relationships between damage and mechanical behaviour must be established. Reduced stiffness and wear life should be correlated against load iterations to produce data on how sub-critical damage affects the material. S-N curves are the most commonly used methods for this, though stiffness vs. load iterations are also used.

3 Experimental Design

The primary body of experimentation in this work was the loading of laminates under combined compression-shear cyclic loading, and the characterization of crack initiation which occurred within specific plies during this loading. The effects of cyclic multiaxial stress on ply failure was investigated in two different specimen types: tubular and rectangular laminates. The study of two specimen types was performed to determine the effects of geometric factors such as material curvature, ply thickness, and neighbouring ply orientation on crack behaviour.

The layup of the tubular laminates comprised two hoop-wound unidirectional plies supported internally and externally by thin plies containing a woven glass fabric (herein referred to by laminate layup shorthand as $[0_F/90/90/0_F]$ or $[0_F/90]_S$). Transverse compressive stress was applied to the hoop-wound (90°) plies by compressing the tube along its length, while shear stress was applied via torsion to the tube. The presence of the internal and external fabric plies was required to constrain cracking during cycling loading such that the *propagation* of cracks could be investigated. The thinness of the plies and their small fibre diameters was reported not to substantially influence the *initiation* of cracks within the hoop-wound plies [18]. The layup of the multidirectional coupons comprised layers of unidirectional plies in the fibre direction (°0), each sandwiching plies at an angle θ or $-\theta$ relative to the loading direction (herein referred to by $[0_2/\theta_2/0_2/-\theta_4/0_2/\theta_2/0_2]$ or $[0_2/\theta_2/0_2/-\theta_2]_S$). The angle of the $\pm\theta$ plies affects the magnitude of shear extension coupling.

The effects of cyclic stress on cracking behaviour were examined within specific plies of interest within laminate specimens, specifically the transverse plies of $[0_F/90]_S$ tubes, and off-axis $\pm\theta$ plies in the multidirectional $[0_2/\theta_2/0_2/-\theta_2]_S$ coupons. However, before these experiments could begin, an initial computational study of the materials was required to design the test specimens. This study comprised several parts:

- Determination of the desired multidirectional laminate layups using experimentally-determined properties
- Determination of desired stress states and corresponding loads for cyclic loading of tubular and rectangular specimens
- Verification of classical laminate behaviour in tubular laminates using finite element analysis
- Determination of critical buckling loads

MATLAB 2015a was used to create a modular toolkit for automating the classical laminate analysis of a variety of laminates under a wide range of loads and torques, described in this section. In this section, *literature values* refers to elastic constants presented in Table 1, while *experimental values* refers to elastic constants obtained by quasistatic characterization of unidirectional panels, provided in Chapter 5.

An literature survey [13,16,71–81] was performed to determine the approximate compressive strengths F_{1C} and F_{2C} for E-glass/epoxy laminates with similar volume fractions, elastic constants and strengths to those provided in Ref. [16]. The results of the survey yielded approximate F_{1C} and F_{2C} values of 600 MPa and 85 MPa, which would be used as baseline values for evaluating laminate behavior.

Table 1. Elastic constants and strengths of E-glass/epoxy laminates in Ref. [16].

Elastic Constant	Literature Value ($V_F = 0.45$)
E_1	34.86 GPa
E_2	9.419 GPa
G_{12}	3.193 GPa
ν_{12}	0.326
Strength	
F_{1T}	973 MPa
F_{2T}	50 MPa
F_{1C}	Not provided
F_{2C}	Not provided
F_6	98 MPa

3.1 Biaxiality Ratio Calculations

The multidirectional laminates considered in this investigation (general layup $[0_2/\theta_2/0_2/-\theta_2]_S$), were designed to use shear extension coupling to introduce shear stress into a ply loaded at an angle to its fibres. Figure 10 shows a top-down view of such a laminate. Laminates with the layup $[0/\theta_2/0/-\theta_2]_S$ (half the number of 0° plies) were initially considered, though the possibility of buckling warranted the addition of extra supporting layers.

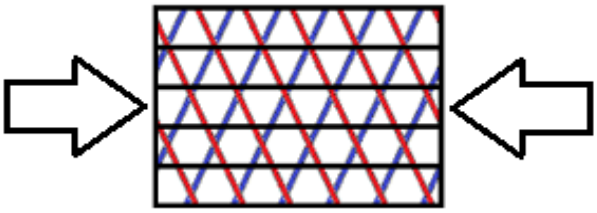

Figure 10. Schematic diagram of a multidirectional laminate containing on-axis plies (0°, black), and off-axis plies ($+\theta$, blue and $-\theta$, red).

3.1.1 Multidirectional Panels Using Literature Values

The behaviour of laminates with literature values for elastic properties were initially simulated to provide a baseline prediction of behavior of the material in this investigation. In a $[0/50_2/0/\text{-}50_2]_S$ laminate with literature value properties and approximate F_{1C} and F_{2C} values of -600 MPa and -85 MPa, the failure of the 50° plies, based on the maximum normal stress criterion (i.e. $|\sigma| = |\sigma_{ult}|$), occurs at a load $P^{50}_{\max}$of -41.07 kN. However, the 0° plies fail earlier, at a load $P^{0}_{\max}$of -35.45 kN. To accurately determine the effects of the multiaxial stress state on crack initiation, the off-axis plies experiencing said stress state must be the first plies to fail. A comparison to Ref. [16] was initially desired, wherein $[0/50_2/0/\text{-}50_2]_S$ and $[0/60_2/0/\text{-}60_2]_S$ experienced biaxiality ratios of $\lambda_{12} = 1.10$ and $\lambda_{12} = 0.57$, respectively. However, the approximate strengths obtained from literature prohibit the use of a $[0/50_2/0/\text{-}50_2]_S$ laminate, though off-axis plies at angles greater than 60° fail before their adjacent 0° plies.

3.1.2 Multidirectional Panels Using Experimental Values

When the true elastic constants and strengths of the unidirectional plies were obtained from quasistatic tests (see Section 5.1.4), constitutive behaviour calculations were performed to confirm if and how the off-axis ply angles must change to produce the desired stress states. Using the reference layup of $[0/\theta_2/0/-\theta_2]_S$, the biaxiality ratios present in a range of off-axis plies were computed, summarized in Table 2.

Table 2. Biaxiality ratios in $[0/\theta_2/0/-\theta_2]_S$ laminates with a variety of off-axis ply angles.

Off-Axis Ply Angle [°]	λ_1	λ_2	λ_{12}
45	0.4201	0.5932	1.4120
48.35	0.6624	0.7329	1.1064
50	0.8253	0.8166	0.9894
55	1.6099	1.1614	0.7214
59.00	2.8334	1.6126	0.5691
60	3.2955	1.7695	0.5369
65	7.9871	3.2041	0.4012
70	44.1754	13.0448	0.2953
75	27.1467	5.6548	0.2083
80	14.1740	1.8873	0.1332

The maximum allowable load for a given coupon layup P_{max}^{coupon} is defined as the applied axial load that will cause catastrophic failure in the off-axis plies. The failure criterion for this analysis was the maximum stress criterion. Laminate coupons were assumed to have a nominal width and ply thickness of 15 mm and 0.27 mm respectively. Classical Laminate Theory treats laminates as perfectly-bonded linear-elastic materials experiencing plane states of stress, and the assumptions outlined in Section 2.1.1.1 allow the representation of the laminate as a system of linear equations. Consequently, changes to the width or ply thickness linearly adjust the stresses based on a given applied load (i.e. halving the laminate width halves the failure load).

From the highlighted angles and biaxiality ratios in Table 2, calculations for ply loads and stresses were performed. However, these calculations revealed two significant hurdles which undermined efforts to perform tests at the same biaxiality ratios as Ref. [16] (λ_{12} = 1.10, 0.57). The first issue was the notable difference between literature values and those obtained by experiment. The comparatively poor shear strength in this material, as well as the much higher transverse strength in compression than tension, meant that at both desired λ_{12} values (1.10 and 0.57), it would be impossible to achieve more than 30% of the F_{2C} value without causing the off-axis plies to fail statically by shear stress. The second issue was the combination of higher transverse strength (compressive vs. reference tension), the lower longitudinal strength, and the high longitudinal modulus. Based on these values, impractically high loads would be required to induce sufficient transverse stresses in the off-axis plies; the high loads would be primarily supported by the longitudinal plies due to their high stiffness, resulting in them being loaded to approximately 95% of their F_{1C} values. This was not a concern in tension, since transverse tension and longitudinal tension are the weakest and strongest directions of the material, so low loads – which do not threaten the integrity of the 0° plies – could be used.

Figure 11 and Figure 12 illustrate the states of stress in a $[0/48_2/0/\text{-}48_2]_S$ (λ_{12} = 1.10) laminate under a range of axial loads. Dashed lines indicate stress values which meet the corresponding strength of the plies. Table 3 and Table 4 show the ply stresses in laminates with 48° and 59° angled plies. Red cells indicate stresses which exceed the corresponding strength of the ply. The tables indicate that to prevent static failure, multidirectional specimens with λ_{12} = 1.10 would need to be loaded to a maximum of 20% of their ultimate transverse compressive stress. Due to fatigue limit of materials at such a low stress level, this would not be practical. Consequently, a lower biaxiality ratio

would be required to compensate for the low shear strength. Based on Table 2, off-axis ply angles of 65° and 75° were chosen, corresponding to biaxiality ratios of 0.40 and 0.21.

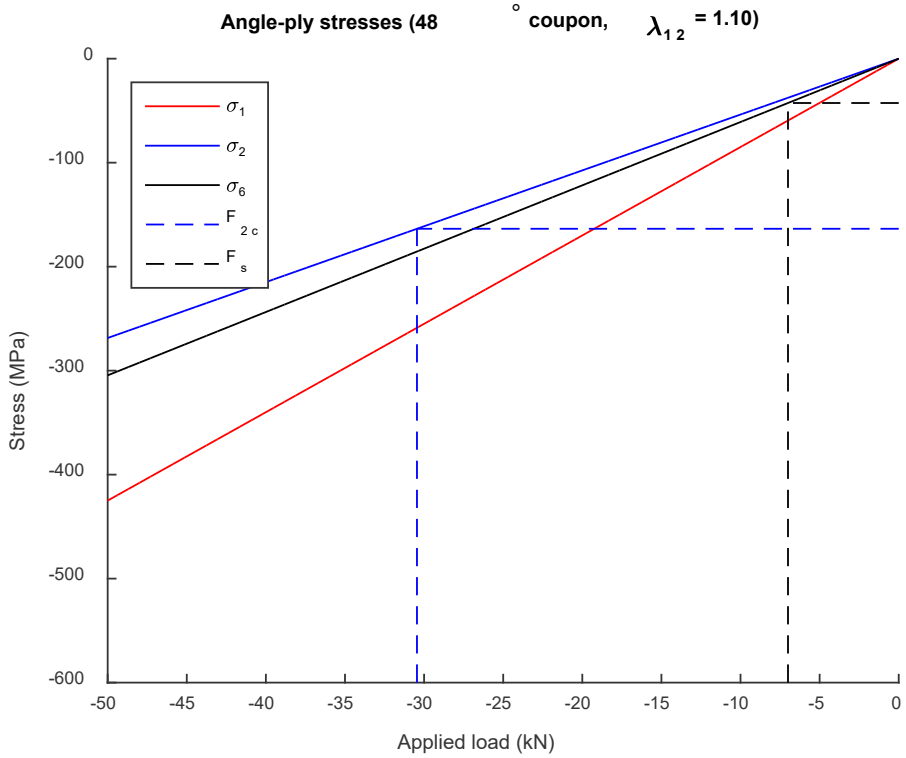

Figure 11. Ply stresses in off-axis plies in a $[0/48_2/0/-48_2]_S$ laminate.

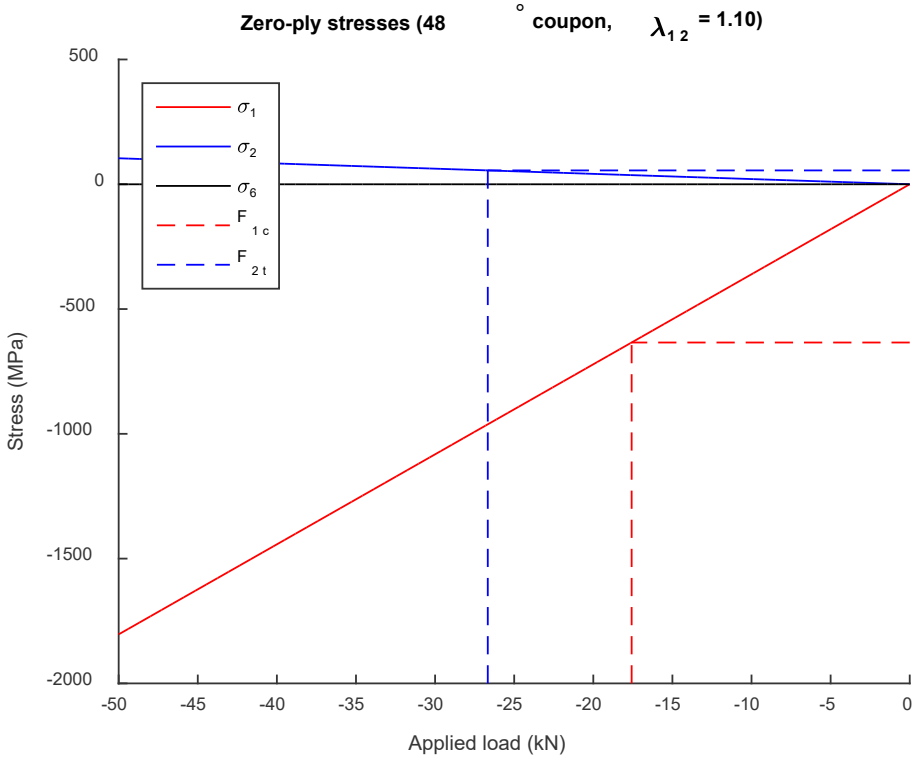

Figure 12. Ply stresses in 0° plies in a $[0/48_2/0/-48_2]_S$ laminate.

Table 3. Ply stresses in 0° (0) plies and angled plies (A) based on transverse compressive load in the angled plies (48°, $\lambda_{12} = 1.10$)

σ_2^A/F_{2c}^A	P_{min} [N]	σ_1^0 [MPa]	σ_2^0 [MPa]	σ_6^0 [MPa]	σ_1^A [MPa]	σ_2^A [MPa]	σ_6^A [MPa]
1.00	-30450	-1098.3	63.5	0	-258.8	-163.6	-185.5
0.90	-27405	-988.5	57.1	0	-232.9	-147.2	-166.9
0.80	-24360	-878.7	50.8	0	-207.0	-130.9	-148.4
0.70	-21315	-768.8	44.4	0	-181.2	-114.5	-129.8
0.60	-18270	-659.0	38.1	0	-155.3	-98.2	-111.3
0.50	-15225	-549.2	31.7	0	-129.4	-81.8	-92.7
0.40	-12180	-439.3	25.4	0	-103.5	-65.4	-74.2
0.30	-9135	-329.5	19.0	0	-77.6	-49.1	-55.6
0.20	-6090	-219.7	12.7	0	-51.8	-32.7	-37.1
0.10	-3045	-109.8	6.3	0	-25.9	-16.4	-18.6

Table 4. Ply stresses in zero-degree (0) plies and angled plies (A) based on transverse compressive load in the angled plies (59°, $\lambda_{12} = 0.57$)

σ_2^A / F_{2c}^A	P_{min} [N]	σ_1^0 [MPa]	σ_2^0 [MPa]	σ_6^0 [MPa]	σ_1^A [MPa]	σ_2^A [MPa]	σ_6^A [MPa]
1.00	-18220	-689.3	7.2	0	-57.7	-163.6	-93.1
0.90	-16398	-620.4	6.5	0	-52.0	-147.2	-83.8
0.80	-14576	-551.4	5.8	0	-46.2	-130.9	-74.5
0.70	-12754	-482.5	5.1	0	-40.4	-114.5	-65.2
0.60	-10932	-413.6	4.3	0	-34.6	-98.2	-55.9
0.50	-9110	-344.6	3.6	0	-28.9	-81.8	-46.6
0.40	-7288	-275.7	2.9	0	-23.1	-65.4	-37.2
0.30	-5466	-206.8	2.2	0	-17.3	-49.1	-27.9
0.20	-3644	-137.9	1.4	0	-11.6	-32.7	-18.6
0.10	-1822	-68.9	0.7	0	-5.8	-16.4	-9.3

Stress vs. load calculations for the newly selected biaxiality ratios (0.40 and 0.21) were performed, tabulated in Table 5 and Table 6. With an off-axis angle of 65°, the laminate could be loaded to approximately 70% of the F_{2C} without causing static shear failure of the plies. At 75°, the laminates could be loaded to 100% of the F_{2C} without causing static shear failure. Additionally, neither laminate would experience static failure of the 0° plies.

Table 5. Ply stresses in zero-degree (0) plies and angled plies (A) based on transverse compressive load in the angled plies (65°, $\lambda_{12} = 0.40$)

σ_2^A / F_{2c}^A	P_{min} [N]	σ_1^0 [MPa]	σ_2^0 [MPa]	σ_6^0 [MPa]	σ_1^A [MPa]	σ_2^A [MPa]	σ_6^A [MPa]
1.00	-15724	-594.05	-8.46	0	-20.48	-163.58	-65.62
0.90	-14152	-534.66	-7.61	0	-18.43	-147.22	-59.06
0.80	-12580	-475.27	-6.77	0	-16.39	-130.87	-52.50
0.70	-11007	-415.84	-5.92	0	-14.34	-114.51	-45.93
0.60	-9435	-356.45	-5.08	0	-12.29	-98.15	-39.37
0.50	-7862	-297.02	-4.23	0	-10.24	-81.79	-32.81
0.40	-6290	-237.63	-3.38	0	-8.19	-65.43	-26.25
0.30	-4717	-178.21	-2.54	0	-6.14	-49.07	-19.69
0.20	-3145	-118.82	-1.69	0	-4.1	-32.72	-13.12
0.10	-1572	-59.39	-0.85	0	-2.05	-16.35	-6.56

Table 6. Ply stresses in zero-degree (0) plies and angled plies (A) based on transverse compressive load in the angled plies (75°, $\lambda_{12} = 0.21$)

σ_2^A / F_{2c}^A	P_{min} [N]	σ_1^0 [MPa]	σ_2^0 [MPa]	σ_6^0 [MPa]	σ_1^A [MPa]	σ_2^A [MPa]	σ_6^A [MPa]
1.00	-13783	-512.29	-23.40	0	6.03	-163.58	-34.07
0.90	-12405	-461.08	-21.06	0	5.42	-147.22	-30.67
0.80	-11027	-409.86	-18.72	0	4.82	-130.87	-27.26
0.70	-9648	-358.60	-16.38	0	4.22	-114.50	-23.85
0.60	-8270	-307.38	-14.04	0	3.62	-98.15	-20.45
0.50	-6892	-256.17	-11.70	0	3.01	-81.80	-17.04
0.40	-5513	-204.91	-9.36	0	2.41	-65.43	-13.63
0.30	-4135	-153.69	-7.02	0	1.81	-49.07	-10.22
0.20	-2757	-102.47	-4.68	0	1.21	-32.72	-6.82
0.10	-1378	-51.22	-2.34	0	0.60	-16.35	-3.41

An additional set of calculations was performed to determine the effects of changing the laminate layup. As shown in Table 7, the biaxiality ratios do not change if the proportion of 0° plies to angled plies remains the same. Additionally, any changes which occur from altering the ply ratios do not significantly change the biaxiality ratios λ_{12}. While the ratios λ_1 and λ_2 exhibit more drastic changes with the change in off-axis ply angle, the relative magnitude of σ_1 (order of 10 MPa) makes these changes have little effect on the state of stress in the plies. While off-axis plies do have a non-zero σ_1, its small magnitude mitigates its contribution to ply failure, and the plies can be reasonably considered to have a biaxial stress state comparable to that of the tubes (which also have a minimal, non-zero σ_1 shown in Figure 22 in Section 3.2).

Table 7. Effects of layup change on stress state of off-axis plies in a laminate.

Layup	n_0/n_A	λ_1	λ_2	λ_{12}
$[0/65_2/0/\text{-}65_2]_S$	0.5	7.9871	3.2041	0.4012
$[65/0/\text{-}65]_S$	0.5	7.9871	3.2041	0.4012
$[0/65/0/\text{-}65]_S$	1.0	9.3950	3.8003	0.4045
$[0_2/65_2/0_2/\text{-}65_2]_S$	1.0	9.3950	3.8003	0.4045
$[65/0_2/\text{-}65]_S$	1.0	9.3950	3.8003	0.4045

3.1.3 Tubular Specimens Using Experimental Values

With the desired states of stress within the multidirectional laminates determined, calculations were performed to determine the loads and torques required to induce the same desired stress states ($\lambda_{12} = 0.40$ and 0.21) in the transverse plies of the tubes (layup $[0_F/90]_S$). Classical mechanics dictates that within a circular cross-section, the magnitude of the shear stress τ is proportional to the radius ρ of the stress locus from the centre of the cross-section, as shown in the formula below:

$$\tau = \frac{T\rho}{J} \tag{24}$$

where T is the applied torque and J is the polar moment of inertia of the cross-section. A cross-section of the tube specimens is shown in Figure 13. To account for the curvature of the tubes within the Classical Laminate Theory framework, the definition of the applied force per unit width N requires an adjustment to evaluate ply stresses at the outer radius of the 90° plies, R_{90}. Adjustments were not made to the definition of applied moment per unit area M, since the plies do not experience out-of-plane bending.

$$A_{tube} = \pi(R_o^2 - R_i^2) \tag{25}$$

$$J = \frac{\pi(R_o^4 - R_i^4)}{2} \tag{26}$$

For a thin-walled tube, the polar moment of inertia J can be approximated as

$$J = 2\pi t R^3 = tCR^2 \tag{27}$$

where t is the wall thickness of the tube, R is the mean radius of the tube wall, and C is the circumference at the mean radius R. This definition for J allows N_{xy} to be put in terms of R_{90}:

$$N_{xy} = \sigma_{xy} t = \frac{TR_{90}}{J} t = \frac{TR_{90}}{2\pi t \mathrm{R}^3} t = \frac{TR_{90}}{CR^2} \tag{28}$$

$$N_{coupon} = \begin{bmatrix} P/b \\ 0 \\ 0 \end{bmatrix} \quad , \quad N_{tube} = \begin{bmatrix} P/C \\ 0 \\ TR_{90}/(CR^2) \end{bmatrix} \tag{29}$$

With this relationship established, N can now be expressed simply in terms of the applied loads and torques, and the established relationships can be combined to form an explicit constitutive equation relating the stress in an arbitrary ply k to an applied load and torque:

$$\begin{Bmatrix} \sigma_1 \\ \sigma_2 \\ \sigma_6 \end{Bmatrix}_k = [T_1]_k \left[\bar{Q}\right]_k [A]^{-1} \begin{bmatrix} P/C \\ 0 \\ TR_{90}/(CR^2) \end{bmatrix} \tag{30}$$

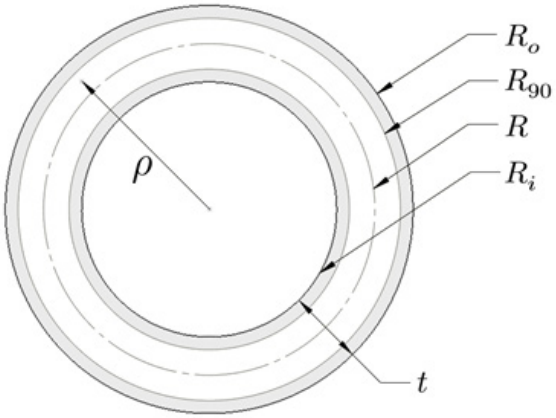

Figure 13. Schematic cross-section of a tube specimen with constants pertaining to the thin woven fabric layers (grey) and the unidirectional transverse layers (white). Shear stress within the cross-section can be evaluated at any arbitrary radius ρ.

To simulate the biaxiality ratios present in the different multidirectional coupons, Figure 14 through Figure 21 show the *load ratios* required to impart the desired stress ratios ($\lambda_{12} = 0.40$ and 0.21) to the tubes. Black markers indicate combinations of torque and load which induce biaxiality ratios within 1% of a desired value. The black markers extend linearly to the origin, though the figures only show load and torque combinations that induce a state of stress within 1% of the F_{2C} or the F_6. Each stress state is computed relative to the F_{2C} and the F_6 values, and the mode of failure is determined by the lowest corresponding load or torques, as shown in Table 8. It was determined that at $\lambda_{12} = 0.40$, the tubes were predicted to fail due to shear, whereas at $\lambda_{12} = 0.21$, the tubes were predicted to fail by transverse compression.

Table 8. Loads and torques applied at points of static ply failure in tubes under prescribed biaxiality ratios. Red cells indicate the mode of failure (transverse compression or shear) which occurs first.

	$\lambda_{12} = 0.40$ Loads	$\lambda_{12} = 0.40$ Stresses	$\lambda_{12} = 0.21$ Loads	$\lambda_{12} = 0.21$ Stresses
Tube P_{2C}	-7609 N	-163.58 MPa	-7609 N	-163.58 MPa
Tube T_{2C}	-26.31 N · m	-66.18 MPa	-14.29 N · m	-34.84 MPa
Tube P_S	-4930 N	-104.07 MPa	-9030 N	-197.78 MPa
Tube T_S	-17.06 N · m	-42.09 MPa	-17.06 N · m	-42.10 MPa

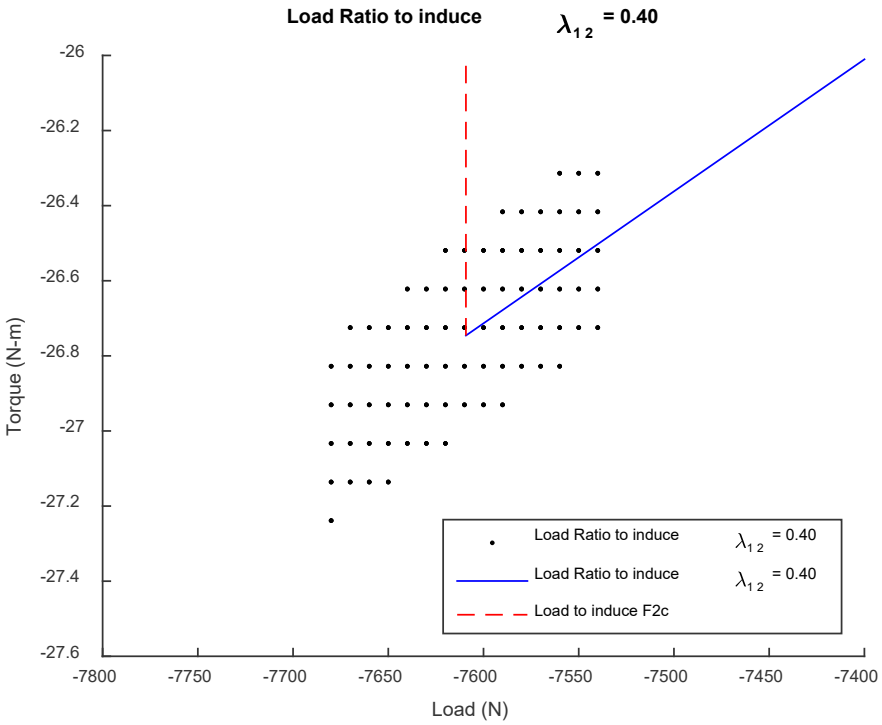

Figure 14. Applied loads and torques within 1% of the failure compressive load in a tube under $\lambda_{12} = 0.40$.

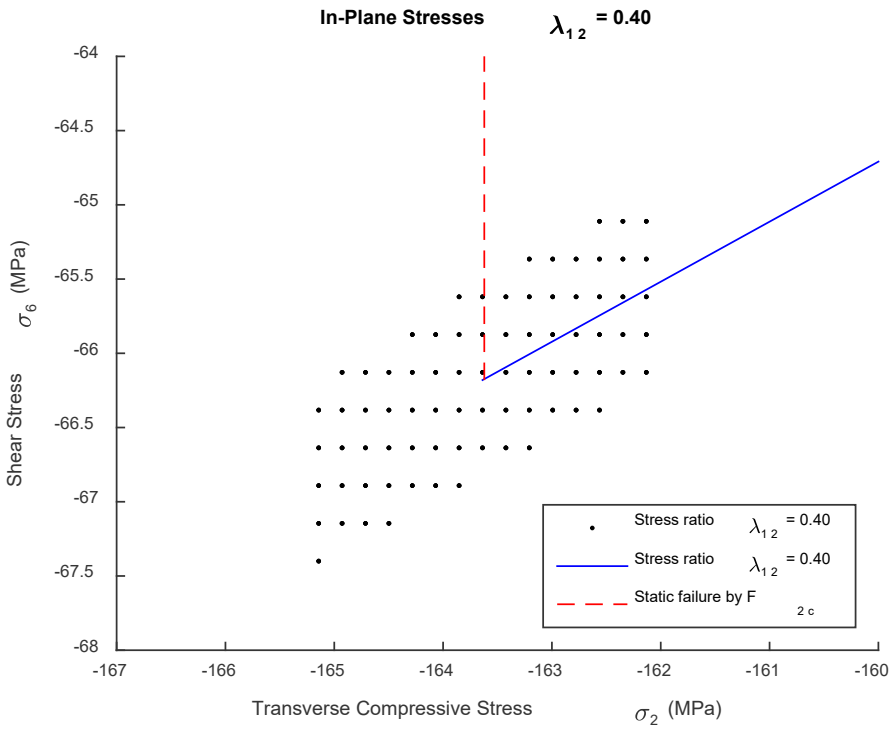

Figure 15. Ply stresses at the ultimate transverse compressive strength within a tube under $\lambda_{12} = 0.40$.

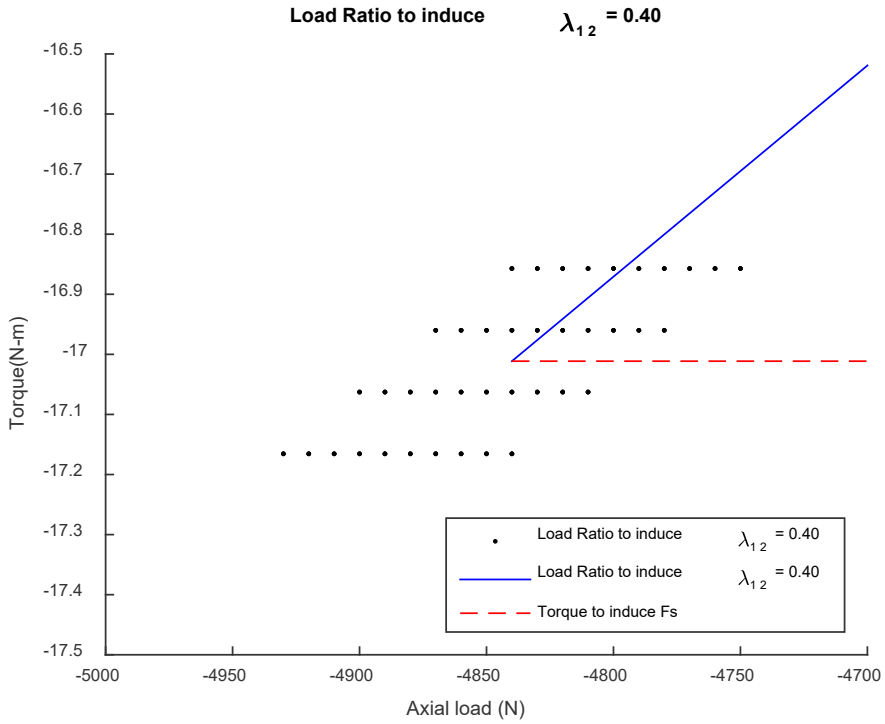

Figure 16. Applied loads and torques within 1% of the failure torque in a tube under $\lambda_{12} = 0.40$.

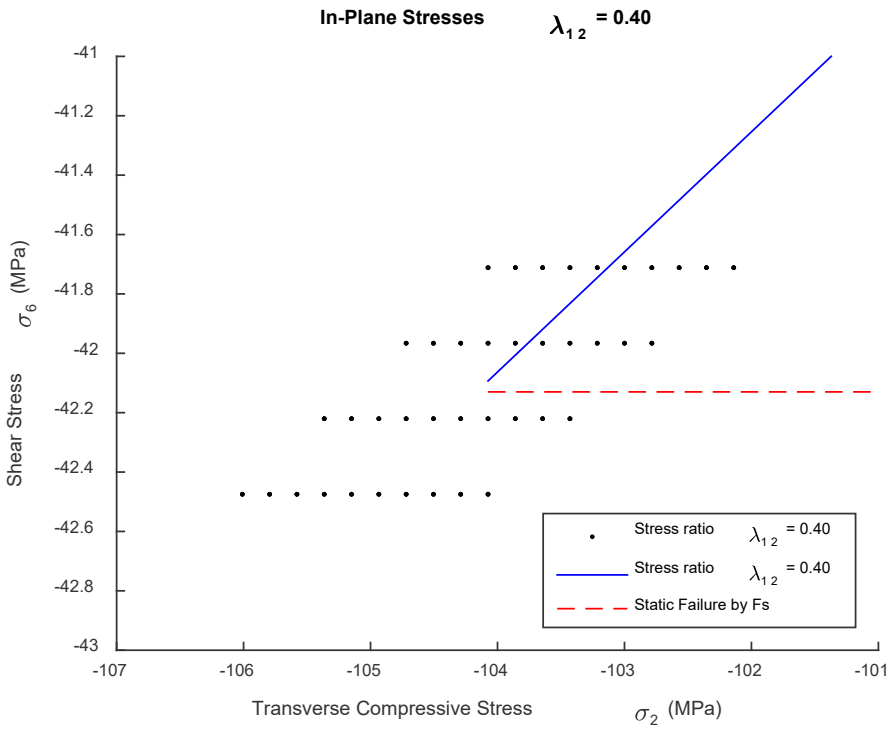

Figure 17. Ply stresses within 1% of the ultimate shear strength in a tube under $\lambda_{12} = 0.40$.

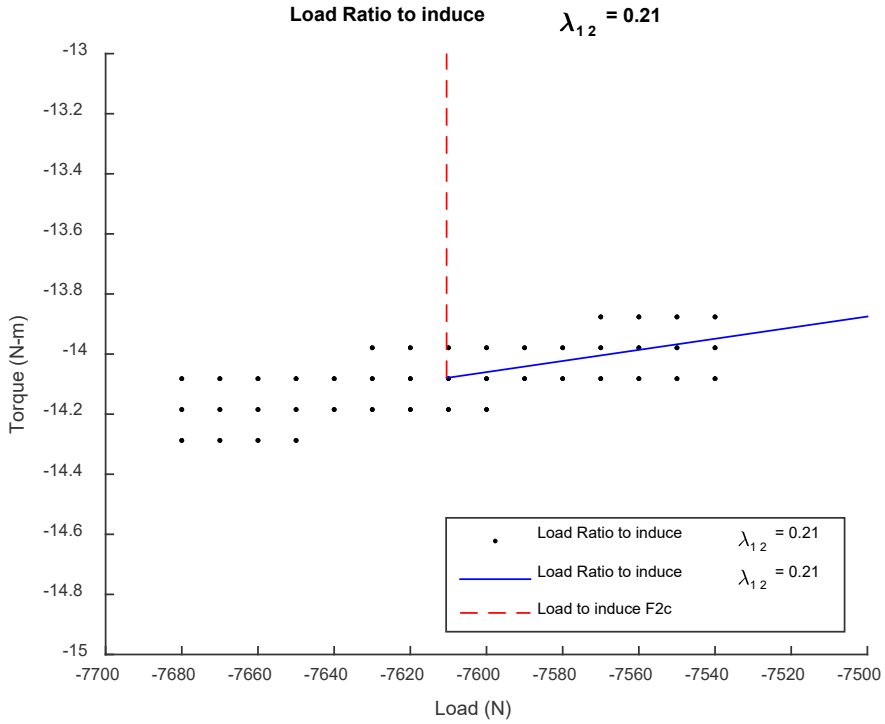

Figure 18. Applied loads and torques within 1% of the failure compressive load in a tube under $\lambda_{12} = 0.21$.

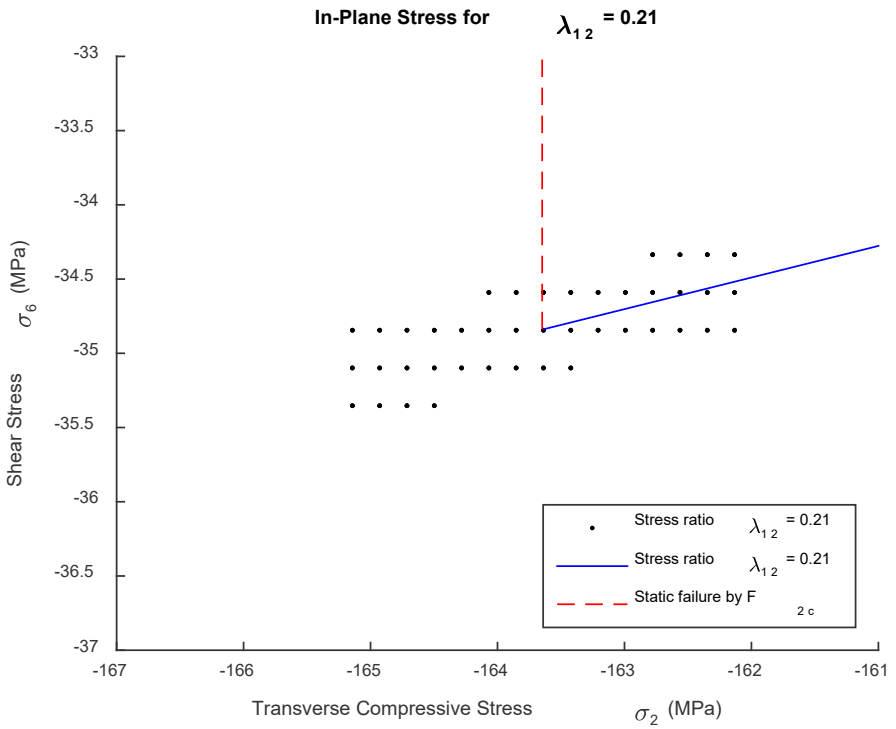

Figure 19. Ply stresses at the ultimate transverse compressive strength within a tube under $\lambda_{12} = 0.21$.

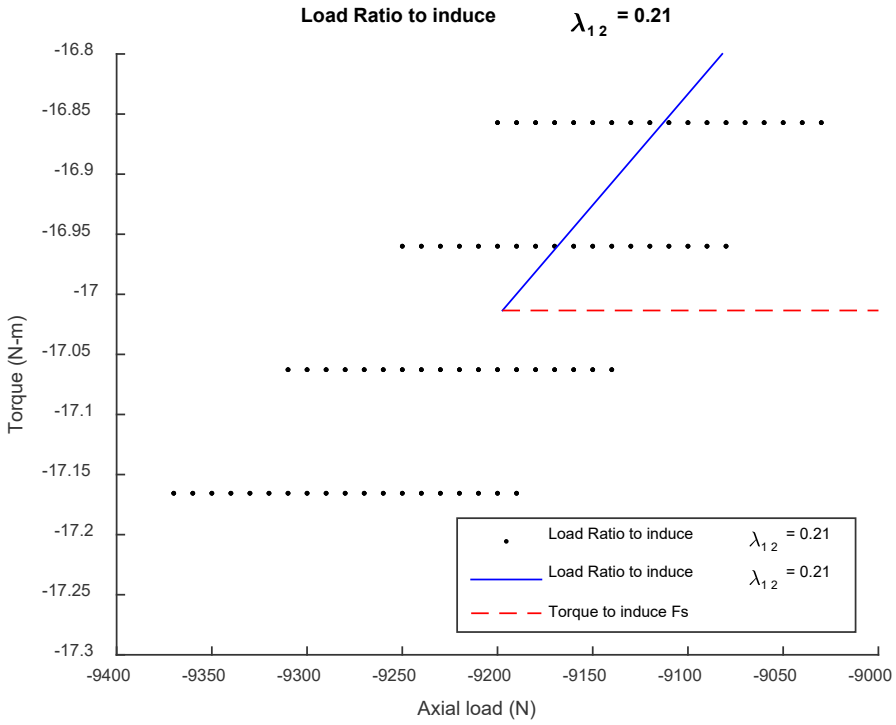

Figure 20. Applied loads and torques within 1% of the failure torque in a tube under $\lambda_{12} = 0.21$.

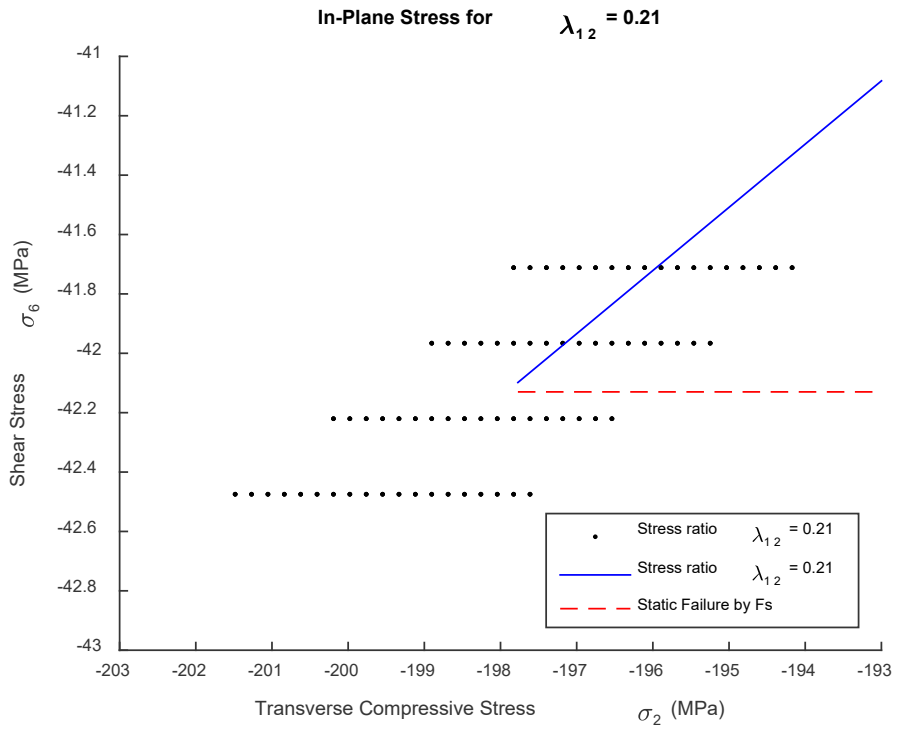

Figure 21. Ply stresses within 1% of the ultimate shear strength in a tube under $\lambda_{12} = 0.21$.

As with the multidirectional coupons, ply stresses are linearly proportional to the applied loads and torques. Consequently, determining the reduced stresses, loads and torques for cyclic loading was done by similarly reducing the magnitude of the applied loads and torques while maintaining the same load ratio.

Table 9. Reduced loads, torques and transverse ply stresses for the cyclic loading of tubular specimens under two biaxiality ratios. Red cells indicate stresses beyond the corresponding ultimate strength.

σ_2 / F_{2c}	P [N]	σ_2 [MPa]	$T^{0.40}$ [N·m]	$\sigma_6^{0.40}$ [MPa]	$T^{0.21}$ [N·m]	$\sigma_6^{0.21}$ [MPa]
1.00	-7609	-163.62	-26.75	-66.18	-14.29	-34.83
0.90	-6848	-147.26	-24.08	-59.57	-12.86	-31.35
0.80	-6087	-130.90	-21.40	-52.95	-11.43	-27.87
0.70	-5326	-114.53	-18.73	-46.33	-10.00	-24.38
0.60	-4565	-98.17	-16.05	-39.71	-8.57	-20.90
0.50	-3805	-81.81	-13.38	-33.09	-7.15	-17.42
0.40	-3044	-65.45	-10.70	-26.47	-5.72	-13.93
0.30	-2283	-49.09	-8.03	-19.86	-4.29	-10.45
0.20	-1522	-32.72	-5.35	-13.24	-2.86	-6.97
0.10	-761	-16.36	-2.68	-6.62	-1.43	-3.48

3.2 Finite Element Simulation of Tube Stresses

To determine the validity of modelling curved structures using classical laminate theory, finite element simulations of an arbitrary tubular specimen was performed using Abaqus/CAE 6.14-2. The tube geometry was modelled using solid, linear hexahedral elements, giving the tube a gauge length of 55 mm and ply thicknesses outlined in Table 10. The unidirectional and fabric plies were modelled as homogeneous linear-elastic materials, using the experimentally-obtained properties in Table 25 and Table 26 (Section 5.1.4). The unidirectional and fabric plies contained five and twenty through-thickness elements, respectively, while the length and circumference of the tube comprised 100 and 200 elements, respectively. One face of the tube was fixed, and the load and torque were applied to a reference point concentric and pin-constrained to the opposing tube face. From the results in Section 3.1, the loads and torques required to induce static shear failure under $\lambda_{12} = 0.40$ respectively were applied to a tube, and through-thickness stresses within the walls were probed (summarized in Table 11).

Table 10. Ply dimensions of the laminate tube modelled in Abaqus.

Ply	Inner Radius [mm]	Outer Radius [mm]
Inner fabric ply (0_F)	9.50	9.59
Transverse ply (90_2)	9.59	10.14
Outer fabric ply (0_F)	10.14	10.23

Table 11. Loads, torques and stresses in a tube at ply-level static shear failure.

Load at F_6	-4930 N
Torque at F_6	-17.06 N · m
σ_2 at F_6	-104.07 MPa
σ_6 at F_6	-42.09 MPa

Figure 22, Figure 23, and Figure 24, plot the results as global stresses, resulting in the discontinuities at the ply boundaries (radii 9.59 mm and 10.14 mm). As detailed in Section 3.1.3, applied torques are defined in terms of the stresses they induce at the outer transverse ply radius R_{90}.

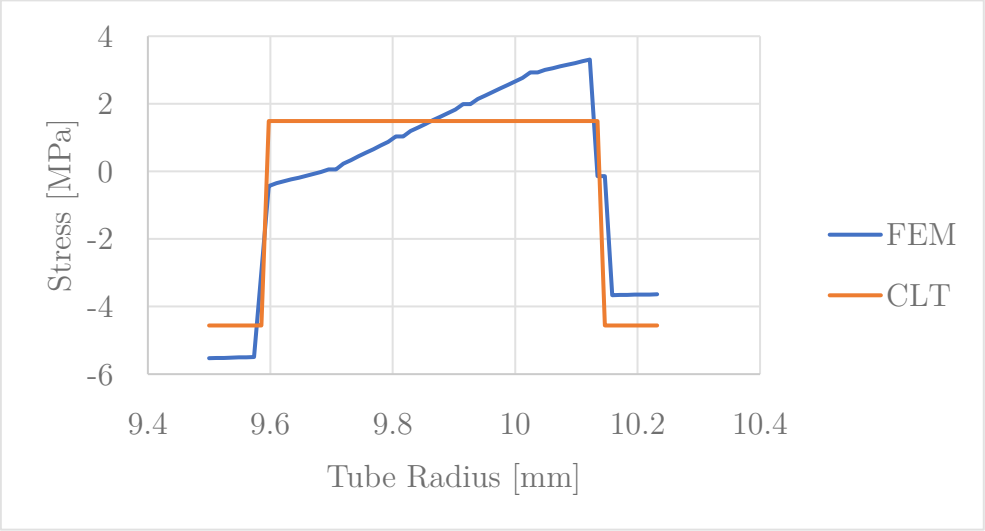

Figure 22. Through-thickness hoop stress (σ_2 in the 0° plies, σ_1 in the 90° plies).

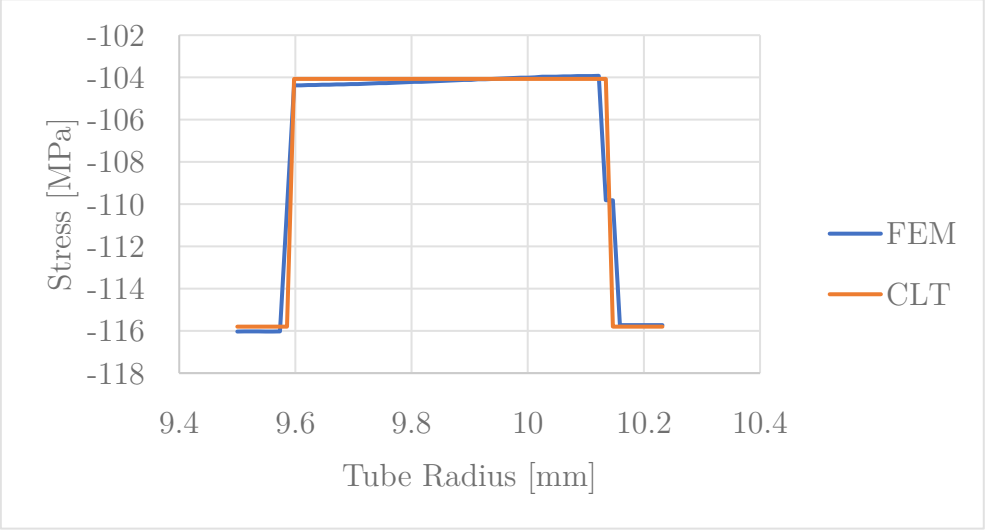

Figure 23. Through-thickness axial stress (σ_1 in the 0° plies, σ_2 in the 90° plies).

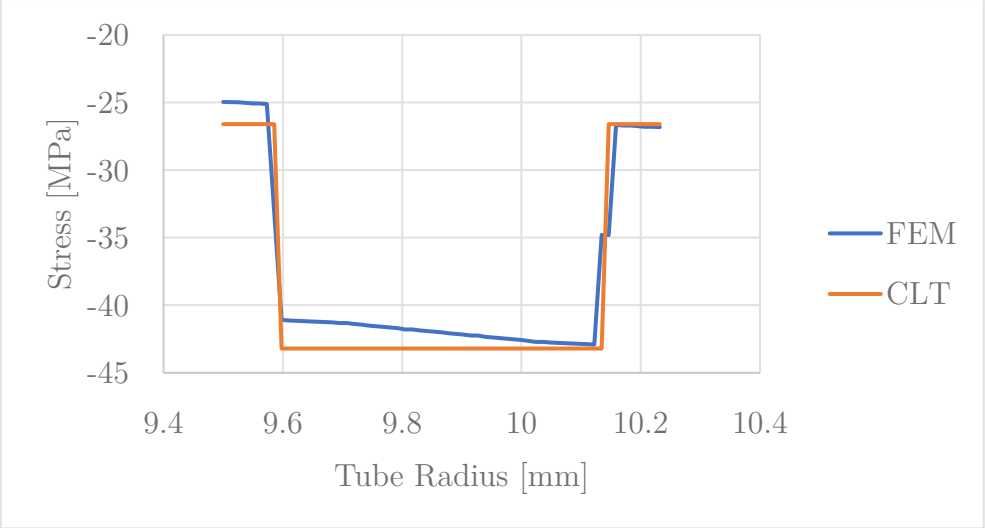

Figure 24. Through-thickness shear stress (σ_6 in the 0° and 90° plies).

3.3 Buckling Calculations

One of the biggest issues facing compression experimentation is buckling, which introduces geometry-specific deformation which prevents proper observation of underlying material properties. It is therefore necessary to design specimens such that their failure loads do not exceed their critical buckling loads. In the case of composite laminates, this includes not only specimen geometry, but the ply layup as well. In cases where constraints such as laminate thickness prevent such designs, anti-buckling fixtures can be incorporated into the test. Specifications of the anti-buckling fixtures used in this investigation can be found in Section 4.3.

3.3.1 Coupon Buckling

Evaluation of the coupons' critical buckling loads was performed using a modified Euler column buckling model presented in Ref. [82]:

$$P_{cr} = \frac{\pi^2 EI}{(KL)^2} \tag{31}$$

$$I = \frac{bh^3}{12}$$

where E is the elastic modulus of an isotropic material, I is the cross-sectional moment of inertia (defined for a rectangular cross-section), b is the specimen width, L is the column length, and K is the effective length factor, governed by the beam's boundary conditions. For a laminate beam, the isotropic modulus E is replaced by the beams' out-of-plane bending modulus E_x:

$$E_x = \frac{12}{h^3 D_{11}^*} \tag{32}$$

where h is the thickness of the laminate, and D_{11}^* is the first element of the inverted bending stiffness matrix D. The effective length term, K, which varies depending on the

boundary conditions imposed on the buckling column, remains unchanged between Euler buckling analysis of homogeneous and laminate columns. In the case of the flat coupons tested in this work, the effective length term is 0.5 due to the clamped boundary conditions. The final expression for the buckling of an orthotropic laminate is:

$$P_{cr} = \frac{\pi^2 b}{(KL)^2 D_{11}^*} \tag{33}$$

Assuming a width of 15 mm and an average ply thickness 0.30 mm respectively, the critical buckling loads of the unidirectional and multidirectional coupons over a range of gauge length were evaluated (layups: $[0_{12}]$, $[90_{12}]$, $[0/65/0/-65]_S$ and $[0/75/0/-75]_S$). The results are tabulated in Table 12.

Table 12. Summary of allowable specimen lengths for different coupon layups.

Specimen Layup	Static Failure Load [kN]	Static Failure Type	Max. Gauge Length [mm]
$[0_{12}]$	34.235	F_{1C}^{0}	54
$[90_{12}]$	8.833	F_{1C}^{90}	63
$[0/65_2/0/\text{-}65_2]_S$	11.350	F_{6}^{65}	77
$[0/75_2/0/\text{-}75_2]_S$	15.315	F_{2c}^{75}	67

The results presented in Table 12 show that the maximum allowable gauge length is in the range of 50 – 80 mm. However, during all quasistatic and cyclic tests performed without anti-buckling fixtures, specimens buckled regardless. This suggests that either the formula is not accurate, the material properties were not the same as those assumed (due to issues such as fibre misalignment [14]), or additional exterior factors such as test frame misalignment played roles not initially considered.

3.3.2 Tube Buckling

Determination of the critical buckling load of the tubular specimens required substantially more complex calculations than those for the beam-like coupons. Since a hollow-cylinder cannot be as easily supported with a simple fixture as a rectangular specimen, calculations of the critical buckling load for the tubes was of critical importance. Three different approaches were considered to evaluate this load [83,84]. In each case, the gauge length of the tube L was assumed to be 75 mm, while the mean radius R was 10.01 mm.

The Behaviour of Structures Composed of Composite Materials by Vinson and Sierakowski presents a general framework for the buckling of thin cylindrical shells, as well as another set of equations specifically for symmetric laminate cylindrical shells [83]. Additional formulas exist to account for the effects of torsion on buckling, though the tubes being considered did not meet the criteria for the use of these formulae. However, torsion is not believed to be a significant factor in buckling. Additionally, these formulas assume boundary conditions in which the ends of the tube are free to rotate (analogous to a pin-pin connection in a buckling beam). Consequently, these values are conservative estimates for the purposes of this investigation, as the tubular specimens will be clamped to the testing frame, providing substantially improved buckling resistance. The formulas for the general case are as follows:

$$N_x^{cr} = \left(\frac{L}{m\pi}\right)^2 \frac{\begin{vmatrix} C_{11} & C_{12} & C_{13} \\ C_{21} & C_{22} & C_{23} \\ C_{31} & C_{32} & C_{33} \end{vmatrix}}{\begin{vmatrix} C_{11} & C_{12} \\ C_{21} & C_{22} \end{vmatrix}} \tag{34}$$

$$C_{11} = A_{11}\left(\frac{m\pi}{L}\right)^2 + A_{66}\left(\frac{n}{R}\right)^2$$

$$C_{22} = A_{22}\left(\frac{n}{R}\right)^2 + A_{66}\left(\frac{m\pi}{L}\right)^2$$

$$C_{33} = D_{11}\left(\frac{m\pi}{L}\right)^4 + (4D_{66} + 2D_{12})\left(\frac{m\pi}{L}\right)^2\left(\frac{n}{R}\right)^2 + D_{22}\left(\frac{n}{R}\right)^4 + \frac{A_{22}}{R^2} + \frac{2B_{22}}{R}\left(\frac{n}{R}\right)^2 + \frac{2B_{12}}{R}\left(\frac{m\pi}{L}\right)^2$$

$$C_{12} = C_{21} = (A_{12} + A_{66})\left(\frac{m\pi}{L}\right)\left(\frac{n}{R}\right)$$

$$C_{23} = C_{32} = (B_{12} + 2B_{66})\left(\frac{m\pi}{L}\right)^2\left(\frac{n}{R}\right) + \frac{A_{22}}{R}\left(\frac{n}{R}\right) + B_{22}\left(\frac{n}{R}\right)^3$$

$$C_{13} = C_{23} = \frac{A_{12}}{R}\left(\frac{m\pi}{L}\right) + B_{11}\left(\frac{m\pi}{L}\right)^3 + (B_{12} + 2B_{66})\left(\frac{m\pi}{L}\right)\left(\frac{n}{R}\right)^2$$

$$P_x^{cr} = 2\pi R * N_x^{cr}$$

while the formulas for the symmetric laminate case ($B_{ij} = 0$) are as follows:

$$N_x^{cr} = \left(\frac{D_{11}\pi^2}{L^2}\right) * \left[m^2\left(1 + 2\frac{D_{12}}{D_{11}}\beta^2 + \frac{D_{22}}{D_{11}}\beta^4\right) + \left(\frac{\gamma^2 L^4}{\pi^4 m^2 D_{11} R^2}\right)\left(\frac{A_{11}A_{22} - A_{12}^2}{A_{11} + \left(\frac{A_{11}A_{22} - A_{12}^2}{A_{66}}\right)\beta^2 + A_{22}\beta^4}\right) \right] \tag{35}$$

$$\beta = \frac{nL}{\pi R m} \quad , \quad \gamma = 1 - 0.901(1 - e^{-\phi}) \quad , \quad \phi = \frac{1}{29.8}\left[\frac{R}{\left(\frac{D_{11}D_{22}}{A_{11}A_{22}}\right)^{\frac{1}{4}}}\right]^{\frac{1}{2}}$$

$$P_x^{cr} = 2\pi R * N_x^{cr}$$

where A_{ij}, B_{ij} and D_{ij} are elements of the laminate's stiffness matrices. In both cases, m is the number of *half waves* in the axial direction, and n is the number of *waves* in the circumferential direction. A knockdown factor γ exists to reconcile differences between calculated buckling load values, and those determined experimentally. Consequently, N_x^{cr} calculated in the symmetric case is expected to be smaller.

Optimization is required to determine the integer values for m and n that produce the lowest N_x^{cr} value, showing in Figure 25. While beams buckle at the lowest buckling mode ($m_{beam} = 1$), the critical buckling modes of a cylinder can vary significantly based on the ratios of length, radius, and thickness.

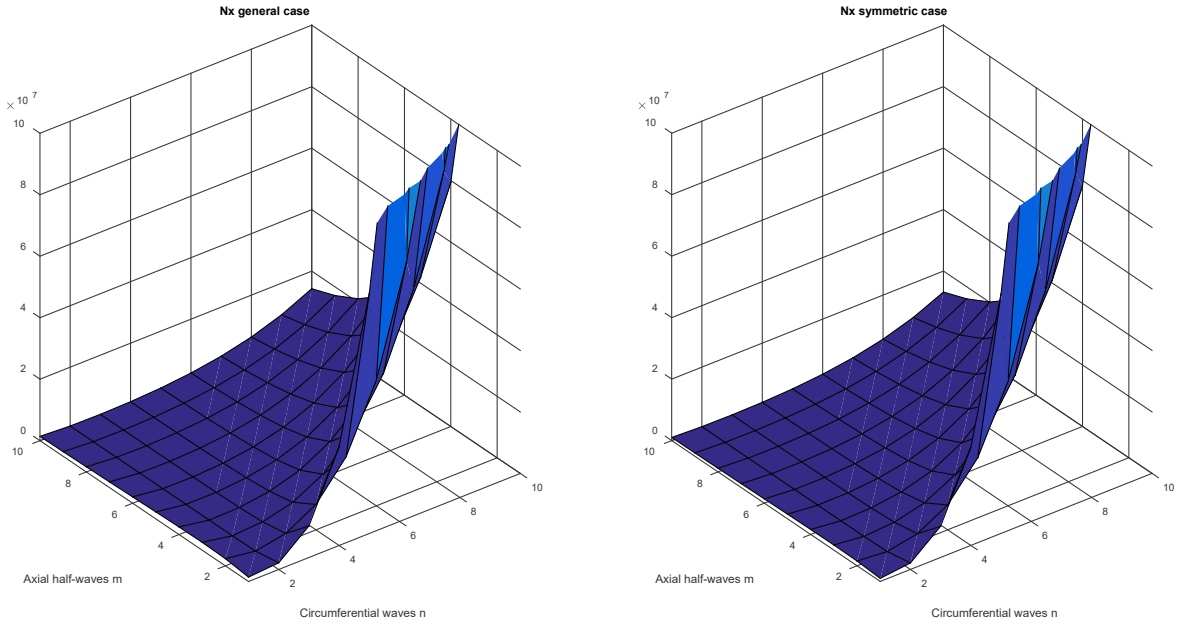

Figure 25. Critical buckling loads N_x with varying axial and circumferential buckling modes.

For the general case, the m and n buckling modes which produce the lowest buckling load were 8 and 3, producing a buckling load of 45.20 kN. For the symmetric case, the m and n buckling modes which produce the lowest buckling load were also 8 and 3, producing a buckling load of 32.95 kN. With a predicted compressive failure load of 7.7 kN, the probability of tube buckling during testing, especially fatigue testing, is negligible.

Simple Formulas and Results for Buckling-Resistance and Stiffness Design of Compression-Loaded Laminate-Composite Cylinders by Nemeth and Mikulas provided another method for estimating the critical buckling load of the cylindrical specimens [84]. The preliminary steps of this method involve the simplification of the laminate layup into a single homogenized ply:

$$\tilde{Q} = \sum_{k=1}^{n} \bar{Q}_k \left(\frac{t_k}{t}\right) \tag{36}$$

$$\tilde{E}_x = \tilde{Q}_{11} - \frac{\tilde{Q}_{12}^2}{\tilde{Q}_{22}} \qquad \tilde{E}_y = \tilde{Q}_{22} - \frac{\tilde{Q}_{12}^2}{\tilde{Q}_{11}} \qquad \tilde{\nu}_{xy} = \frac{\tilde{Q}_{12}}{\tilde{Q}_{22}} \qquad \tilde{\nu}_{yx} = \frac{\tilde{Q}_{12}}{\tilde{Q}_{11}} \qquad \tilde{G}_{xy} = \tilde{Q}_{66}$$

$$\beta = \frac{\tilde{Q}_{12} + 2\tilde{Q}_{66}}{\sqrt{\tilde{Q}_{11}\tilde{Q}_{22}}} \qquad \mu = \frac{\tilde{Q}_{11}\tilde{Q}_{22} - \tilde{Q}_{12}^2 - 2\tilde{Q}_{12}\tilde{Q}_{66}}{2Q_{66}\sqrt{\tilde{Q}_{11}\tilde{Q}_{22}}} \qquad \rho = \frac{R}{t}\sqrt{1 - \left(\frac{\tilde{Q}_{12}^2}{\tilde{Q}_{11}\tilde{Q}_{22}}\right)}$$

$$\lambda_{12} = \left[\frac{(1+\beta)(1+\mu)}{3\rho^2}\right]^{\frac{1}{4}} = \frac{1}{n_{cr}}$$

$$I_{n,cr} \equiv \textit{closest integer to } n_{cr}$$

$$\varepsilon = \frac{I_{ncr} - n_{cr}}{n_{cr}}$$

$$\sigma_x^{cr} = \frac{1}{2}\sqrt{\frac{2\tilde{G}_{xy}\sqrt{\tilde{E}_x\tilde{E}_y}}{3\left(1 - \sqrt{\tilde{\nu}_{xy}\tilde{\nu}_{yx}}\right)}\left(1 + 2\varepsilon + \varepsilon^2 + \frac{1}{1 + 2\varepsilon + \ \varepsilon^2}\right)\frac{t}{R}} \ , \quad P_x^{cr} = \ \sigma_x^{cr}\pi(R_0^2 - R_i^2)$$

where β, μ and ρ are non-dimensional geometric parameters of the tube, $\tilde{E}_x$, $\tilde{E}_y$, $\tilde{G}_{xy}$, $\tilde{\nu}_{xy}$, $\tilde{\nu}_{yx}$ and $\tilde{Q}$ are the elastic constants and reduced stiffness matrix of the homogenized laminate in the universal coordinate system, t is the laminate thickness, R is the mean radius of the tube.

These equations produce a critical buckling load of 45.85 kN, which is close to the 45.2 kN as predicted by the general case in [83]. Given that these are conservative estimates (fixed boundary conditions are not accounted for), and the predicted failure load of 7.7 kN, it is unlikely that buckling of the cylinders will occur before individual plies begin to fail.

4 Experimental Program

4.1 Specimen and Material Specifications

4.1.1 Material Specifications

Two E-glass/epoxy prepregs, one unidirectional and the other a woven fabric, were obtained from Composite Materials Italy, a part of the Toray Group. The unidirectional prepreg, UE400-REM, was used for both the flat coupon specimens and the tubular specimens. The woven fabric prepreg, EE106-ET443, was used as an internal and external support layer for the tubular specimens to prevent unstable crack propagation during cyclic loading. These prepregs are the same materials as those used in Ref [16]; their selection in this investigation was based on providing a more consistent basis on which to compare results between the two studies. Prepreg datasheets are available in Appendix A.

4.1.2 Processing Parameters

Rolls of both the woven and unidirectional prepregs were sent to the National Research Council in Ottawa, where the material was processed into thirteen flat panels and twenty cylinders, with layups and dimensions discussed in Section 4.1.3

For the preparation of the flat panels, prepreg plies were cut from the thawed rolls and hand-laid on a base plate, and debulked for ten minutes after every other layer. Shims were placed around the ply stack to control the thickness of the finished laminate. A Teflon-wrapped caul plate, used to distribute temperature and pressure uniformly over the laminate, was placed on the stack. A perforated non-stick Teflon sheet was taped to the entire based plate. Two layers of breather were placed on the plate, and the entire plate was inserted into a vacuum bag with two ports (one for the vacuum source, and

the other for a pressure meter). The panels were then inserted into the autoclave and processed with the curing cycle shown in Figure 28.

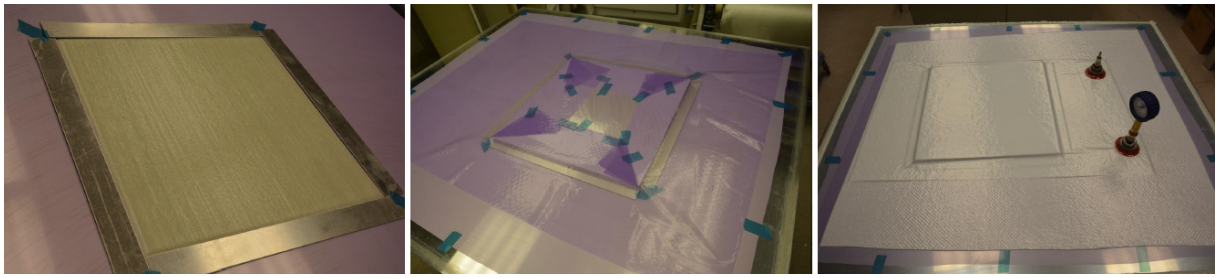

Figure 26. Steps during panel manufacturing. From left to right: ply-by-ply layup of prepreg in shims, layering of perforated Teflon over caul plate and plies, and application of vacuum over plies and breather.

The cylinders were processed in a similar manner to the panels, with several additional steps. An aluminum mandrel was cleaned with isopropanol and coated with non-stick Loctite Frekote FMS. Prepregs were individually wrapped around the mandrel with minimal overlap. Each ply was offset to distribute the overlaps around the tube. The tubes were debulked for ten minutes in a vacuum bag. Tool coat tape was rolled around the mandrel at the edges of the prepregs to act as a dam for bleeding resin. The tubes were hand-wrapped with 1" wide shrink tape in two layers, with each section having ¾" of overlap. A peel ply was rolled as a bleeder to absorb excess resin, and the tubes were wrapped in perforated Teflon and breather. The tubes were inserted into a vacuum bag and cured in the autoclave with the curing cycle shown in Figure 28. Autoclave processing was implemented because the high curing pressure improves the efficiency with which gases are removed from the specimen, resulting in specimens with fewer voids [1].

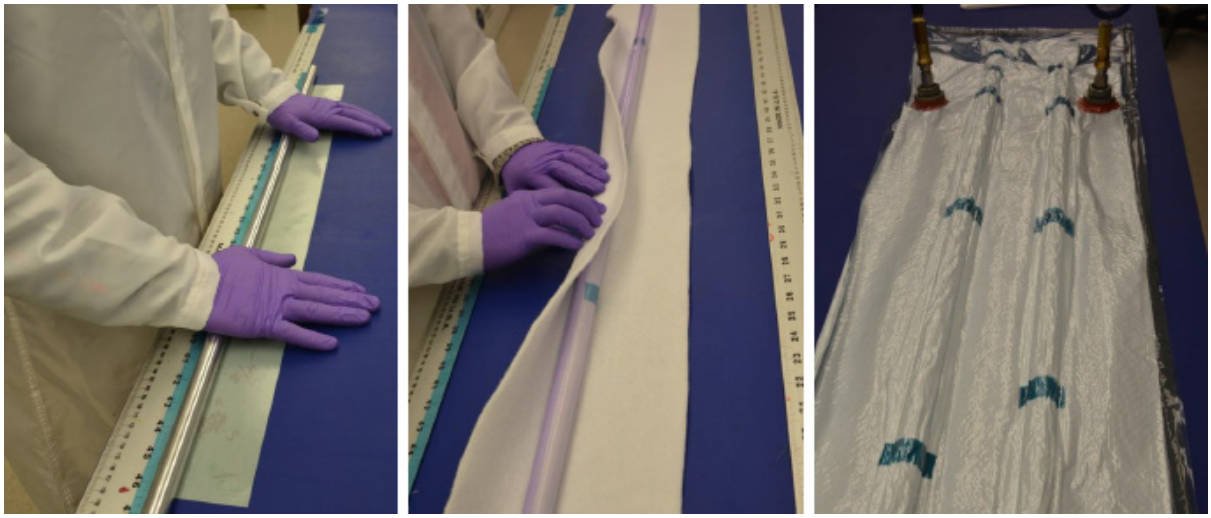

Figure 27. Steps during cylinder manufacturing. From left to right: ply-by-ply wrapping of prepregs on mandrel, wrapping of breather and perforated Teflon around cylinders, and application of vacuum bagging prior to autoclave curing.

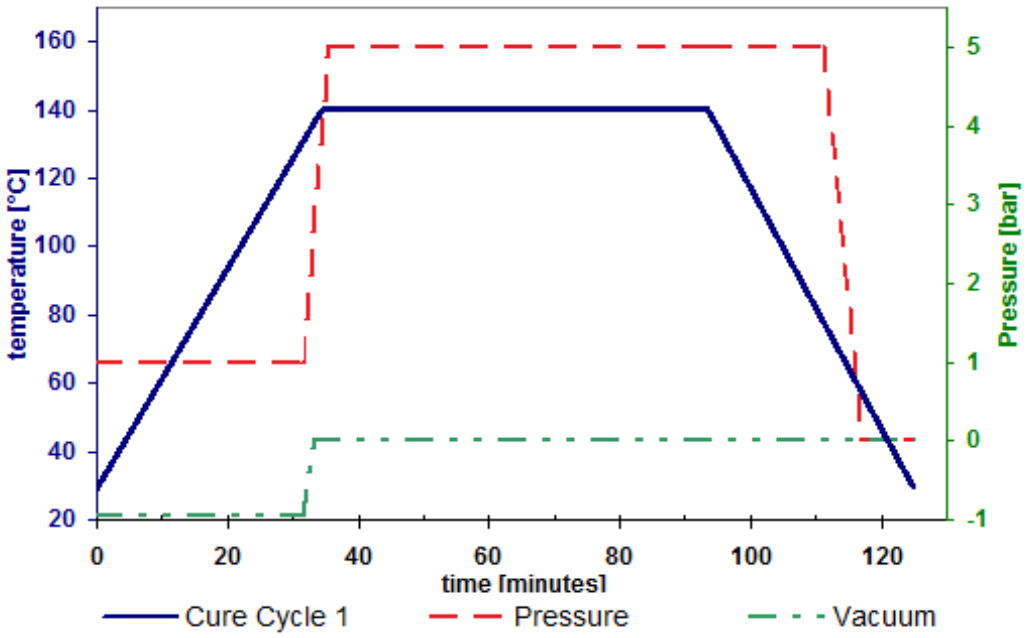

Figure 28. Autoclave curve cycle for the panels and tubes.

4.1.3 Specimen Specifications

4.1.3.1 Coupons

A total of thirteen 15" x 15" panels were prepared at the National Research Council, with layups and internal diameters listed in Table 13. Unidirectional and multidirectional coupons were waterjet cut from the prepared panels with dimensions in accordance with ASTM standards (outlined below in Table 14 and Table 15). Waterjet cutting and other abrasive machining methods (such as the use of cutoff saws discussed in Section 4.1.3.2) were reported and observed to not introduce damage within the specimens.

Table 13. Flat panel layups and designations.

Panel Layup	Panel ID
$[0_6]$	UD-Thin1
$[0_6]$	UD-Thin2
$[0_{12}]$	UD-Thick
$[45_{12}]$	UD-Shear
2x $[0_2/65_2/0_2/-65_2]_S$	MD16-65
$[0_2/70_2/0_2/-70_2]_S$	MD16-70
2x $[0_2/75_2/0_2/-75_2]_S$	MD16-75
2x $[0/65/0/-65]_S$	MD8-65
2x $[0/75/0/-75]_S$	MD8-75

Table 14. Unidirectional coupon dimensions and relevant ASTM standards.

Specimen Type	Length	Width	ASTM Reference
Long. Tens.	254 mm	15 mm	ASTM D3039
Trans. Tens.	178 mm	25 mm	ASTM D3039
Long. Comp.	137 mm	10/12 mm	ASTM D6641*
Trans. Comp.	137 mm	10/12 mm	ASTM D6641*
In-Plane Shear	229 mm	25 mm	ASTM D3518

*Alignment fixtures were not available for use in compression testing.

Table 15. Multidirectional and cyclically-loaded coupon dimensions.

Specimen Type	Length [mm]	Width [mm]
QS-$[0/65/0/-65]_S$	137 mm	15 mm
QS-$[0/75/0/-75]_S$	137 mm	15 mm
Cyc-$[0_{12}]$	137 mm	15 mm
Cyc-$[0/65/0/-65]_S$	137 mm	15 mm
Cyc-$[0/75/0/-75]_S$	137 mm	15 mm

4.1.3.2 Tubes

A Mastercraft wet tile saw was used to section the large cylinders into tube specimens. It is reported in the literature that toothed saws cause substantial damage to the composite due to the impact of the teeth against the matrix and fibres [17]. The ends of the tubes were then sanded to remove rough edges. It is imperative that a wet tile saw or wet sandpaper be used for preparing fibreglass specimens to prevent the dispersal of harmful glass fibres.

The nominal inner and outer radii of each tube were 9.5 mm and 10.23 mm (determined via optical microscopy). Tubes were initially sectioned to lengths of 125 mm, comprising a 75 mm gauge length and two 25 mm areas for end tabs. Buckling calculations in Section 3.3.2 suggested that the buckling of tubes would not occur at any practical specimen length, so the length of the specimens would be maximized to increase the surface area available for crack observation. However, trial quasistatic tests on the tubes in tension and compression revealed that in compression, cracks only occur in one location, rather than several, shown in Figure 29.

Figure 29. Damage in a tube from tension (left) vs. compression (right).

With large crack viewing areas no longer a priority, specimens were reduced in length due to the limited number of stock tubes (thirteen instead of twenty), thereby increasing the number of available specimens. Additionally, the ubiquity of defects in the cylinders necessitated shorter tubes to reduce the probability of any defects in the tubes. One tube was cut to a 30 mm gauge length, but the proximity of the cup fixtures prevented proper insertion of the tube into the locking assemblies. Specimens could only be inserted partially into the locking assembly, and would then be pressed into place by the loading force of the test frame. Removing these further-shortened specimens from their fixtures was virtually impossible given the lack of space for tools as shown in Figure 30. The shortest practical gauge length that could be used was a 50 mm gauge length, with two 25 mm tabbed ends.

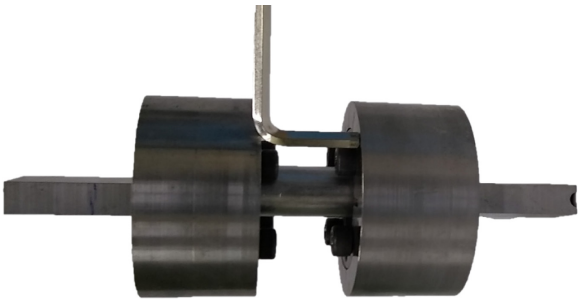

Figure 30. Specimens with a gauge length of 30 mm cannot properly inserted or removed due to the limited space for a standard or ball-end Allen key.

4.2 Material Examination

Upon receiving the panels and cylinders, a quality check of the fibre dispersion, fibre volume fraction, and specimen geometry was performed. The fibre volume fraction V_F of the panels were determined using a combination of mechanical characterization, thermogravimetric analysis (TGA), and optical microscopy, while the fibre volume fraction of the tubes was determined exclusively by optical microscopy.

4.2.1 Fibre Volume Fraction

A critical element of characterizing FRP laminates is the determination of the volume fractions of the fibres, matrix and voids within the material (the latter being a negligible value with autoclave manufacturing). The determination of the fibre volume fractions V_F of the specimens were required to act as corroborating data to support the material properties obtained during quasistatic characterization. The fibre volume fractions were determined using a combination of mechanical characterization, thermogravimetric analysis (TGA), and optical microscopy. Results from quasistatic testing indicated an approximate fibre volume fraction of 58%, based on the rule of mixtures (Equation 1) and the Halpin-Tsai equations.

4.2.1.1 Thermogravimetric Analysis

Thermogravimetric analysis was performed on specimens obtained from unidirectional and multidirectional panels. Table 16 and Table 17 summarize the measurements of the fibre volume fraction in the different panels. It was observed that the average fibre volume fraction within the different panels decreased as the number of plies increased, though a clear correlation could not be drawn due to the limited number of TGA specimens per panel.

Table 16. Fibre volume fractions of the unidirectional panels obtained by thermogravimetric analysis.

Specimen	Panel	Fibre Volume Fraction [%]
Oldthin-1	UD-Thin1	61.7
Oldthin-2	UD-Thin1	49.6
Newthin-1	UD-Thin2	58.4
Newthin-2	UD-Thin2	60.2
Thick-1	UD-Thick	51.4
Thick-2	UD-Thick	55.9
Shear-1	UD-Shear	57.4
Shear-2	UD-Shear	59.3

Table 17. Fibre volume fractions of the multidirectional panels obtained by thermogravimetric analysis.

Specimen Name	Panel	Fibre Volume Fraction [%]
MD16-65-1	MD16-65	48.2
MD16-65-2	MD16-65	50.0
MD16-65-3	MD16-65	58.9

Thermogravimetric analysis could not be performed on the tubes due to the presence of the interior and exterior glass fabric layers, which have narrower glass fibres, and their own unique volume fractions.

4.2.1.2 Optical Microscopy

Without the use of TGA, an alternative method was required to determine the fibre volume fraction of the transverse tube plies. Because the panels contain continuous fibres, an areal volume fraction of the tubes measured by optical microscopy would be an accurate representation. Specimens from different cylinders were ground and polished and examined under a microscope. A sample image is shown below in Figure 31.

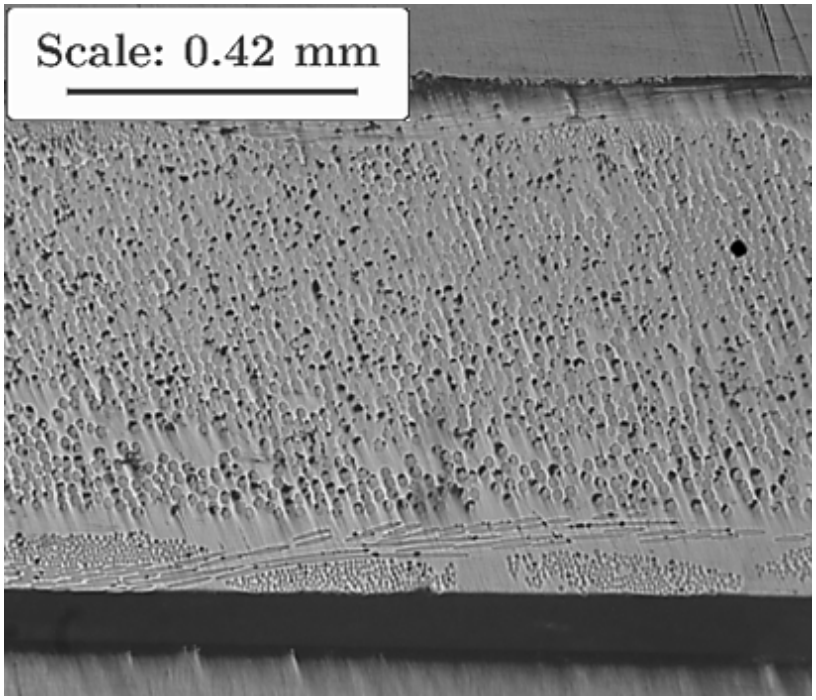

Figure 31. Microscope image of tube wall, showcasing the difference in fibre diameter and grouping with the 90° (centre) plies and the fabric plies (top and bottom).

Due to the visual similarity between the glass fibres and epoxy matrix, post-processing could not provide sufficient contrast for software to determine the fibre volume fraction by thresholding. Similarly, MATLAB was unable to detect the circular fibres with the *imfindcircles* function. To address this issue, individual fibres in each image were manually dotted with white circles using Paint 3D, which *imfindcircles* could detect, shown in Figure 32. While this process requires a significant time contribution by the researcher, it eliminates the tedium and potential source of human error associated with counting manually. The total fibre area was obtained by multiplying the fibre count by an average fibre area measurement, and the final fibre volume fraction was obtained by dividing that area by the image area. This method produced volume fraction measurements consistently 5% lower than those obtained by TGA, based on results obtained by dotting images of the unidirectional panels. Accounting for this error, the fibre volume fraction of the 90° plies in the tubes is nominally 63.8%.

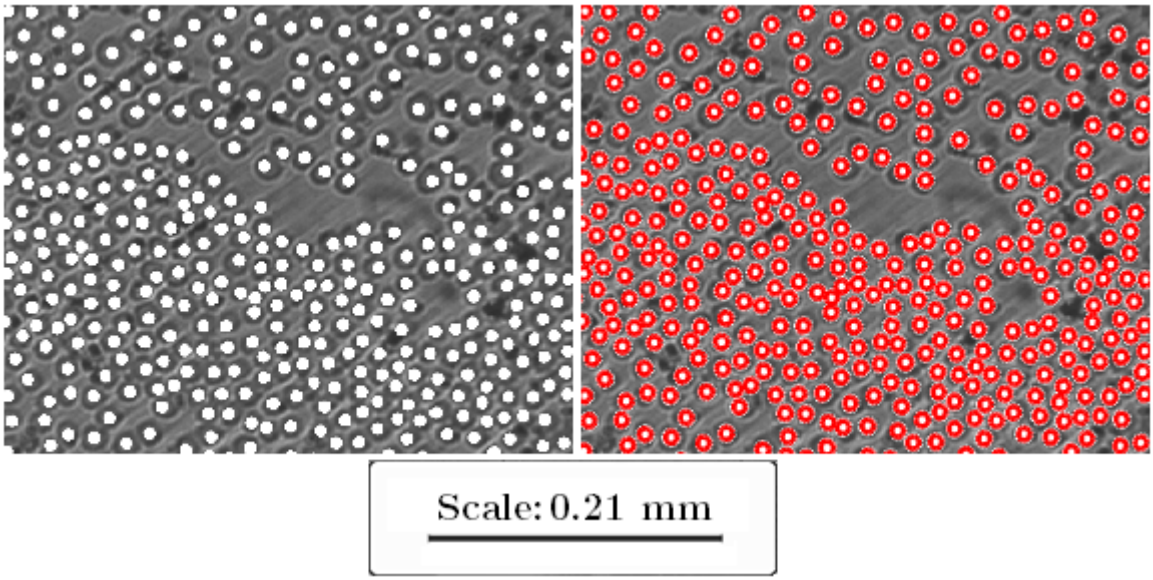

Figure 32. Manually dotted microscope image (left), and the dots counted by MATLAB's *imfindcircles*, with highlighting function *viscircles* employed as a visual error check (right).

Based on the results obtained, it is evident that the volume fraction of fibres varies between specimens cut from different stock material (panels or cylinders), despite their theoretical similarities based on their processing parameters.

4.2.2 Material Quality Inspection

In addition to verifying the fibre volume fraction of the material, another critical component to the initial examination is the evaluation of material defects. Defects include voids in the matrix, resin-rich areas, notable non-uniformity of glass fibre radii, poor fibre distribution within the matrix, and changes in ply thickness.

Specimens from the same source panel or cylinder where considered to have the same nominal properties. However, the ply thickness (and thus the true material properties) from specimen to specimen varied substantially.

Table 18. Changes in ply thickness relative to the number of plies within a panel. The relationship is virtually linear ($R^2 = 0.9405$).

Panel	Number of Plies	Average Ply Thickness [mm]
UD-Thin1	6	0.26
UD-Thin2	6	0.27
UD-Thick	12	0.29
UD-Shear	6	0.27
MD16-65	16	0.32

It appears that despite being processed in theoretically identical conditions, the average ply thickness is different between laminates with different numbers of plies. These measurements corroborate the thermogravimetric measurements of the fibre volume fraction in the panels, which were smaller in the thicker panels. It appears that the thicker panels did not bleed sufficient resin to maintain the same ply thickness as their thinner counterparts. As mentioned previously, the change in average ply thickness did affect the fibre volume fraction of the laminates. However, due to insufficient time and material to establish material properties for a range of fibre volume fractions, the material properties obtained from quasistatic test were accepted as nominal values for all specimens.

The twenty cylinders were prepared in two batches, the first of seven, and the latter of thirteen. The first batch was prepared using a similar recipe to that in Figure 28, but with a dwell temperature of 125°C. The initial cylinders exhibited poor surface quality, with large ridges and valleys running helically along the length of the tubes. Microscope images indicated that the poor quality of the cylinders was not only on the surface, but within internal layers of the tube as well. The transverse tube plies showed significant variations in ply thickness, as well as a poor distribution of the fibres, shown in Figure 33.

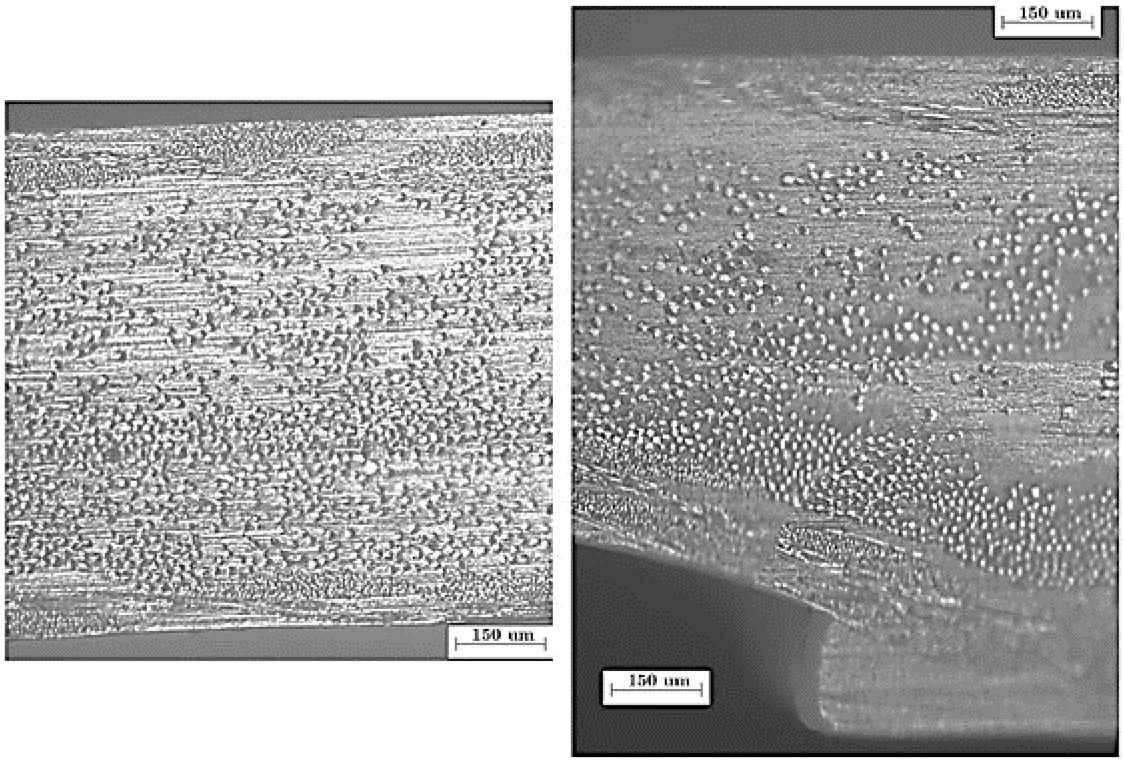

Figure 33. Microscope images of first batch tubes, showing non-uniform fibre distribution (left, right) and inconsistent wall thickness (right).

The second batch of cylinders had notably inferior outer surface quality relative to the first cylinders (see Figure 34). However, optical microscopy revealed that the surface defects were primarily resin-rich areas, or regions with varying woven-layer thickness. The relatively constant thickness of the transverse ply and the uniform fibre distribution (Figure 35) limited the influence of the defects on the specific performance.

Figure 34. Cylinders from the first batch (top) and the second batch (bottom).

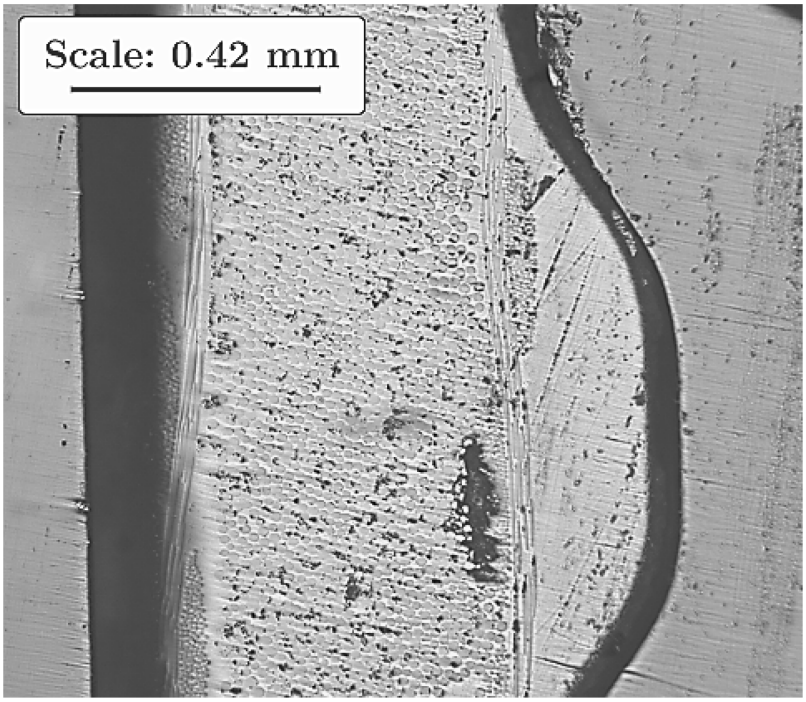

Figure 35. Microscope image of a surface wrinkle in a defective tube specimen. The region has large resin-rich areas extending beyond the outer fabric ply, though the transverse plies show a comparatively minimal change in thickness and curvature.

Tube specimens were cut from the higher-quality batch of thirteen cylinders. Only nine specimens could be cut from areas with no visible defects. Four of these tubes were used for the combined quasistatic tests, and the fifth test was run at an incorrect cyclic stress state ($\lambda_{12} = 0.18$). The combination of a specimen shortage and the nominally acceptable transverse tube plies warranted additional specimens to be cut from areas with minimal surface defects. The nine initial specimens are labelled with the general form CC-#, indicating the tube number cut from a specific cylinder (e.g. 8-3 is the third tube cut from cylinder 8). Similarly, defective specimens are marked CC-X#, with the X indicated the presence of at least one surface defect within the gauge section. Over the course of testing, more additional specimens needed to be cut. With each successive batch of specimens cut from the cylinders, the benchmark for what was considered acceptable quality was lowered further. While the defects in the sample specimens were observed to be surface defects only, it is possible that the performance of the later specimens were worsened by these defects, if only marginally.

4.3 Equipment, Fixtures and Components

4.3.1 Test Frames

Three test frames were used to test the coupons and tubes are listed in Table 19, and shown in Figure 36.

Table 19. Hydraulic test frames.

Test Frame	Axial Capacity	Torsional Capacity	Tests
MTS 810	±50 kN	N/A	Quasistatic tests for unidirectional and multidirectional panels
Instron 8872	±25 kN	N/A	Cyclic tests for unidirectional and multidirectional panels
Instron 8874	±25 kN	±100 N · m	Quasistatic and cyclic tests for tubes

Figure 36. Hydraulic test frames. Left to right: MTS 810, Instron 8872, Instron 8874.

4.3.2 Cup Fixtures and Locking Assembly

Instron jaws capable of accommodating cylindrical specimens with radii of 10.5 mm were not available, warranting the need for a specific fixture to hold the tubes in place using the available jaws. A hardened steel cup fixture was machined to allow the cylindrical specimen and a circular locking assembly to be inserted into the wedge grips of the Instron. The Tollok TLK 350 locking assembly was used to keep the tubular specimens

in the centre of the cup fixture, as well as to prevent their rotation. The locking assembly bolts were tightened using a hex key and torque wrench assembly to a torque value of 10.7 Newton-metres.

To allow a wire for the tube lighting apparatus to enter the tube, one of the fixtures was machined by wire electron discharge machining, as the material was already hardened to 50 RC. A four-millimetre hole was removed down the length of the grip section, and a 5 mm semicircular trench was removed along its based. This port allowed wires to be passed into the tube without comprising the concentricity of the tube and the stability of the locking assembly.

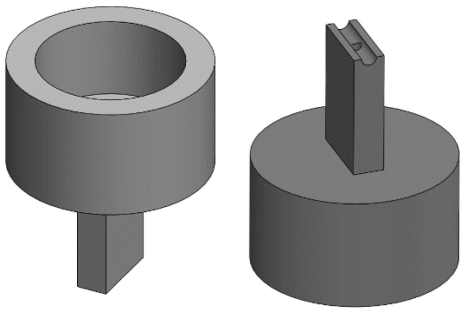

Figure 37. Cup fixtures into which the tube locking assembly was inserted.

Figure 38. Combination of Allen key and torque wrench used to tighten the locking assembly.

4.3.3 Specimen Tabs

The brittle behaviour of composite laminates necessitates the use additional material on the ends of the specimen to prevent any damage from occurring due to the pressure of hydraulic grips. Tabbing material, geometry, and bonding technique vary from source to source in the literature, though rectangular specimens typically have rectangular tabs made from aluminum or steel bonded to the specimen, or additional layers of the composite material cured to the ends.

One of the issues that tabbing introduces is the sliding of the specimen relative to position of the hydraulic cross-heads. This typically occurs at high compressive loads with either the specimen slipping between the tabs, or the tabs sliding against the specimen grips. Bonding the tabs to the specimen using a strong adhesive can prevent specimen sliding. Increasing the grip pressure can prevent both forms of sliding, though this can introduce damage within the gripped area of the specimen. Additionally, increasing grip pressure can introduce stress concentrations at the gauge length boundaries due to the restriction of Poisson effects within the grips but not without, inducing tab-region failure [85,86].

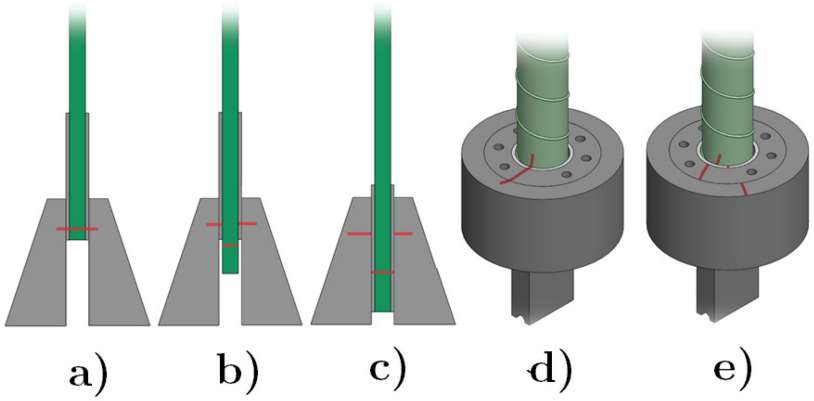

Figure 39. Schematic diagrams of slipping in rectangular and tubular specimens: a) Marked coupon prior to test, b) Tab-specimen slipping, c) Tab-grip slipping, d) Marked tube prior to test, e) Slipping at the interfaces between the tube, shell tab, locking assembly, and cup fixture.

4.3.3.1 Coupon Tabs

Rectangular tabs for the unidirectional and multidirectional coupons were cut from 18-gauge aluminum 3003 using a press shear. Each tab was 1.5 inches long, with a width corresponding to the individual specimen to which they were bonded. The faces of the tabs, as well as their locations on the specimen, were sanded at ±45° using 400 grit sandpaper to improve the contact strength between the two materials. Tabs for quasistatic tension and shear specimens did not require such adhesion to stay in place, and therefore were bound to the specimen using masking tape. To prevent tab slipping during quasistatic and cyclic compression tests, tabs were bonded in place using 3M Impact-Resistance Structural Adhesive, a readily-available two-part structural epoxy. Binder clips were used to produce a uniform bondline, as shown in Figure 40.

Figure 40. Binder clips used on a coupon to ensure a uniform adhesive bondline.

4.3.3.2 Tube Tabs

For the tubular specimens, interior *plug* tabs and exterior *shell* tabs were required to prevent specimen crushing and damage induction by the hydraulic grips, respectively. Using aluminum 6061 round bars, interior tabs were turned to a diameter of 19 mm and snugly slid to the tube ends. However, the exterior surface roughness of the tubes prevented simply boring out aluminum shells and sliding them on. Aluminum 6061 round bars were turned down to a diameter of 25 mm and bored to an inner diameter of 22 mm (a sufficiently large diameter to accommodate large surface defects). The interior surface was scratched with a coarse file, and the voids between the tube and its two shell

tabs were filled with an adhesive. A variety of adhesives were tested, though only all-purpose Krazy Glue was sufficiently non-viscous to be injected using a hypodermic syringe. The shell tabs were permanent once bonded, but the plug tabs could be easily removed to allow the insertion of the internal lighting apparatus.

Using shell tabs with bore diameters larger than the tube meant that during gluing, the tabs could shift or rotate relative to the central axis of the tube, shown in Figure 41.

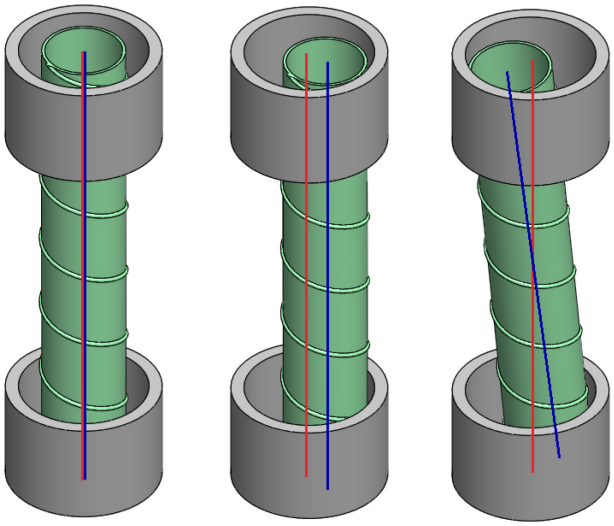

Figure 41. Alignment (left), lateral misalignment (middle), and rotational misalignment (right) present between the tube axis (red) and the shell tabs' axis (blue). Shell tabs are exaggerated in size.

To prevent this misalignment, a specially-designed alignment fixture was used during the tube tab bonding to ensure that the axis of the tube and the tabs were aligned. (Section 4.3.6)

Once the specimens were bonded and removed from the alignment fixtures, hardened droplets of the Krazy Glue were sanded to allow insertion of the specimens into the locking assemblies.

4.3.4 Quasistatic Compression Anti-Buckling fixture

Quasistatic compression tests on specimens from 6-ply and 12-ply panels causes specimens to buckle before fracturing, in contrast to the predictions of the Euler buckling equations discussed in 3.3.1. Specimens were initially cut much shorter, however the distance of the crossheads relative to one another became the limiting factor, as extremely short specimens could not be inserted without the crossheads touching one another. An alternative method to artificially reduce the effective gauge length was to bond long steel tabs to the specimen which extend beyond the range of the wedge grips. This method produced unexpected failure modes (i.e. flat vs. inclined fracture surfaces in transverse compressive specimens) and was thus abandoned. An anti-buckling fixture which could slide along the length of the specimen was obtained so that no part of the specimen was unsupported during testing. Thin Teflon layers were present between the fixture and the specimen to allow movement fixture without rubbing against specimen faces. Figure 42 shows a diagram of the fixture.

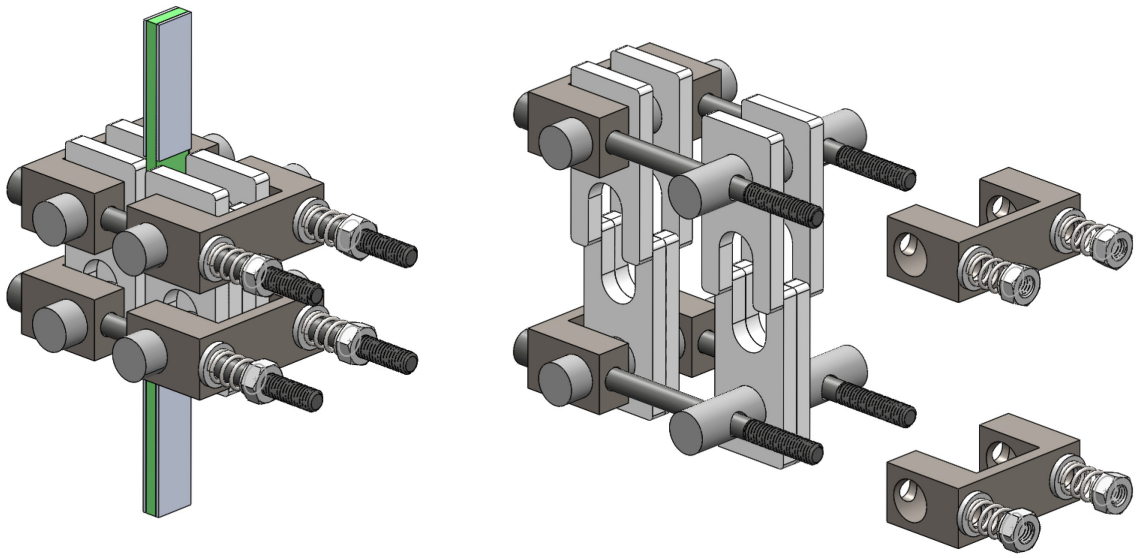

Figure 42. Unexploded (a) and exploded (b) schematic of the anti-buckling fixture used for quasistatic testing. This design could not be easily modified to incorporate a window for crack monitoring.

4.3.5 Windowed Anti-Buckling Fixtures for Rectangular Fatigue Specimens

Rectangular specimens from the thick transverse panel ($\lambda_{12} = 0.00$) and from both multidirectional panels ($\lambda_{12} = 0.21$ and 0.40) were required to characterize the cracking behaviour in different specimen geometries. Quasistatic testing revealed that the rectangular specimens were prone to buckling. However, because crack monitoring was required in these new specimens, the anti-buckling fixture used for quasistatic testing could not be used, as it completely obscured the specimen faces and edges. A windowed anti-buckling fixture was required to allow for crack visualization during testing.

4.3.5.1 Static Windowed Fixture

A windowed anti-buckling fixture was built to prevent buckling of the off-axis coupons during compressive fatigue loading, while still allowing in-situ crack observation.

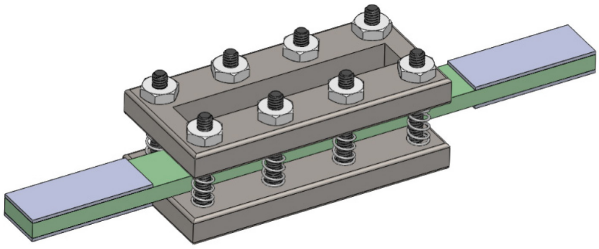

Figure 43. Windowed anti-buckling fixture for rectangular fatigue specimens.

The fixture's single-piece design made the fixture itself incompressible along its length. As a result, small spaces were present between the edges of the fixture and the test frame jaws to prevent loads being transferred through the fixture rather than the specimen. These half-inch spaces were sufficiently long to allow buckling to occur during compression, forcing a new design to be made.

4.3.5.2 Dynamic Windowed Fixture

The second iteration of the windowed design featured two opposing pairs of brackets which can slide along the specimen's length independently of one another, along a low-friction Teflon layer. This movement would allow the fixture to be set in contact with the test frame jaws at the start of the test, eliminating the small space between the fixture and the jaws that could promote buckling. Spaces that were present to allow fixture compression were offset from one another to prevent the entire specimen from buckling. The possibility of local buckling was considered negligible.

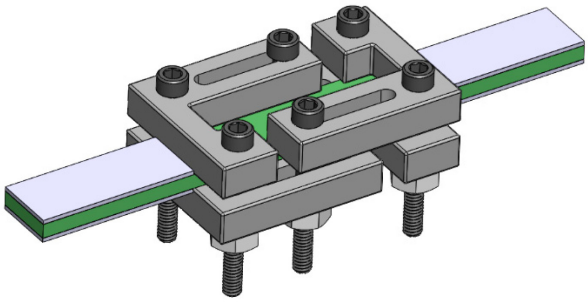

Figure 44. Two-piece windowed anti-buckling fixture for rectangular fatigue specimens.

4.3.6 Tube Alignment Fixture

Four sets of a tube alignment fixture were designed and machined to prevent misalignment of the tube tabs during bonding. Each fixture contains three components, namely one alignment socket and two alignment socket caps. The cold-rolled steel socket was used keep the axes of the two tabs aligned with one another rotationally and laterally.

The two aluminum socket caps each comprised a steel dowel pin and ring fixed to an aluminum base plate. The dowel pin and ring were used to align the axes of the plug tab and tube with that of the shell tab and the alignment socket, respectively. Due to the precise inner diameter of the tubes, the central axes of the plug tabs are colinear

with that of the tube. With a sufficient coating of Vaseline to the different fixture surfaces to ease specimen retrieval and prevent fixture bonding, the tubes were slid into the fixtures, and Krazy Glue was injected into the void between the tube and shell tab through the window in the alignment socket.

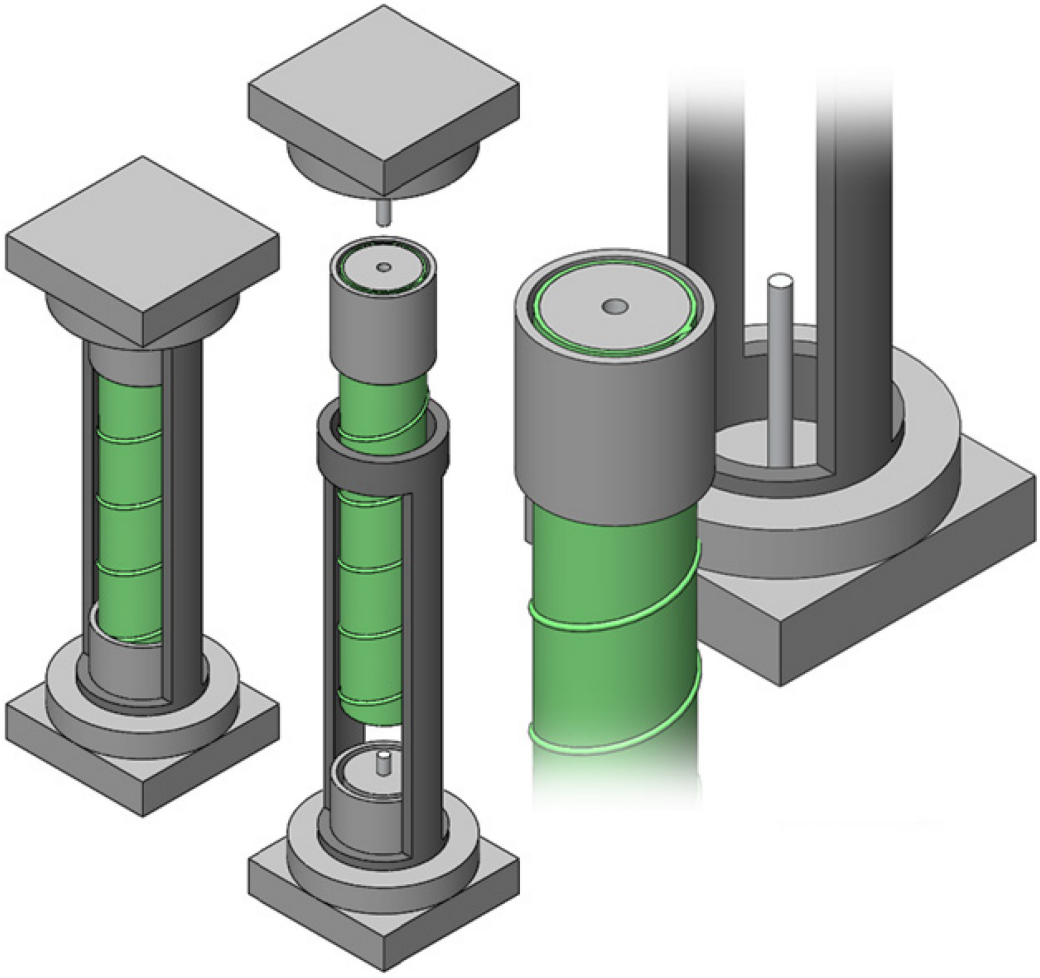

Figure 45. Shell tab alignment fixture, fully assembled in image (a). Image (b) shows how the tube slides into the socket and onto the plug tab, while image (c) highlights the gap between the tube and the shell tab, which is filled with adhesive once the tube is socketed.

Because Krazy Glue is non-viscous, the alignment socket must be upright, meaning that only one tab could be glued at a time. With four sets of fixtures and a curing time of twelve hours, four specimens could have both tabs bonded in one day.

The removal of bonded specimens from the fixtures was an additional issue, since the water-like Krazy Glue flowed into the numerous fixture interfaces. This problem generally surfaced in one of two ways: either the shell tabs were bonded to the alignment socket, or the glue flowed underneath the tube onto plug tab, making it a permanent installation. Because the use of excessive force would damage the tubes, two plunger rods were made to aid in specimen removal. A large steel plunger was made to precisely slide within the alignment socket, only contacting the upper faces of the tube and shell tab. By repeatedly tapping the specimen using the plunger, it would be incrementally pushed out of the socket with relatively minimal force. This is shown in Figure 46.

When the plug tab was stuck inside the removed tube, the cured glue covering the end of the tube was first sanded off, or gently chipped away. Next, with the stuck plug facing downward, the plunger was put into the tube, and the open tube end was covered with the thumb. By repeatedly shaking the tube up and down, the plunger would repeatedly percuss the plug tab, slowly forcing it out. Plunging the plug tabs could be done very forcefully, as the plunger only applies a force to the plug and not the rest of the tube as it slams downward, shown in Figure 47.

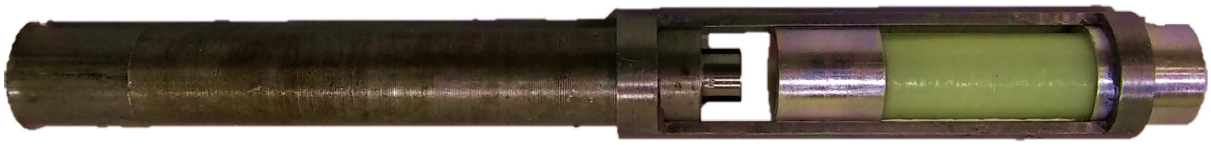

Figure 46. Tube plunger (left) used to remove a tube stuck in the alignment socket (right).

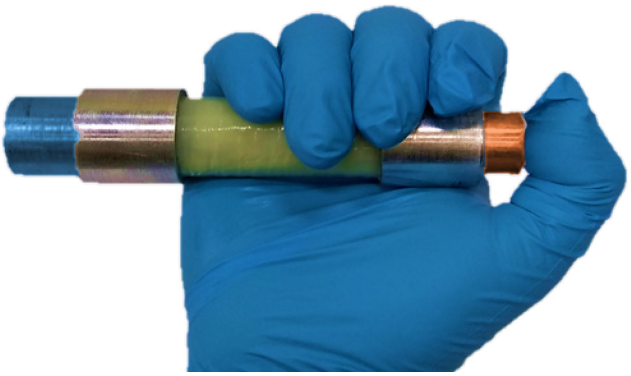

Figure 47. Plug tab plunger (right, orange), repetitively shaken to remove plug tab (left, blue).

4.4 Digital Image Correlation

Strain measurements were obtained from the unidirectional coupons to obtain the moduli and Poisson's ratios of individual lamina. Specimens were speckled with black and white spray-paint to produce a pattern whose distortion was measured using a dual camera setup using ARAMIS software from GOM Correlate.

4.5 Crack-Monitoring Methods

Present in the literature is an extensive variety techniques to characterize cracking behaviour in a composite material. In addition to categorization into *in situ* and *ex situ* methods, these methods can be further subdivided as *global* and *local* methods. Global methods characterize test outputs such as acoustic waves [41,87], electricity resistivity changes [88], and stiffness reductions, which all indicate the presence of cracks, but do not reveal their size and locations. Local methods, such as visual observation, infrared thermography, X-ray tomography [22], and computer tomography [89] can show the exact location of damage occurring within a specimen.

In situ methods are naturally more practical for characterization sub-critical damage mechanisms compared to intermittent *ex situ* characterization, which can be strenuous on the researcher, and introduce more sources of experimental error.

The biggest benefit of glass-epoxy composites compared to carbon-epoxy is that the composite is transparent, which allows visual observation of crack behaviour using an ordinary high-definition camera, rather than a thermal camera.

As a showcase, a FLIR infrared camera was used to observe several quasistatic tests on the tubes, to determine the efficacy of an IR camera to capture *in situ* cracking of the specimen by the heat generated during damage initiation and progression. Thermography would be critical in similar investigations using carbon fibre, since its opacity prevents the optical techniques used herein.

4.5.1 Internal Lighting Assembly

A lighting apparatus which can be inserted inside a tubular specimen is presented in the works of Quaresimin *et al.* [17] and shown in the Figure 48 below. A series of similar devices with the same basic design were tested.

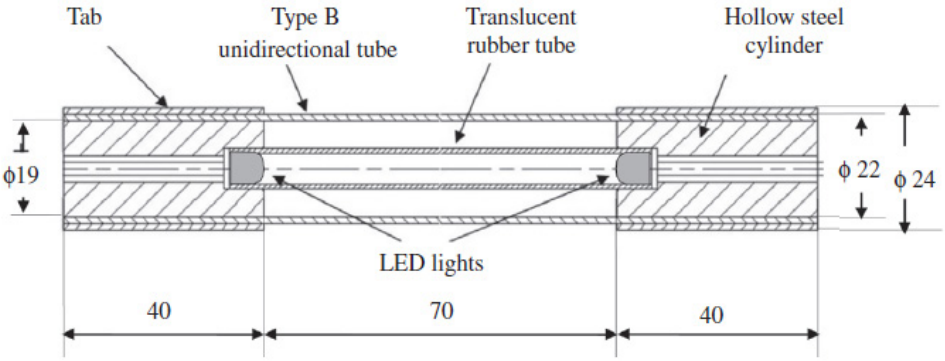

Figure 48. Internal lighting apparatus for tubular specimens, from Ref. [17]. Dimensions given (millimetres) reflect those in the referenced article.

Because a cup fixture and locking assembly were used to insert the tubes into the Instron, the tube was completely encapsulated, necessitating a self-contained (i.e. battery powered) lighting apparatus to operate inside the tube. Due to the small volume within the tube, creating a light sufficiently bright to show cracks and last the duration of a fatigue test was extremely difficult, even using compact lithium polymer batteries. Additionally, space constraints within the tube prevented the light source from radially distributing light, since the battery would obstruct the light on one half of the tube. The device was tested with and without an external light source, but external sources only

reduced the contrast between the specimen and the crack. Based on the issues faced, it was determined that the lighting apparatus must be externally powered. External power would be supplied through a port hole machined into the cup fixtures.

Two devices with different designs were soldered and tested within the tubes to evaluate their efficacies. In the first device, eight 20 mA, 3.1 V white light emitting diodes were wired in two parallel groups of four. The LEDs and the nylon tubes they were glued into were sanded to better diffuse the light. A 12 V source and 72 Ω resistor were wired to the device through a port hole in the cup. Initial fatigue tests were performed using this device with great success due to the device's brightness, however the LED bright spots increased the contrast between different parts of the tube. Consequently, the image processing required to isolate the initiation of a crack was very time consuming. A second device was built based on Figure 48 using a glue stick drilled longitudinally rather than a sanded nylon tube. The glue stick dispersed the light very well, and the reduced brightness was counteracted by increasing the shutter time of the camera. Figure 49 below shows a comparison of images taken with both lighting apparatus.

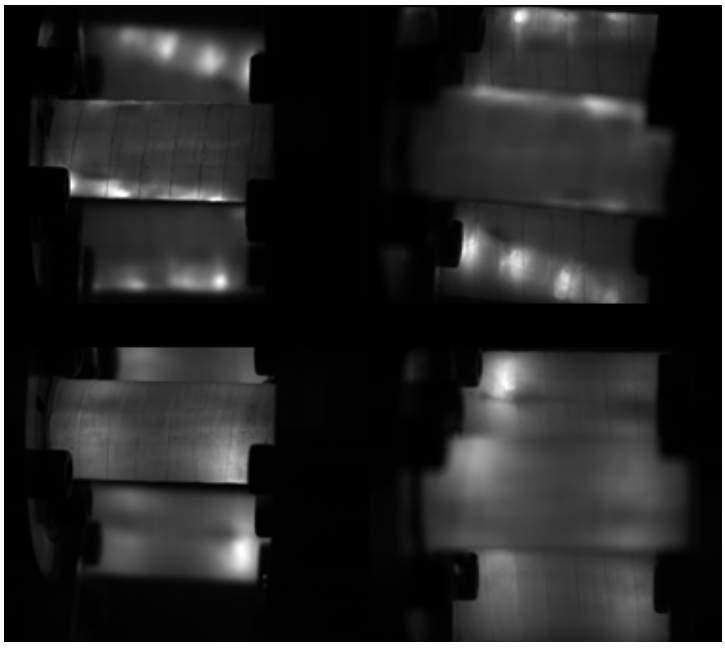

Figure 49. Wired light apparatus Mk I (top pair) and Mk II (bottom pair).

4.5.2 *In situ* Image Capture

A dual-camera apparatus from Correlated Solutions was used to monitor cracking in all specimens. For the coupons, one camera was pointed at the face of the specimens through the windowed anti-buckling fixture, when the second camera faced the narrow edge of the specimen. In addition to providing images of any cracks that may have initiated at that edge, the edge camera also provided a way to more easily determine if and at what loads buckling occurred.

The image capture setup for the tubes was much more complex, however. A complete 360° view of the tube was required to guarantee that the crack initiation locus is within view of the camera. To determine the optimal configuration of the image capture setup, the surface of a reference tube was divided into 45° octants, each containing ticks marking 11.25°, as shown in Figure 50.

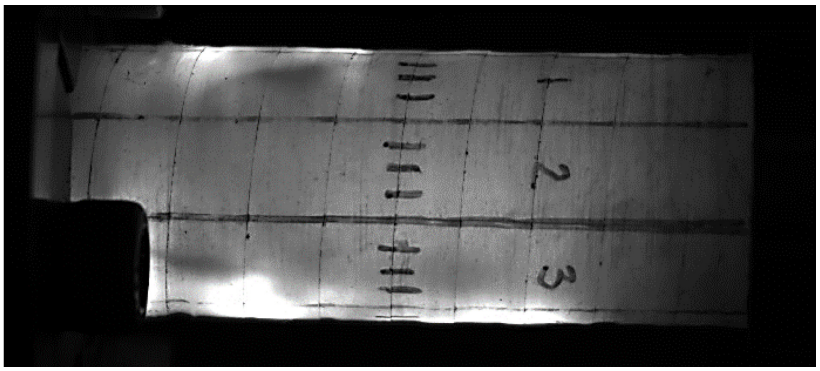

Figure 50. Reference tube image with a visible range of three octants and one tick (146.25°).

The first camera setup had the two cameras directly opposing one another. As shown in Figure 50, only 146.25° of the specimen surface is visible to the camera. Consequently, a maximum of 292.5° can be viewed with this arrangement. Additionally, the most extreme tick on each side of the image is nearly tangential to the light path from the tube to the camera, meaning that the expansion of the crack length in the direction towards the camera could not be measured. This loss of useful data makes only 123.75°

visible to each camera. With two opposing cameras with non-overlapping visible regions, this arrangement reveals only 68.75% of the entire specimen area. Combined quasistatic tests were run using this camera setup, but it was determined that improvements would be required to see the entire specimen.

With the poor efficiency of the first camera arrangement, it was determined that at least one mirror would be required to view the entire specimen area. For the second camera arrangement, two large mirrors were attached to the posts of the test frame. However, the sensitivity of the focal length of the cameras is very high. The distance to the mirrors from the specimen made the reflections both out of focus and out of the narrow field of view of the cameras. Mirrors were cut 5 mm shorter than the specimens, allowing the mirrors to be situated within the hydraulic test frame itself to reduce the distance travelled by the reflections. Figure 52 shows several additional camera setups described in this Section.

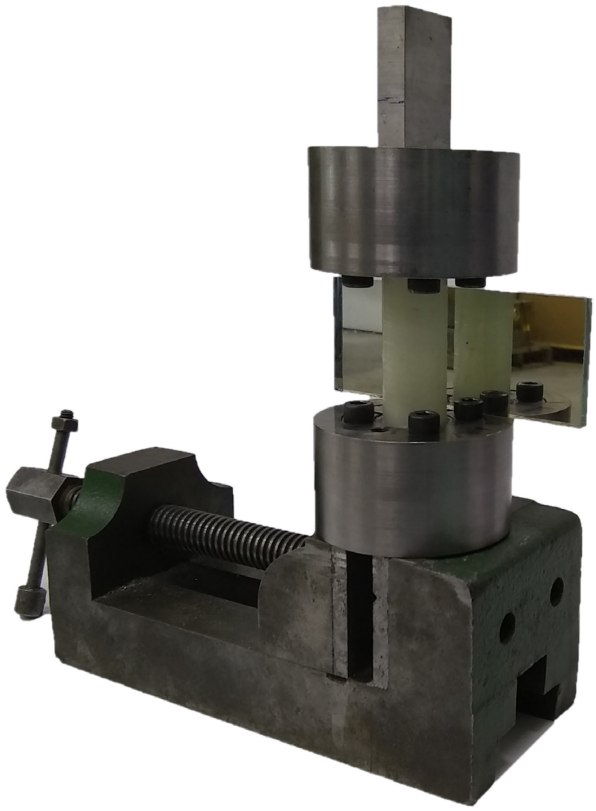

Figure 51. Small mirror inserted within the cup fixtures.

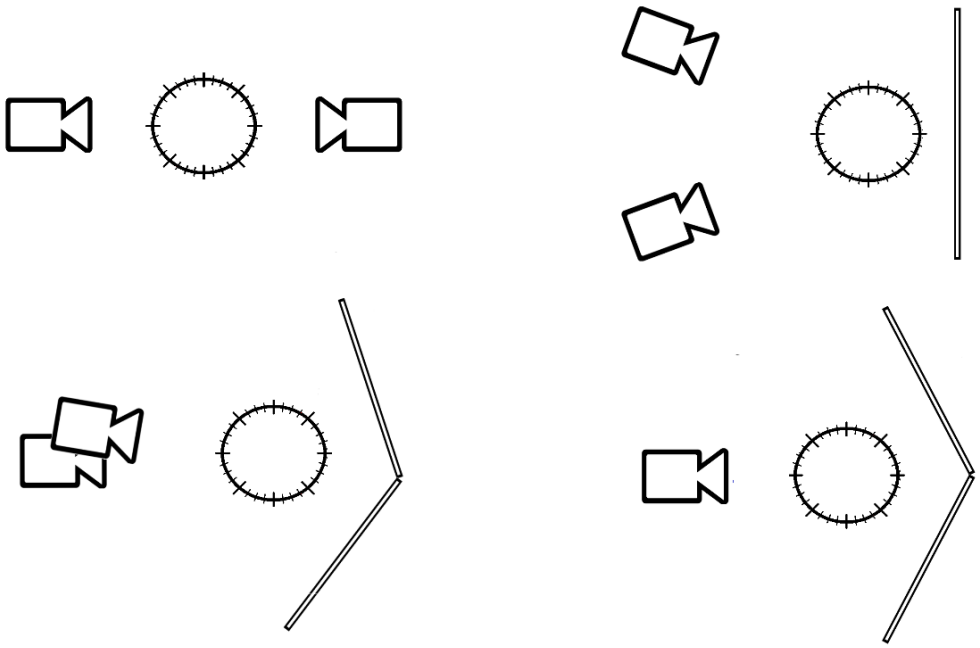

Figure 52. Schematic diagrams for camera arrangements 1, 3, 4 and 5 (clockwise from top left).

The third camera arrangement involved using two cameras and a small mirror within the hydraulic cross-heads, which would theoretically be close enough to the specimen to allow a single camera to observe both the front and the rear of one half of the specimen. However, the bolts from the locking assembly prevented the mirror from being close enough to the specimen to sufficiently reduce the reflection distance to make both the front and back clear. The locking assembly could be rotated 45°, but then the mirror was so close to the specimen that it obscured the rear completely. Any rotation between 0° and 45° would have the mirror not be symmetric for the two cameras. Using a much shorter mirror fit between the upper and lower locking assembly bolts was not an option, since crack initiation near the tab was very likely, and that area could not afford to go unobserved.

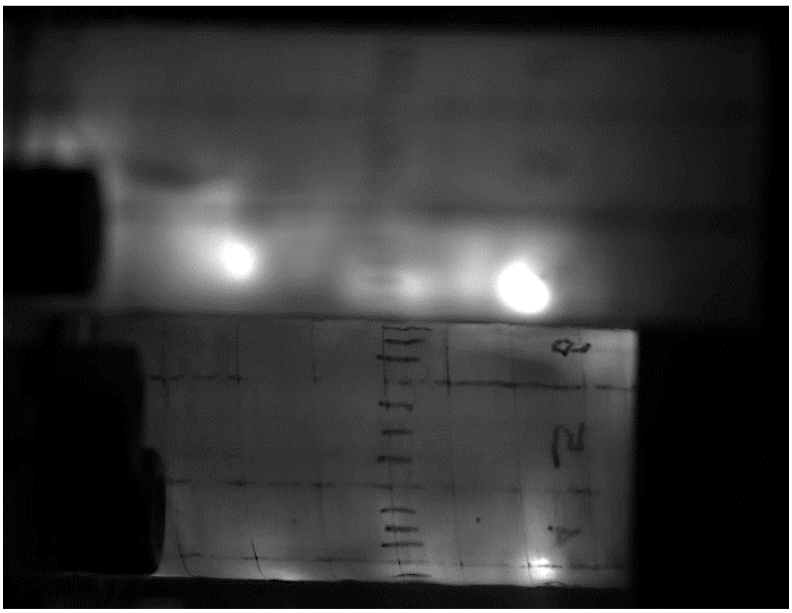

Figure 53. Image of the front and back of a tube from one camera in arrangement three.

The fourth camera arrangement involved using one camera and two mirrors. This allowed the entire specimen to be within the field of view, but the reflections were out of focus due to the added distance.

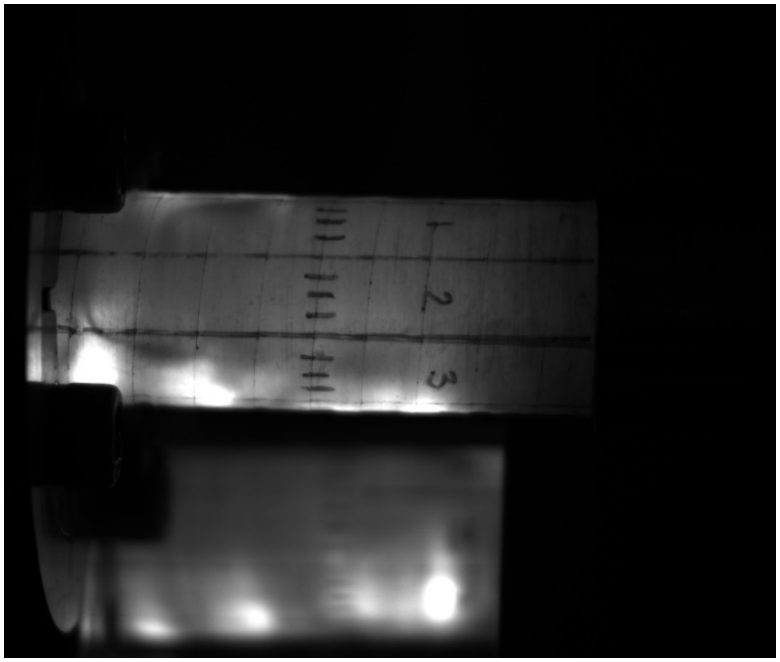

Figure 54. Image of the front and back of a tube from the camera using one of the two mirrors in arrangement four.

In the fifth arrangement, two offset cameras were used, with the offset camera being used to characterize the rear of the tube using the mirrors. This worked well, allowing a full 360° degree view of the specimen. However, positioning the mirrors and the camera capturing them was extremely difficult. Figure 55 shows that the entire specimen is visible between the two cameras. It should be noted that Figure 55 contains uncropped images; the mirrors and their camera had to be precisely position so that the entire specimen was within the field of view of the mirror camera, which in this case, it is by a fraction of a millimetre.

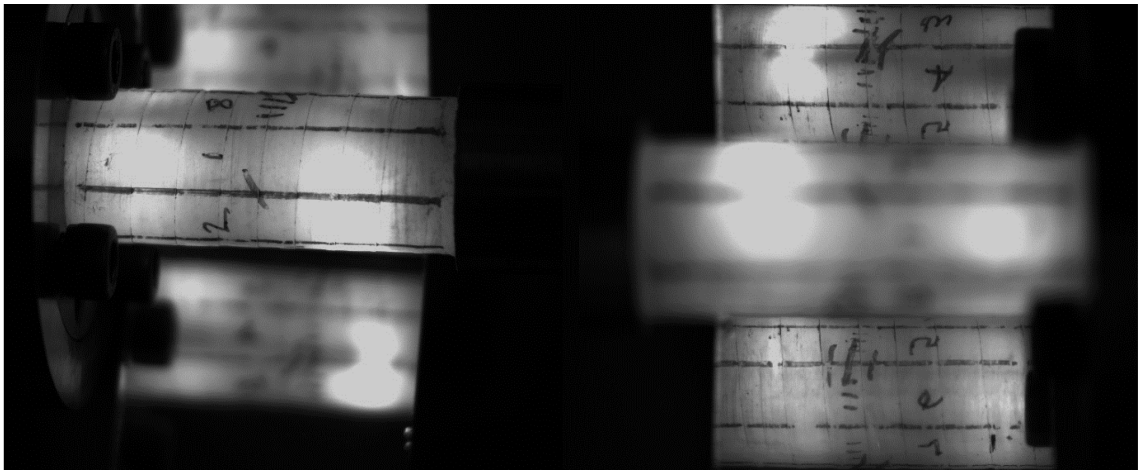

Figure 55. Image of the reference tube from both cameras in arrangement five, with full specimen visibility.

In both the combined quasistatic and combined cyclic tests, images of cracks were taken periodically over the duration. The frequency of image capture f_{img} varied with the applied peak loads, such that each between 100 and 1000 images were taken during each test. Assuming 500 images are taken per test, each image is taken after a 0.2% increment of the total tube lifetime, allowing a sufficiently granular assessment of the crack behaviour over the course of the test.

Both the test frames and the camera setup experienced delays between the time they are initiated and the time the cyclic loading and image capture begin. The test frames experience a delay due to force and displacement balancing steps, as well as the time required to ramp the load or torque up to the cyclic mean. Similarly, the camera software takes the first image after a delay corresponding to the desired capture frequency. If the test and the image capturing were started simultaneously, the two delays can be accounted for, and the time of any images can be matched to cycle numbers during the test.

5 Experimental Results

5.1 Quasistatic Characterization of Material Properties

The strengths and elastic properties of the plies were determined by the displacement-controlled quasistatic testing of five unidirectional specimen types: longitudinal tension, longitudinal compression, transverse tension, transverse compression, and in-plane shear. Quasistatic testing was divided into four rounds of testing after-the-fact, due to procedural changes that occurred throughout the process. Strain was measured by digital image correlation (DIC), and an anti-buckling fixture was used during longitudinal and transverse compressive tests. Table 20 shows the number of specimens tested in each test round, while Table 14 provides specimen dimensions, and the relevant ASTM references.

Table 20. List of specimens tested in four rounds of quasistatic testing.

Test Round	Longitudinal Tension (LT)	Transverse Tension (TT)	Longitudinal Compression (LC)	Transverse Compression (TC)	In-Plane Shear (IPS)
I	4x $[0_6]$	4x $[90_6]$			6x $[45_6]$
II			6x $[0_6]$	5x $[90_6]$	
III			7x $[0_{12}]$	7x $[90_{12}]$	
IV*	3x $[0_6]$	3x $[90_6]$		4x $[90_{12}]$	

*Additional shear specimens were not tested in Round IV, since Round I shear tests showed great consistency.

5.1.1 Round I Testing

Round I comprised the testing of tensile and shear properties of unidirectional coupons cut from panels UD-Thin1 and UD-Shear. Using the longitudinal tensile specimens, the ultimate longitudinal tensile strength F_{1T} was obtained from the failure loads and specimen geometries, while the elastic modulus E_1 and the major Poisson's ratio ν_{12} were obtained using DIC measurements of in-plane strain. Similarly, the ultimate

transverse tensile strength $F_{2T,}$ the elastic modulus E_2, and the minor Poisson's ratio ν_{21} were obtained from the transverse tensile specimens. Finally, the ultimate shear strength F_6 and the shear modulus G_{12} were obtained from the shear specimens (angled specimens loaded in tension), in the manner described in ASTM D3518. Table 21 contains the list of specimen measurements from Round I, and Figure 56, Figure 57 and Figure 58 show stress-strain data for the LT, TT, and IPS specimens respectively. Figure 59, Figure 60 and Figure 61 show the failure surfaces of several specimens loaded in longitudinal tension, transverse tension, and in-plane shear specifically (other specimens were sectioned for fibre volume fraction measurements).

Table 21. Round I specimen dimensions

Specimen	Width (mm)	Thickness (mm)
LT-1	20.04	1.80
LT-2	19.78	1.46
LT-3	19.83	1.44
LT-4	19.67	1.64
TT-1	25.33	1.72
TT-2	25.45	1.46
TT-3	25.37	1.52
TT-4	25.36	1.50
IPS-1	25.51	1.62
IPS-2	25.40	1.65
IPS-3	25.34	1.56
IPS-4	25.42	1.76
IPS-5	25.34	1.63
IPS-6	25.42	1.64

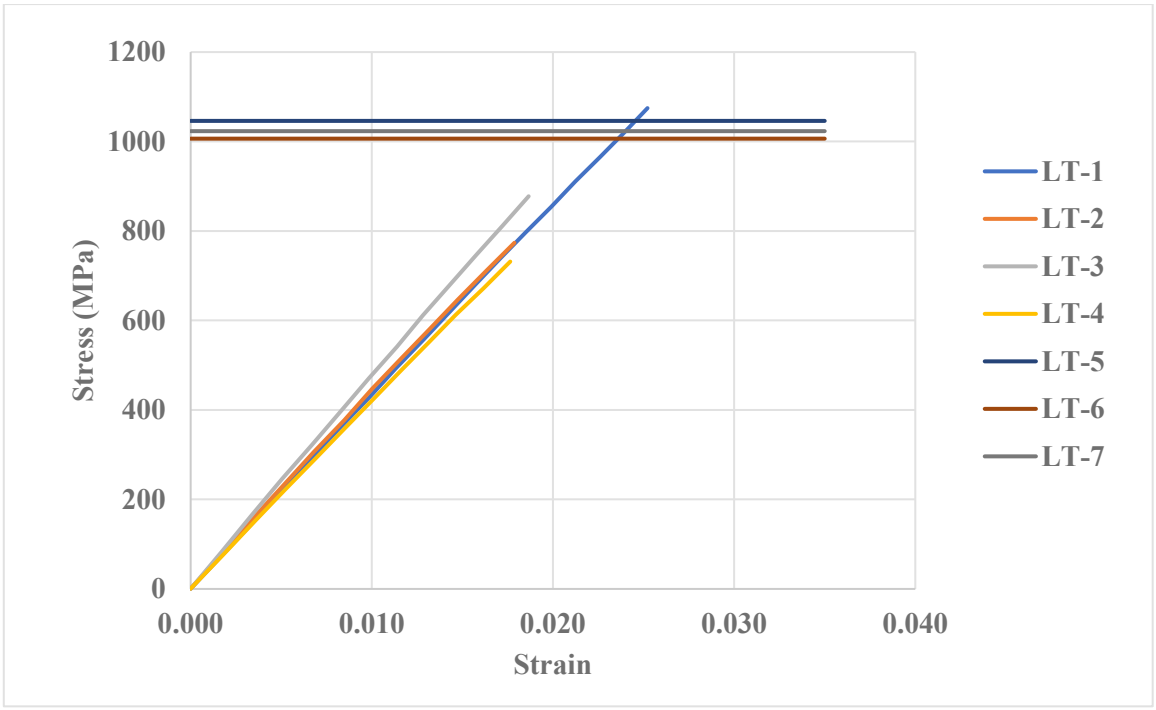

Figure 56. Stress-strain curves of longitudinal tensile tests.

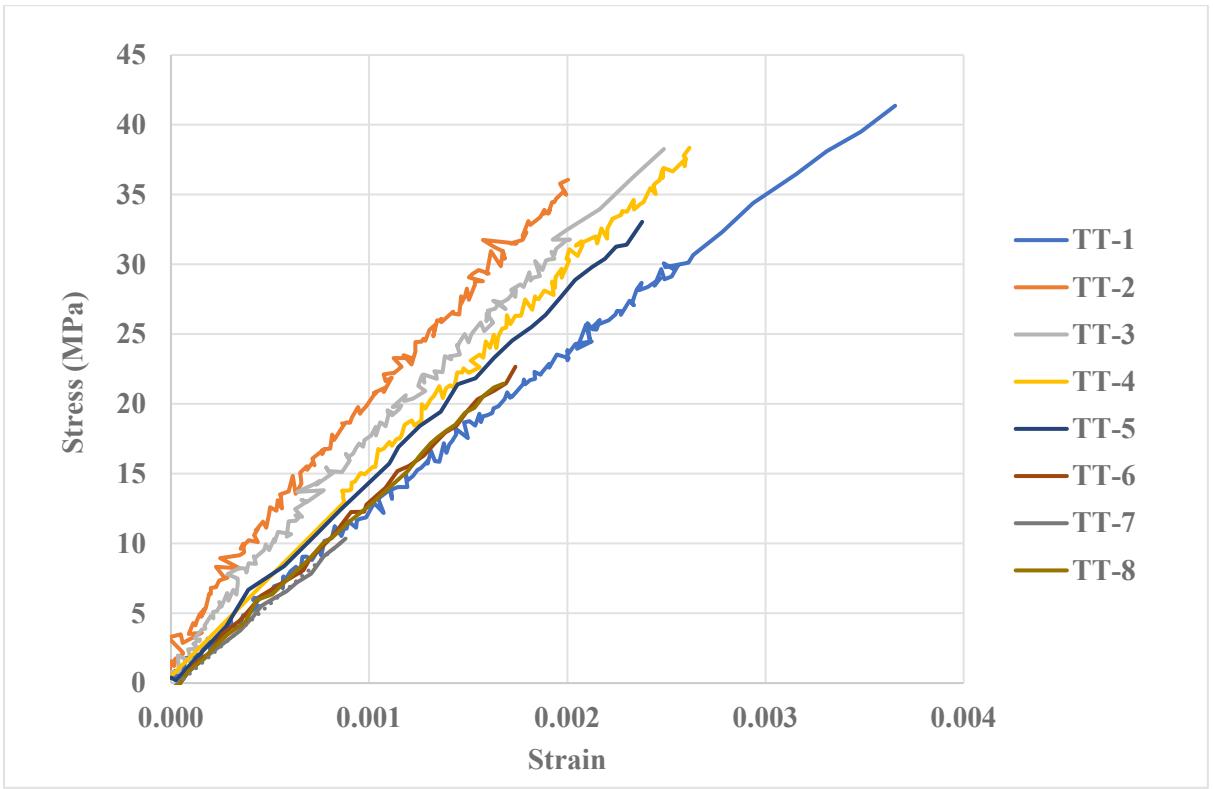

Figure 57. Stress-strain curves of transverse tensile tests.

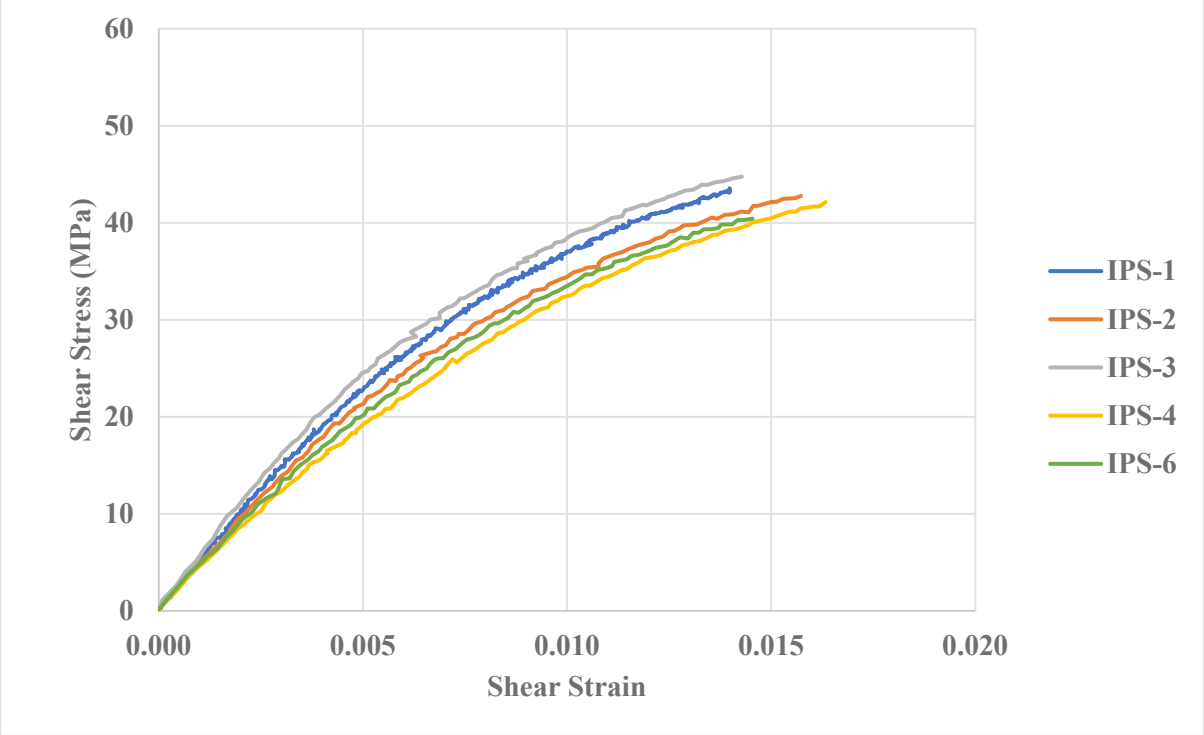

Figure 58. Stress-strain curves of in-plane-shear tests.

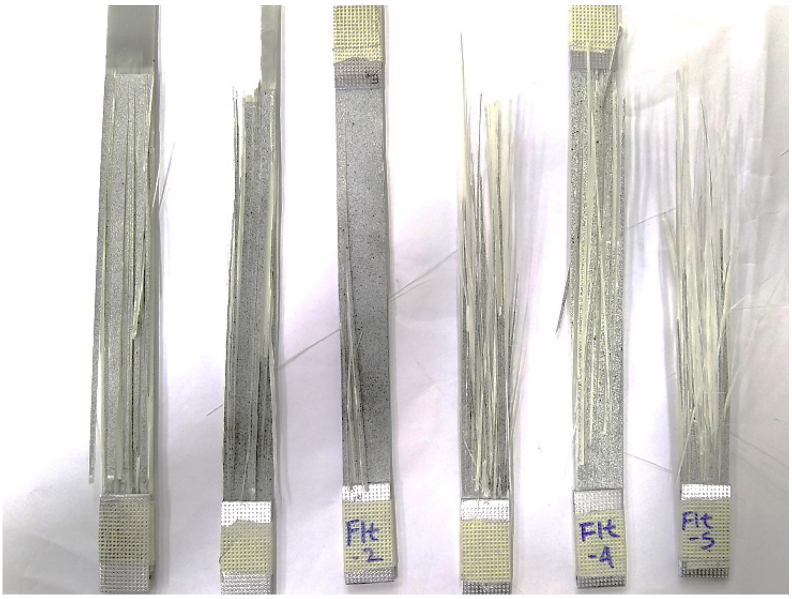

Figure 59. Failure surfaces of longitudinal tensile specimens.

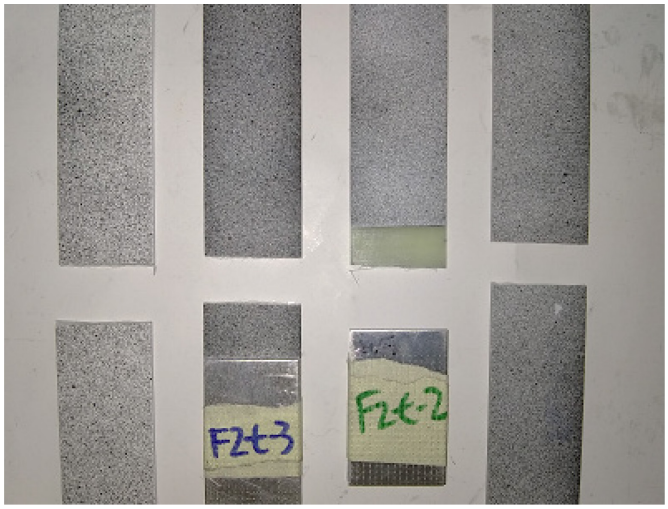

Figure 60. Failure surfaces of transvers tensile specimens.

Figure 61. Failure surfaces of in-plane shear specimens.

The failure mode of lamina in longitudinal tension produces a cloud of glass dust, a substantial safety hazard. Normally, a barrier of Saran wrap could be wound around the test frame cross-heads to prevent dust dispersion, however this prevents strain measurements using digital image correlation. Consequently, a barrier was placed partially surrounding the specimen without obscuring the camera, and glass particles were left to settle five minutes after each test. With a particulate mask and other personal protective equipment, the machine was wiped with a wet cloth after each test.

The first four specimens showed great consistency in their modulus measurements, so the latter three specimens were not strain mapped, being only tested for their ultimate strength, and are therefore only shown as strength values in Figure 56.

5.1.2 Round II Testing

Round II comprised the compressive testing of longitudinal and transverse coupons from panel UD-Thin1 to obtain their compressive strengths. While the modified Euler method was used to evaluate the theoretical buckling load of the compressive specimens based on the expected properties, both longitudinal and transverse specimens loaded in compression buckled before ultimate failure. Both longitudinal and transverse specimen types (measurements shown in Table 22) exhibited mode I buckling, though longitudinal specimens buckled between the grip ends, in contrast to the transverse specimens which buckled between the aluminum tabs, as shown in Figure 62. Buckling of unsupported transverse (top) and longitudinal (bottom) specimens.

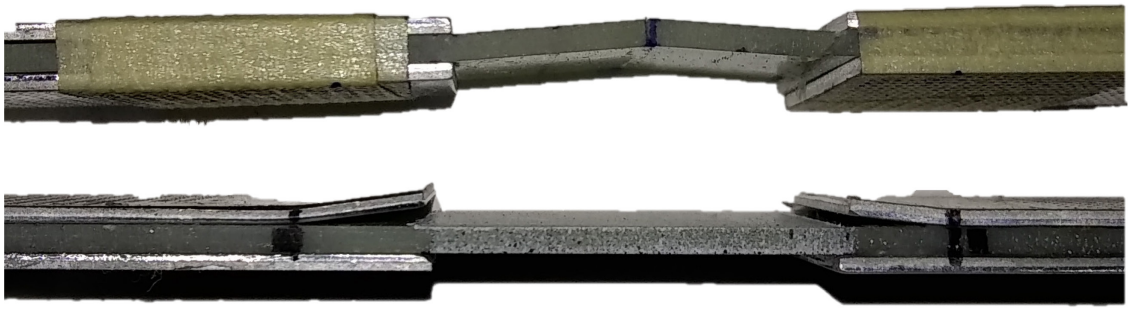

Figure 62. Buckling of unsupported transverse (top) and longitudinal (bottom) specimens.

Table 22. Round II specimen measurements.

Specimen	Width (mm)	Thickness (mm)
LC-1	25.39	1.48
LC-2	25.22	1.56
LC-3	25.31	1.57
LC-4	25.33	1.68
LC-5	25.24	1.54
LC-6	25.35	1.48
TC-1	25.35	1.44
TC-2	25.38	1.45
TC-3	25.36	1.64
TC-4	25.20	1.45
TC-5	25.40	1.72

5.1.3 Round III Testing

Round III comprised compressive tests on unidirectional coupons with twelve plies rather than six (cut from panel UD-Thick). Both longitudinal and transverse specimens still buckled, though not in mode 1 like their thinner counterparts. Figure 63 shows a schematic diagram of the *S-bending* observed in the thicker specimens, in comparison to the similar mode 2 buckling, while Figure 64 shows images of the specimens.

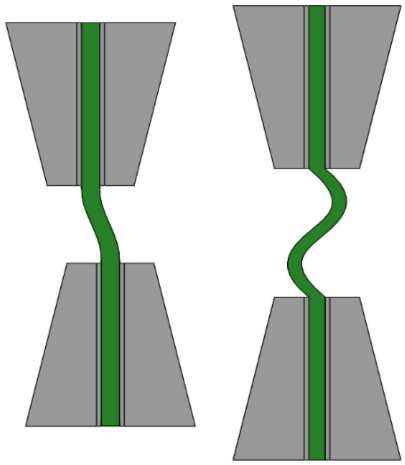

Figure 63. Schematic diagram of a specimen exhibiting standard mode 2 column buckling (left) and exhibiting S-bending observed during testing (right).

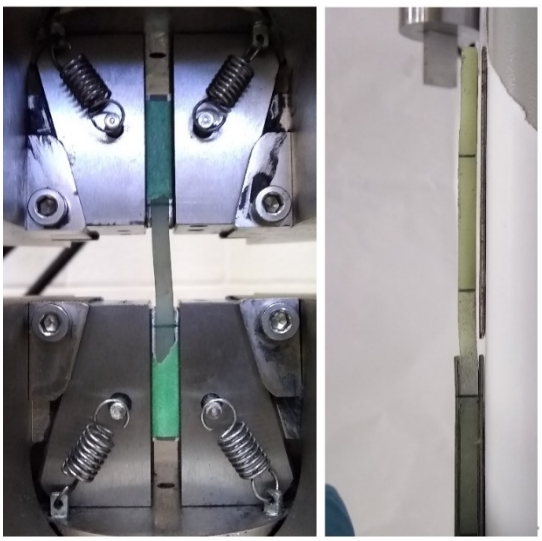

Figure 64. S-bending in multidirectional (left) and unidirectional transverse (right) specimens. The right image (rotated) shows a specimen held against a table with its original tab next to it.

Investigation of the S-bending phenomenon revealed several likely contributing factors. The first potential cause was the difference between the approximate and true properties of the material. Composite materials are far more susceptible to variation than homogenous materials due to changes in fibre misalignment, changes in ply thickness, and local defects. The effects of these changes can be significant, especially in compression, so the theoretical critical buckling load of the specimens could be much higher than the true value [14].

A second likely cause of the S-bending was a minute misalignment in the MTS and Instron crossheads during compression tests. This misalignment would likely greatly destabilize the specimen, and no alignment fixture was available to prevent this.

An anti-buckling fixture (shown in Section 4.3) was obtained to support the specimens laterally. However, this prevented strain mapping of the face using DIC. Specimens were speckled on their narrow widths, and it was assumed the strain measured from the specimen edge would provide the same values as those obtained from the face.

Table 23 shows the measurements of specimens prepared for Round III testing. Figure 65 and Figure 66 show the stress-strain curves of specimens in longitudinal and transverse compression, respectively. Specimens TC-5t-15, TC-6t-15, and TC-2t-10 were tested before strain measurement of the specimen edges was performed, and are therefore presented as straight lines on the stress axis. Additionally, many specimens buckled, failed in the tab region, or failed unexpectedly prior to the use of the anti-buckling fixture, reducing the number of curves presented. Figure 67 and Figure 68 show the failure surfaces of several specimens loaded in longitudinal compression and transverse tension, respectively (other specimens were sectioned for fibre volume fraction measurement).

Table 23. Round III specimen measurements.

Specimen	Width (mm)	Thickness (mm)
LC-1t-15	14.97	3.57
LC-2t-15	14.95	3.40
LC-3t-15	15.01	3.71
LC-4t-15	14.98	3.46
LC-5t-15	15.04	3.88
LC-6t-15	14.96	3.34
LC-1t-12	11.97	3.33
LC-2t-12	11.90	3.31
LC-1t-10	10.24	3.28
LC-2t-10	10.15	3.30
TC-1t-15	15.11	3.79
TC-2t-15	15.02	3.31
TC-3t-15	15.03	3.38
TC-4t-15	15.09	3.63
TC-5t-15	15.04	3.50
TC-6t-15	14.97	3.28
TC-1t-12	12.02	3.30
TC-2t-12	11.92	3.29
TC-1t-10	10.15	3.14
TC-2t-10	10.17	3.14

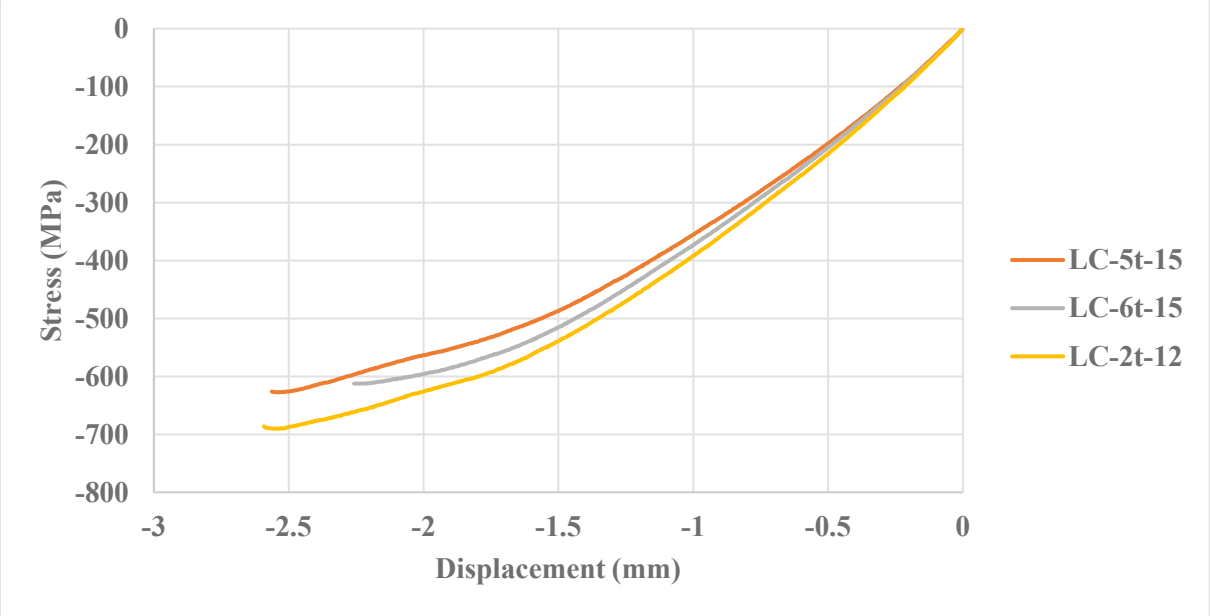

Figure 65. Stress-strain curves for longitudinal compressive tests.

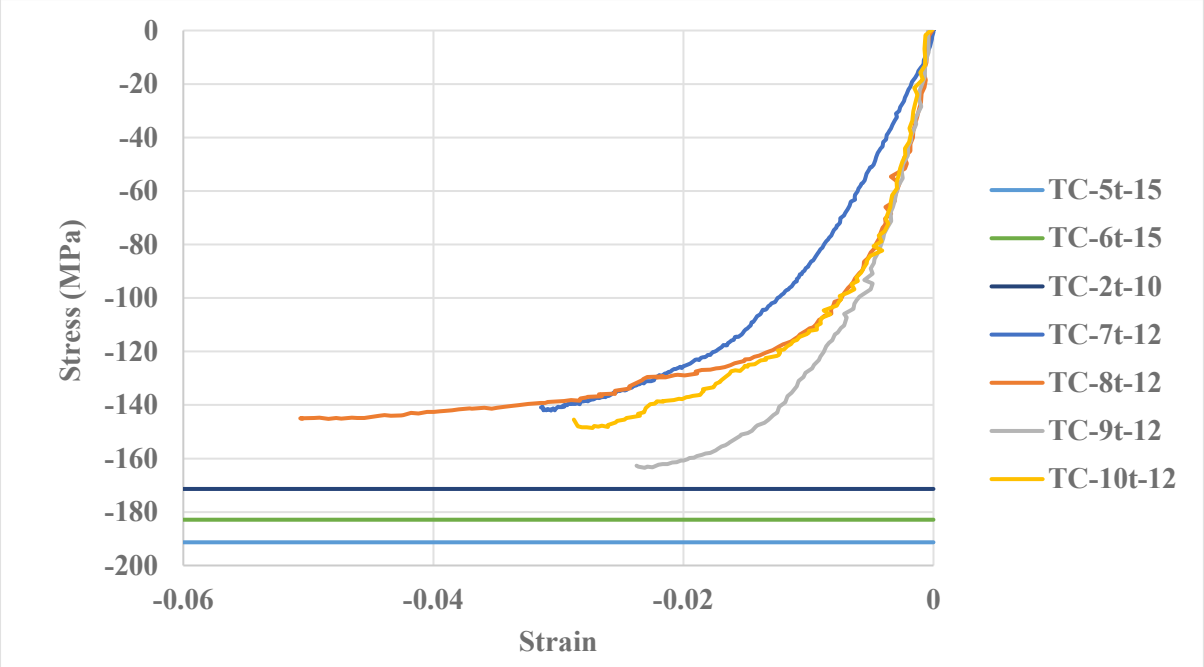

Figure 66. Stress-strain curves for transverse compressive tests (Rounds III and IV).

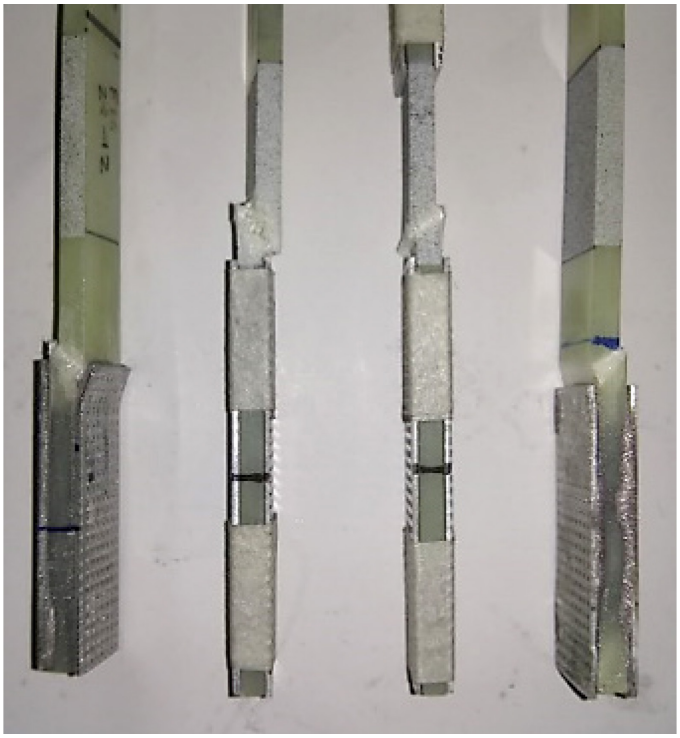

Figure 67. Failure surfaces of longitudinal compression specimens.

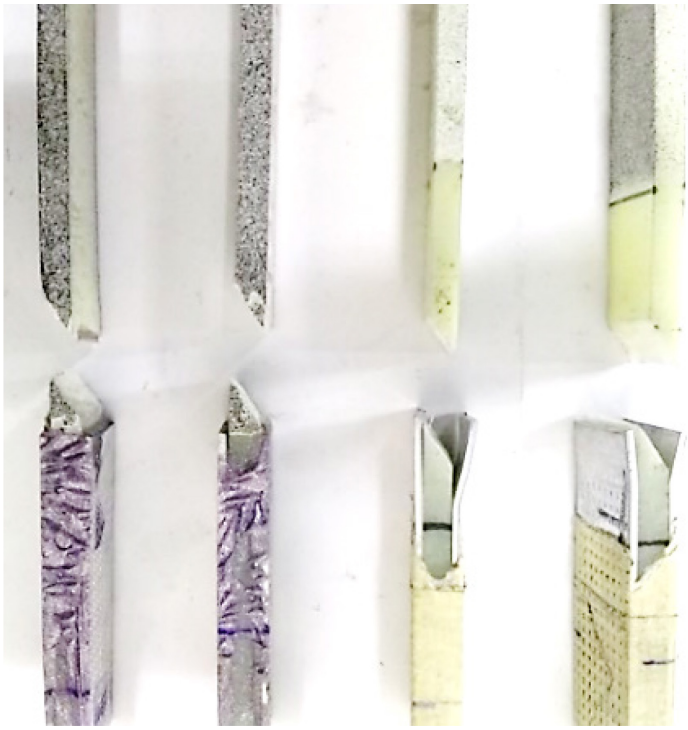

Figure 68. Failure surfaces of transverse compression specimens.

5.1.4 Round IV Testing

Round IV testing comprised several additional tests for each material property and strength (in-plane shear properties exhibited high repeatability). Tensile specimens in Round IV were cut from panel UD-Thin2, and compressive specimens were cut from UD-Thick. Specimens measurements are listed in Table 24.

Table 24. Round IV specimen measurements.

Specimen	Width (mm)	Thickness (mm)
LT-5	19.65	1.73
LT-6	14.95	1.80
LT-7	14.98	1.71
TT-5	25.22	1.56
TT-6	25.15	1.59
TT-7	25.22	1.73
TT-8	25.19	1.59
LC-7t-12	11.94	3.47
LC-8t-12	12.03	3.46
LC-9t-12	12.01	3.52
LC-10t-12	12.01	3.39
LC-11t-12	12.11	3.56
TC-7t-12	12.15	3.94
TC-8t-12	12.19	3.99
TC-9t-12	12.17	3.59
TC-10t-12	12.15	3.90
TC-11t-12	12.13	3.80

Combining the results of the Round IV tests with those from Round I and Round III revealed the approximate material properties and strengths of the unidirectional plies that could be used in classical laminate theory calculations. The values and strengths obtained are summarized in Table 25. Table 26 shows the nominal elastic constants and strengths of the woven fabric plies, which were not tested (obtained from Ref. [16]).

Table 25. Elastic properties and strengths of the unidirectional plies.

Elastic Constant	Value	Data Source
E_1	43.61 GPa	LT (Round I)
E_2	15.43 GPa	TT (Round I)
G_{12}	4.92 GPa	IPS (Round I)
ν_{12}	0.323	LT (Round I)
Strength		
F_{1T}	933.41 MPa	LT (Round I)
F_{2T}	54.58 MPa	TT (Round I)
F_{1C}	633.98 MPa	LC (Round III)
F_{2C}	163.58 MPa	TC (Round III)
F_6	42.63 MPa	IPS (Round I)

Table 26. Elastic properties and strengths of the woven fabric plies present in the tubes. Values were obtained from Ref. [18], not obtained experimentally.

Elastic Constant	Value
E_1	17.03 GPa
E_2	16.54 GPa
G_{12}	3.032 GPa
ν_{12}	0.159 GPa
Strength	
F_{1T}	257 MPa
F_{2T}	239 MPa
F_{1C}	Not provided
F_{2C}	Not provided
F_6	80 MPa

Based on typical modulus and Poisson's ratio value for glass fibres and the epoxy matrix (see Table 27), the rule of mixtures, and Halpin-Tsai equations were used to approximate the fibre volume fraction based on the obtained elastic constants of the quasistatic specimens. By minimizing the error between the theoretical and observed values of E_1, E_2, and G_{12}, the approximate fibre volume fraction of the specimens was calculated to be 59.6%. This volume fraction corroborates that obtained by thermogravimetric analysis (58%).

Table 27. Typical elastic constants of glass fibres (f) and the epoxy matrix (m).

Property	Value
E_f	72 GPa
E_m	4.2 GPa
ν_f	0.20
ν_m	0.34

A comparison with elastic properties and strengths of other E-glass/epoxy laminates suggested an unusually low shear strength value. ASTM D3518 dictates that a $[45/\text{-}45]n_S$ laminate be tested, though quasistatic shear specimens had a layup of $[45_6]$. The elastic behaviour, and therefore the ultimate shear strength and shear strain of the laminate may have been artificially lower due to the non-zero A_{16}, A_{26}, A_{61} and A_{62} in the extensional stiffness matrix. To determine the accuracy of the reported F_6 values, four tubular specimens were loaded quasistatically with increasing rotary displacement. The value of applied torque was recorded whenever an audible crack occurred within the specimen, indicating either crack initiation or propagation. Substantial ambient noise and quiet cracks made this method very subjective, warranting multiple measurements for each specimen; the last measurement represents a crack that undoubtedly corresponds with ply cracking, though failure *may* have occurred at lower torques. Using the established tube properties and geometry, the shear stress of the tubes' transverse plies at the recorded torques was determined using the equations in Section 3.1.3. The

results are shown in Table 28 and indicate that ply failure occurred at approximately 45 MPa (or earlier). While these results were subjective, they did demonstrate that the ultimate shear strength values obtained in Round I tests were not artificially low.

Table 28. Torsion values at which audible cracking is heard in tubular specimens. While not a precise measurement due to ambient noise, blue cells indicate torques at which obvious cracking occurred, constituting the upper bound on ultimate shear strength.

TubeShear1		TubeShear2		TubeShear3		TubeShear4	
Torque [N · m]	Stress [MPa]	Torque [N · m]	Stress [MPa]	Torque [N · m]	Stress [MPa]	Torque [N · m]	Stress [MPa]
12	27.5	22	50.4	20.5	47.0	10.3	23.6
14	32.1					12.7	29.1
17.5	40.2					14.9	34.2
20	45.9					19.5	44.7

In addition to the unexpectedly low ultimate shear stress, a large discrepancy was observed between the observed minor Poisson's ratio and the corresponding value predicted using the fibre volume fraction. For a typical unidirectional laminate, these values are related by Equation 5 which based on the observed values of E_1, E_2, and ν_{12}, would give a minor Poisson's ratio of 0.114. However, the value measured using digital image correlation on the transverse tensile specimens was 0.087. This suggests that the methods used to measure strain or evaluate Poisson's ratios were either not accurate, or not implemented correctly. The erratic major and minor strain measurements obtained from the transverse tensile specimens (shown in Figure 70 compared to Figure 69) suggest that the minor Poisson's ratio is more likely to be incorrect. However, the values of all properties in unidirectional GFRP laminates with a given fibre volume fraction vary greatly from publication to publication. Consequently, there was no basis for discarding any data obtained here in lieu of more universally agreed-upon values. Figure 71 and Figure 72 show the images of failure surface in static shear failure in tubes.

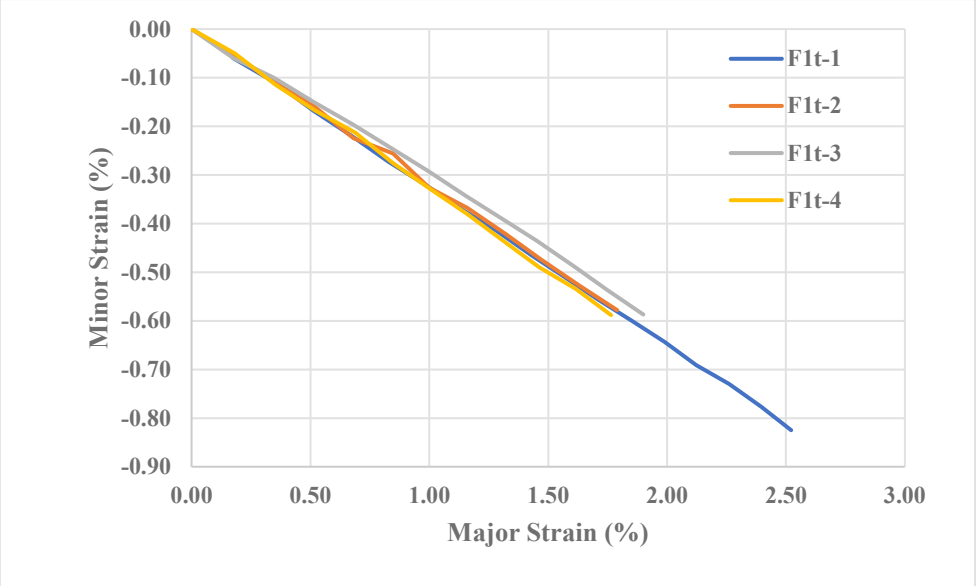

Figure 69. Strain and major Poisson's ratio measurements from LT specimens.

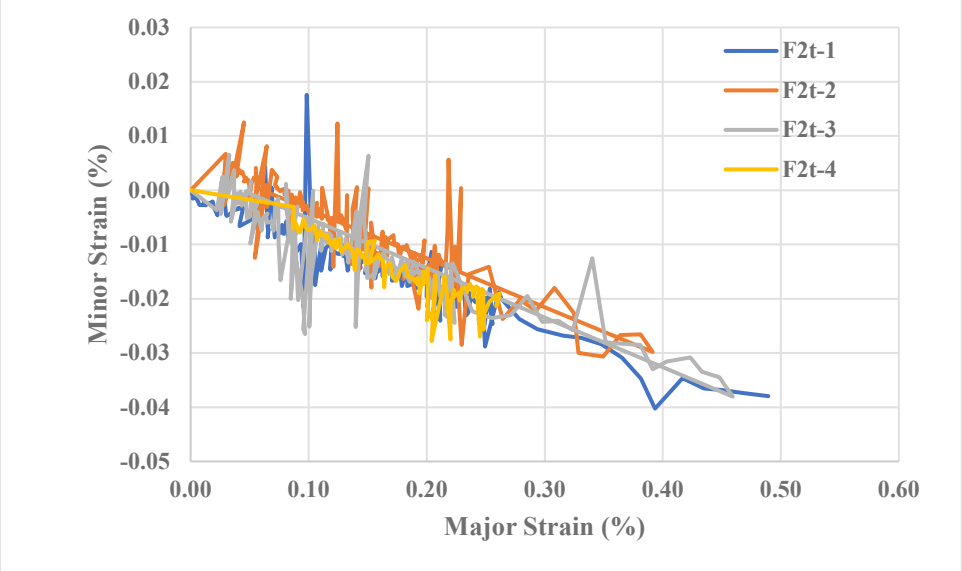

Figure 70. Strain and minor Poisson's ratio measurements from TT specimens.

Figure 71. Static shear failure surface in tubes.

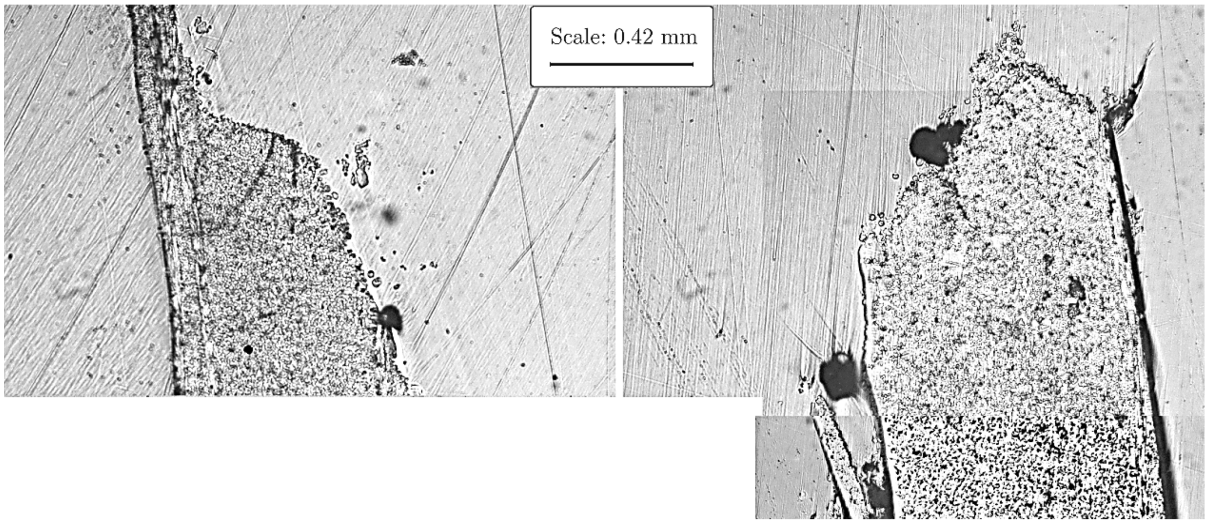

Figure 72. Static Shear failure surface in tubes (continued).

One additional test was run using a FLIR infrared camera to the monitor *in situ* cracking during a quasistatic compression test of a tube. Figure 73 shows frames from the final minute of the test in which heat is released from the specimen in the failure region due the cracking of the matrix. The results confirmed that transverse compressive damage is localized to a single area. Additionally, the results showed that the damage observed visually could also be characterized using thermography, allowing for similar investigations to be performed on opaque carbon-fibre composites.

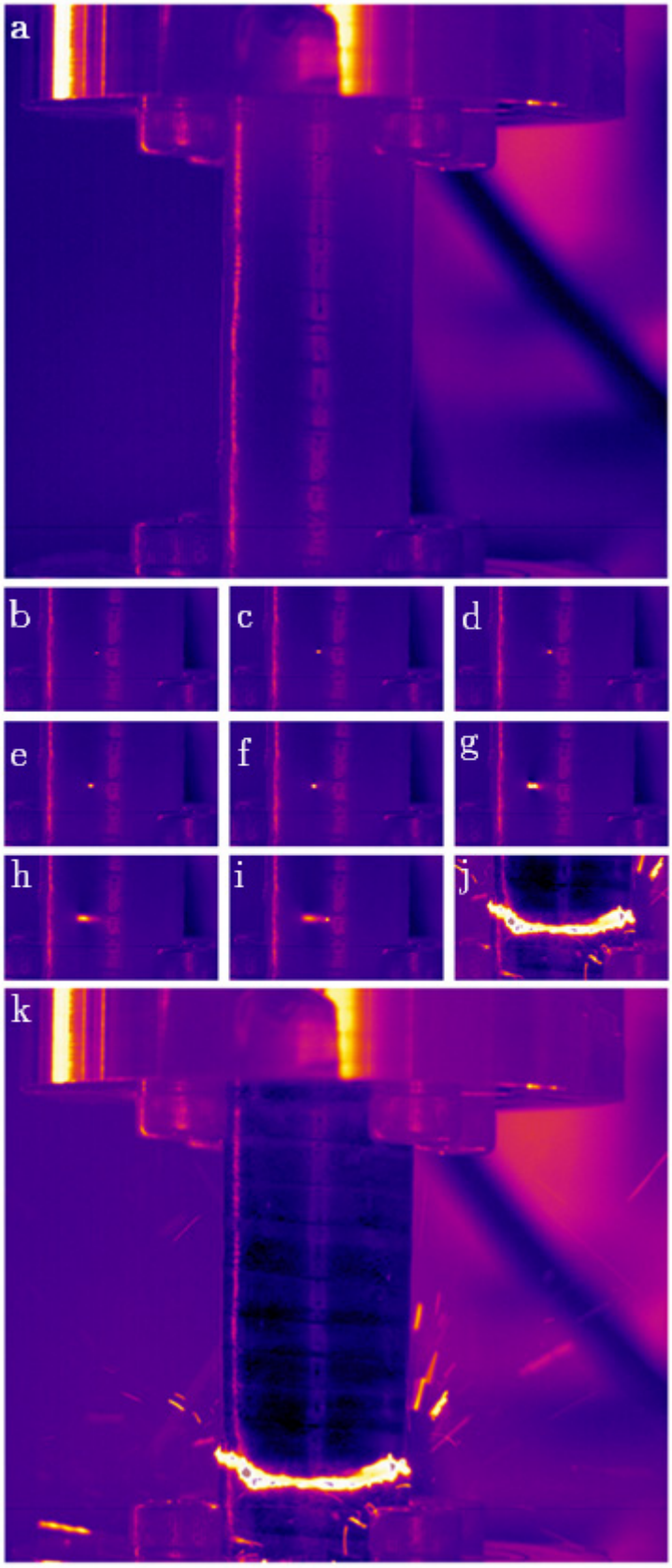

Figure 73. Thermal images of cracking under quasistatic static transverse compressive loading a) at the start of the test, b) during crack initiation, c)-i) during crack propagation, and j)-k) at ultimate failure.

5.2 Quasistatic Characterization of Multiaxial Stress States

5.2.1 Multiaxial Stress States in Coupons

The first set of multidirectional coupons tested where those cut from panel MD16-65 (layup $[0_2/65_2/0_2/-65_2]_S$). With the biaxiality ratios already designed into the laminate layup, multidirectional coupons were loaded quasistatically in displacement-controlled tests. During quasistatic compression loading, it was observed that the apparent *in situ* strengths of the plies were far greater than anticipated. The off-axis plies were predicted to fail at compressive loads of approximately -17 kN and -25 kN (inducing F_6 and F_{2C} respectively). However, the specimens tested withstood up -30 kN and -42 kN, when the 3M two-part epoxy used to bond the tabs failed. No evidence of cracking was apparent from *in situ* images, and examination of these specimens by optical microscopy did not reveal any cracks within the plies that may have occurred prior to tab adhesive failure.

To determine whether the correct biaxiality ratio was being produced within the off-axis plies, four MD16-65 specimens were loaded in quasistatic tension. The first off-axis crack initiations in the different specimens were observed within 10% of the theoretical transverse compressive failure load P_{2T}. Figure 74 shows the specimens loaded beyond the point of first-ply failure.

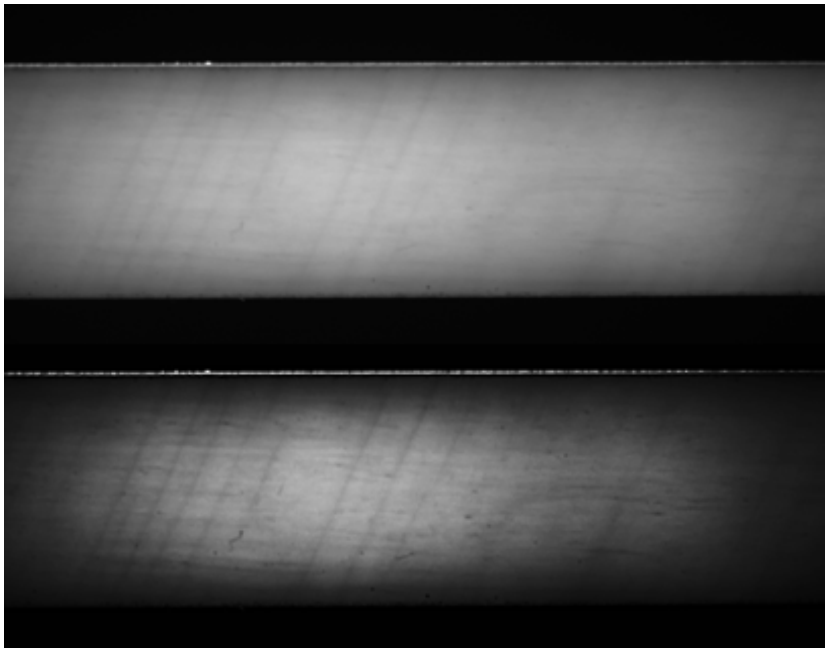

Figure 74. Unprocessed (top) and processed (bottom) images of ply cracking in an MD16-65 specimen loaded in quasistatic tension. Cracks generally occur sequentially, rather than simultaneously.

With the states of stress determined to be accurate, it was clear that the *in situ* strength of the plies was much greater than predicted. Because the loads required to induce ply cracking could theoretically exceed -42 kN, it was determined that the number of plies must be halved, since the use of an anti-buckling fixture was already anticipated. The new laminates, (layups $[0/65/0/-65]_S$ and $[0/75/0/-75]_S$), were not obtained in time for further testing.

5.2.2 Multiaxial Stress States in Tubes

Quasistatic tests on the tubes were load-controlled, rather than displacement-controlled, to ensure that the correct ratio of torque-to-load was applied to induce the desired biaxiality ratio. Due to the cylinder surface defects mentioned Chapter 4, only four specimens were used: two for $\lambda_{12} = 0.21$ and two for $\lambda_{12} = 0.40$. Figure 75 shows the presence of ply damage prior to specimen failure. Figure 78 through Figure 81 show the failure surfaces of the different specimens.

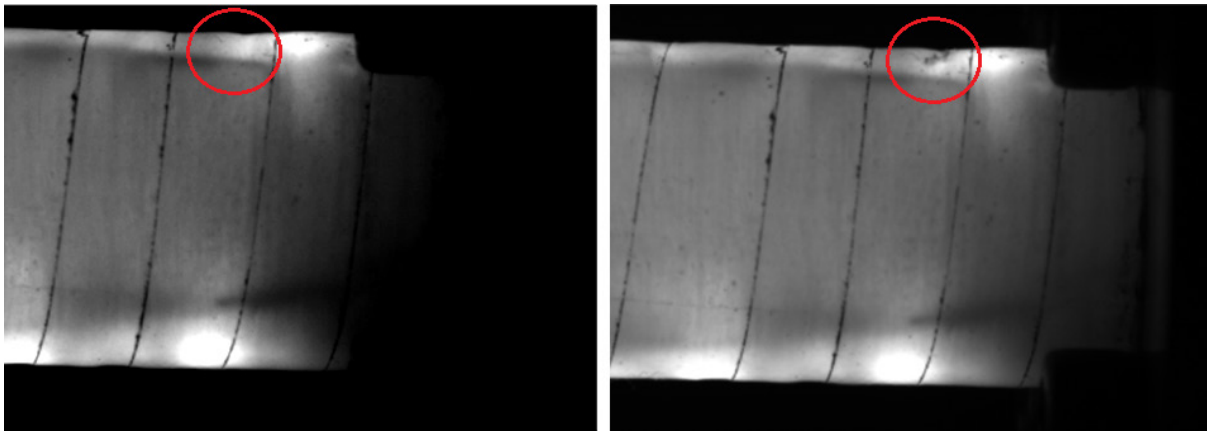

Figure 75. Presence of a combined quasistatic compressive-shear crack moments before rupture (right), and a comparison to the region at the start of the test (left).

Failure stresses were relatively consistent and in line with predicted values. QS04-1 showed a helical failure surface running along the surface defect made by the shrink tape during curing, suggesting defect-induced premature failure. Additionally, QS04-1 did not exhibit any minute dips its force-displacement or torque-rotation plots (Figure 76 and Figure 77, respectively)

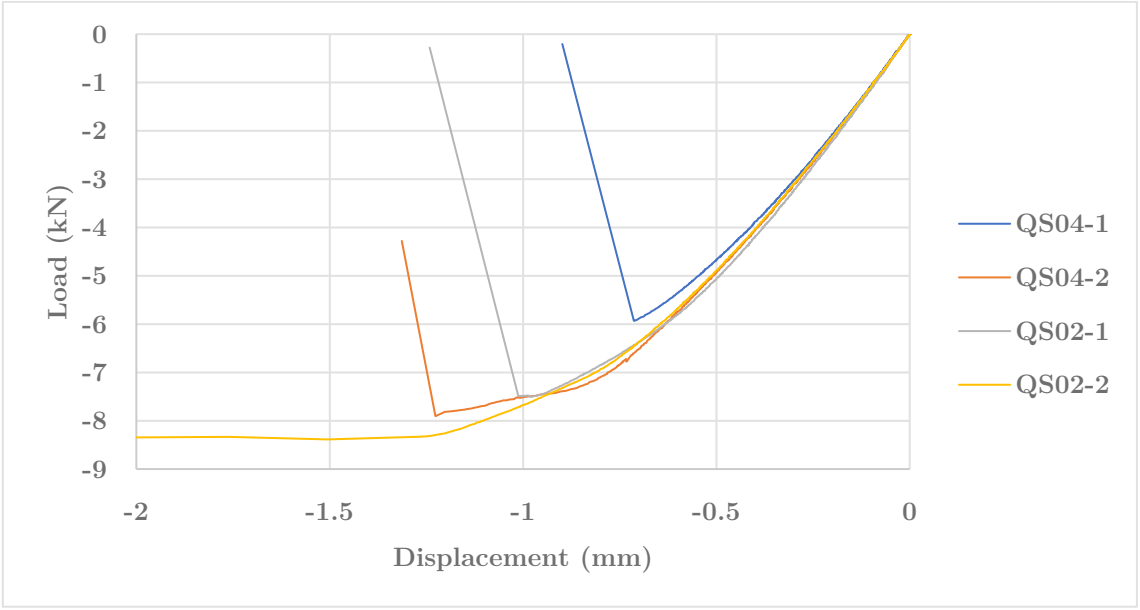

Figure 76. Load-displacement curves of tube specimens under combined quasistatic loading.

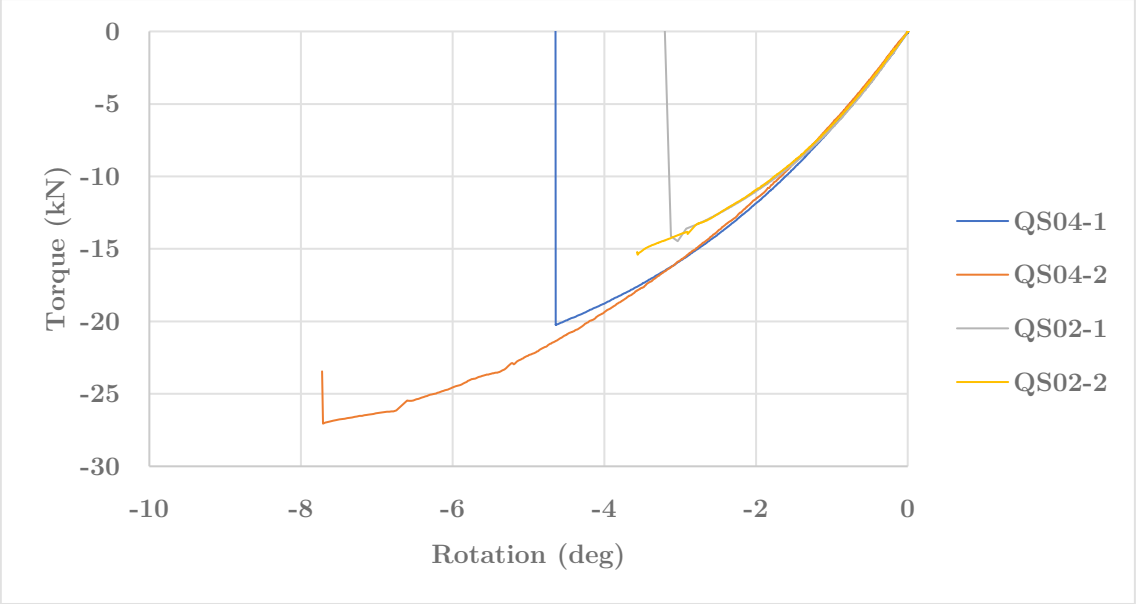

Figure 77. Torque-rotation curves of tube specimens under combined quasistatic loading.

Table 29. Loads, torques, and corresponding approximate stresses (based on nominal tube geometric) at dips observed in load-displacement and torque-rotary displacement graphs.

QS04-2					
Time	Load [N]	σ_2 [MPa]	Torque [N · m]	σ_6 [MPa]	λ_{12}
167.6630	-6.7783	-145.75	-22.9574	-58.39	0.400617
187.1390	-7.4939	-161.14	-25.4772	-64.80	0.402135
194.8260	-7.7900	-167.51	-26.8455	-68.28	0.407617
QS02-1					
Time	Load [N]	σ_2 [MPa]	Torque [N · m]	σ_6 [MPa]	λ_{12}
184.2110	-7.5067	-161.42	13.3300	-33.91	0.2101
QS02-2					
Time	Load [N]	σ_2 [MPa]	Torque [N · m]	σ_6 [MPa]	λ_{12}
186.7090	-7.4601	-160.41	-13.2866	-33.79	0.210648

Table 30. Loads, torques, and corresponding approximate stresses (based on nominal tube geometry) at the point of specimen rupture

	Failure Load [N]	Failure σ_2 [MPa]	Failure Torque [N · m]	Failure σ_6 [MPa]
QS04-1	-5934	-127.60	-20.24	-51.47
QS04-2	-7905	-169.98	-27.06	-68.81
QS02-1	-7507	-161.42	-13.47	-34.26
QS02-2	-8420	-181.06	-15.40	-39.18

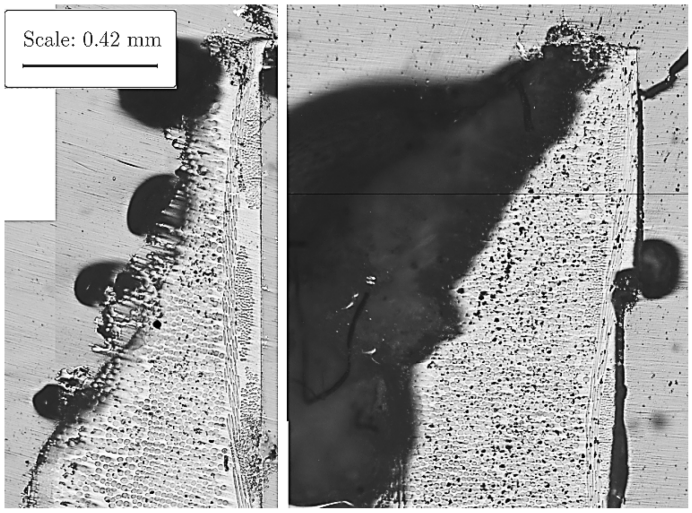

Figure 78. QS02-1 failure surfaces.

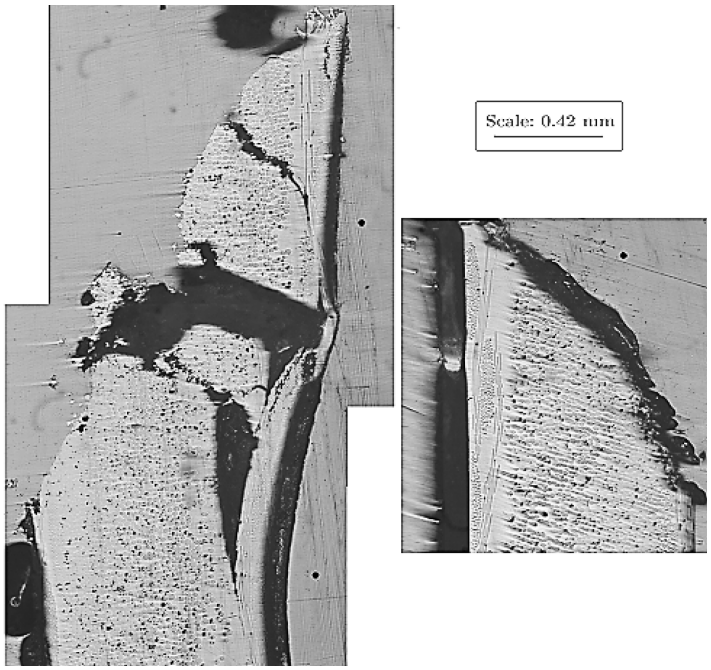

Figure 79. QS02-2 failure surfaces.

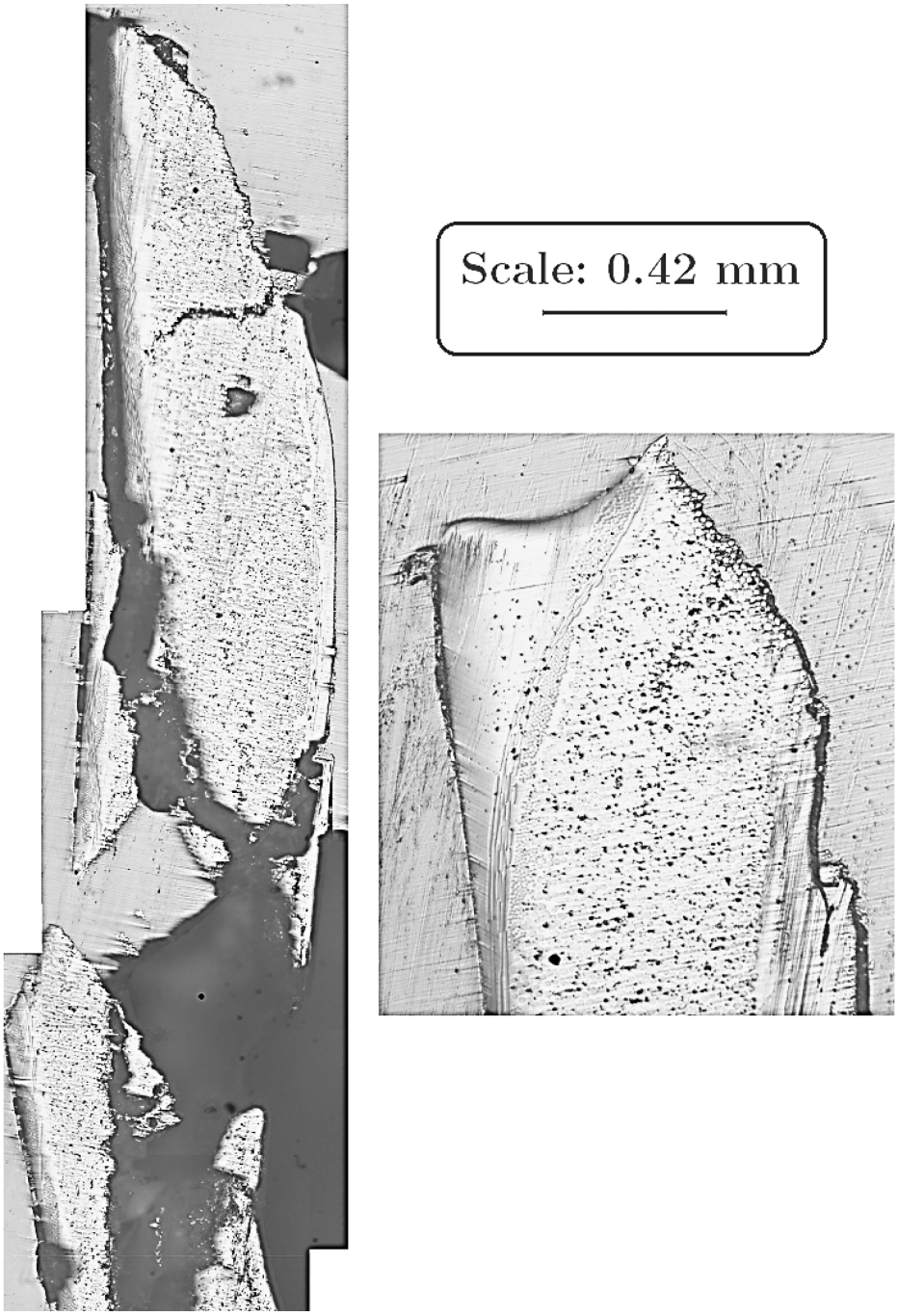

Figure 80. QS04-1 failure surfaces.

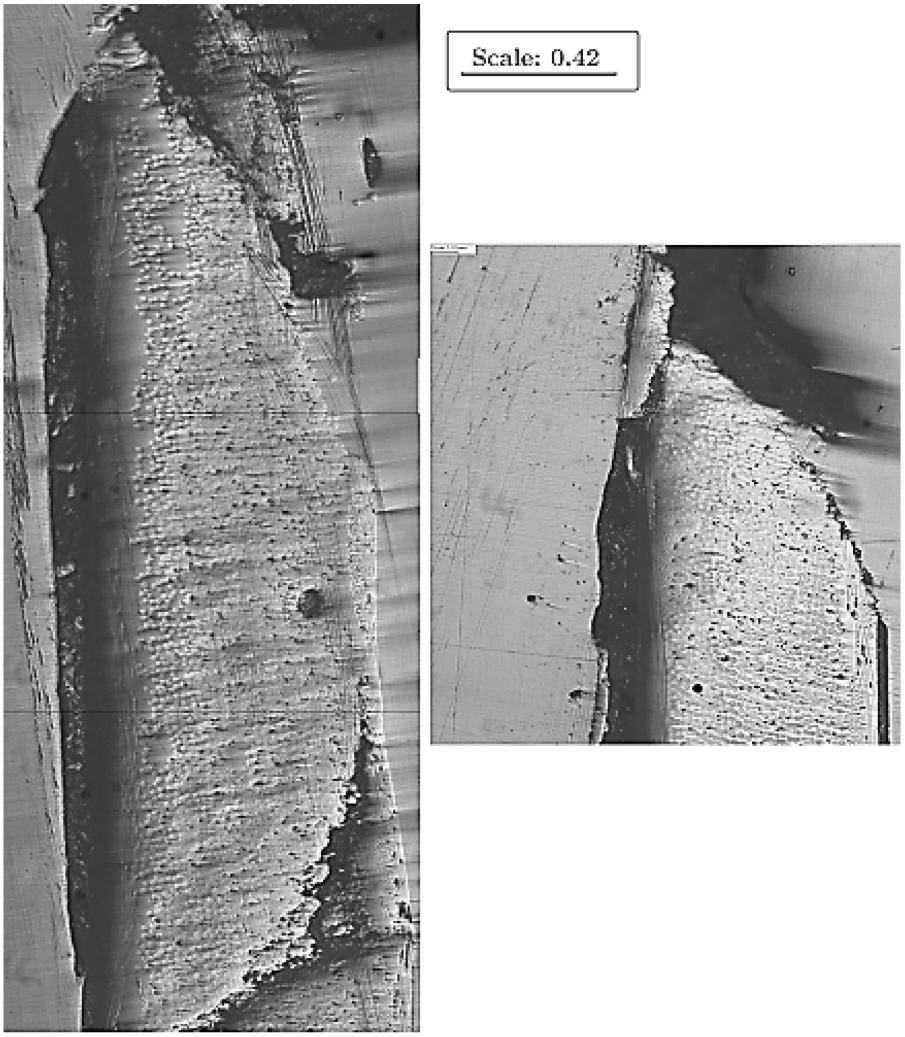

Figure 81. QS04-2 failure surface.

Based on the maximum stress failure criterion and the experimentally observed ply strengths, tubes subjected to $\lambda_{12} = 0.40$ were predicted to fail by transverse compression, while tubes subjected to $\lambda_{12} = 0.21$ were predicted to fail by shear. However, the tubes each exhibited an inclined fracture surface at an angle of $55° \pm 10°$ relative to the plane perpendicular to the loading direction. This fracture plane angle is characteristic of transverse compressive failure [79], and suggests that all four tubes failed in this mode, rather than the QS02 tubes failing by shear as was predicted. The apparently failure of all tubes by transverse compression suggests that the shear strength of the plies is greater than what was predicted, or that the maximum stress failure criterion does not accurate describe the behaviour of the ply under multiaxial stresses.

The increased *in situ* strength of plies is often reported in the literature, wherein the strength of a ply is observed to be greater when the ply is in a laminate compared to when the ply is not. The improved strength is conferred by the presence of adjacent plies, which can constrain transverse cracking and promote damage in different failure modes [62]. In the case of the tube specimens tested, the strengths transverse plies, could be reinforced by the internal and external woven fabric plies.

Another possible factor affecting the apparent transverse compressive failure of the tubes subject quasistatic multiaxial loading is the accuracy of the failure criterion. The maximum stress criterion was considered in this investigation, though more complex alternative failure criteria have been established in the literature for plies including the Tsai-Wu criterion [91], Hashin's criterion [92], and Puck's criterion [93] (as well as publications proposing modified versions of these). Puck's criterion incorporates the interaction between transverse stress and shear stresses on a ply and reports different failure modes dependant on the ratio of applied stresses. The criterion presents a failure envelope which is substantially enlarged in the compression-stress space compared to the tension-shear space (i.e. a reinforcing of the ply's shear strength when combined with transverse compression) and indicates that the failure mode within this *Mode C* region is an inclined fracture surface corresponding to what was observed in the four tubes (see Figure 82). However, the angle of the fracture planes observed in the specimens corresponds to nearly purely-transverse compressive influence on failure. Increasing contribution of shear stress to the failure of a ply typically corresponds to a fracture plane angle much closer to perpendicularity relative to the loading direction. Additional tests of tubular specimens are required to more precisely determine the cause of failure in the two multiaxial load cases.

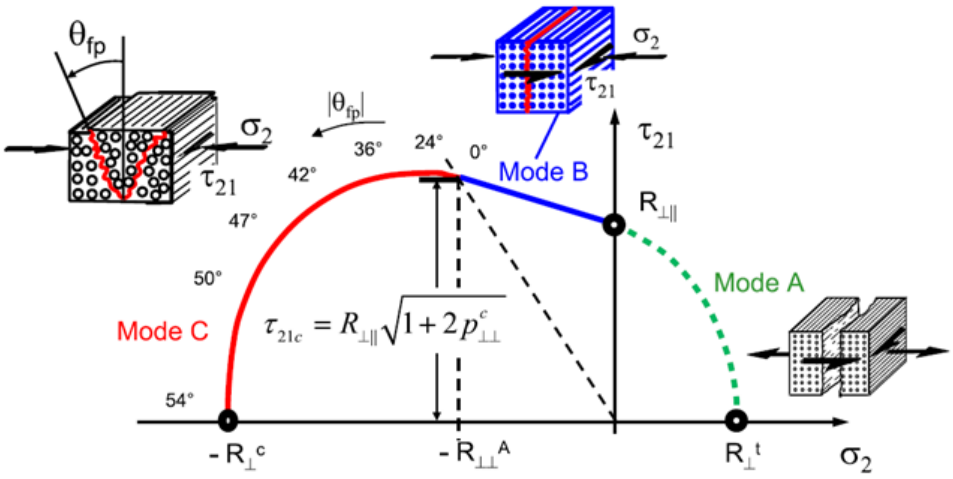

Figure 82. Puck's criterion failure envelope for a ply under combined transverse and shear stresses [94].

5.3 Cyclic Characterization of Multiaxial Stress States

In a series of load-controlled tests at nine predetermine states of stress (three biaxiality ratios, each at three transverse stress levels), coupons and tubes were cyclically loaded to determine the crack initiation lifetime of their constituent plies, and the behaviour of the specimens as they experience increasing sub-critical damage. Tests were purely compressive sinusoidal loading, with an R ratio of 20. The frequency of loading f_{load} was 10 Hz, though several tests used for troubleshooting tab failure were performed at 5 Hz.

The specimens tested under each biaxiality ratio (0.40, 0.21, and 0.00) were loaded to minimum compressive stresses equal to 80%, 70%, and 60% of the ply F_{2C}. The first test at 60% transverse compressive stress under $\lambda_{12} = 0.21$ led to specimen runout. As a result, specimens tested under $\lambda_{12} = 0.21$ and $\lambda_{12} = 0.00$ were tested at 80%, 75% and 70% of the F_{2C}.

Initially, it was planned that coupons and tubes would be each be tested at all three biaxiality ratios. However, the number of tests and the types of tests that could be run were reduced due to poor tube quality, tab adhesive failure in the tubes, and the unexpectedly high *in situ* transverse compressive strength of the multidirectional coupons. These complications meant that the $\lambda_{12} = 0.00$ tests were only run using unidirectional transverse coupons, and $\lambda_{12} = 0.21$ and $\lambda_{12} = 0.40$ tests were only run on tubes. Due to time constraints, thinner multidirectional coupons requiring lower failure loads were not obtained or tested.

Table 31. Specimens tested in each load-controlled test set.

Biaxiality Ratio	No. of Specimens	Specimen Shape	Specimen Layup	Nominal Dimensions (Length x Thickness)
$\lambda_{12} = 0.00$	12	Coupon	$[90_{12}]$	137 mm x 3.5 mm
$\lambda_{12} = 0.21$	16	Tube	$[0_F/90]_S$	100 mm x 0.73 mm
$\lambda_{12} = 0.40$	19	Tube	$[0_F/90]_S$	100 mm x 0.73 mm

Due to these various experimental limitations, fatigue tests on the tubes were grouped into test rounds, like the quasistatic tests on the unidirectional specimens. Round I tests comprised the testing of one tube at each stress level under the two non-zero biaxiality ratios. After the tube defects had been determined to be primarily on the outer surface and not the transverse plies, additional specimens were cut, prepared and tested in Round II and Round III.

Approximately half of Round II tests failed due to the adhesive layer debonding from the shell tab during cyclic loading. Part-way through the testing of additional tubes, many of the tests failed when the adhesive layer bonded to the tube separated from the shell tab. In three tests, the bolts on the locking assemblies were tightened by an additional 2.3 Newton-metres (20 inch pounds), from 10.7 to 13. In all three tests, specimens exhibited lifetimes lower than the lifetimes of other specimens under the same load states by 10 to 100 times. With the limited number of specimens available, this was considered sufficient evidence to stay at the established torque of 10.7 $\mathrm{N} \cdot \mathrm{m}$.

Specimens in Round III tests were loaded at a frequency of 5 Hz. The tests performed at 5 Hz did not indicate any obvious sensitivity of the crack initiation time to the loading frequency.

5.3.1 S-N Curves

S-N curves were produced to report the failure lifetimes of plies within a specific coupons or tubes, rather than the lifetime of the specimen before catastrophic failure. In six of the tube tests, crack initiation and final specimen rupture occurred just above the tabbed regions. As a result, the exact location and time of crack initiation could not be identified, since the angle of the cameras or the presence of the locking assembly screws obscured the view of the failure locus.

Table 32 shows average measurements of the unidirectional transverse coupons tested. Measurements of the tube transverse plies could not be determined prior to testing. The closest measurement to a true ply thickness value of the tube transverse plies could be determined by polishing the tube at the point of failure and examining it under a microscope, though this could not be done due to limited time.

Table 32. Measurements of unidirectional transverse coupons for $\lambda_{12} = 0.00$ tests.

Coupon ID	Width [mm]	Thickness [mm]
lam00_1	15.02	3.17
lam00_2	14.97	3.14
lam00_3	14.99	3.22
lam00_4	15.00	3.73
lam00_5	15.00	3.25
lam00_6	15.00	3.60
lam00_7	15.00	3.82
lam00_8	15.06	3.86
lam00_9	15.00	3.50
lam00_10	15.04	3.36
lam00_11	15.05	3.72
lam00_12	15.05	3.75

Figure 83 and Figure 84 show images of a tube and a unidirectional transverse coupon at the start of the test, at a time shortly before rupture, and after rupture has occurred.

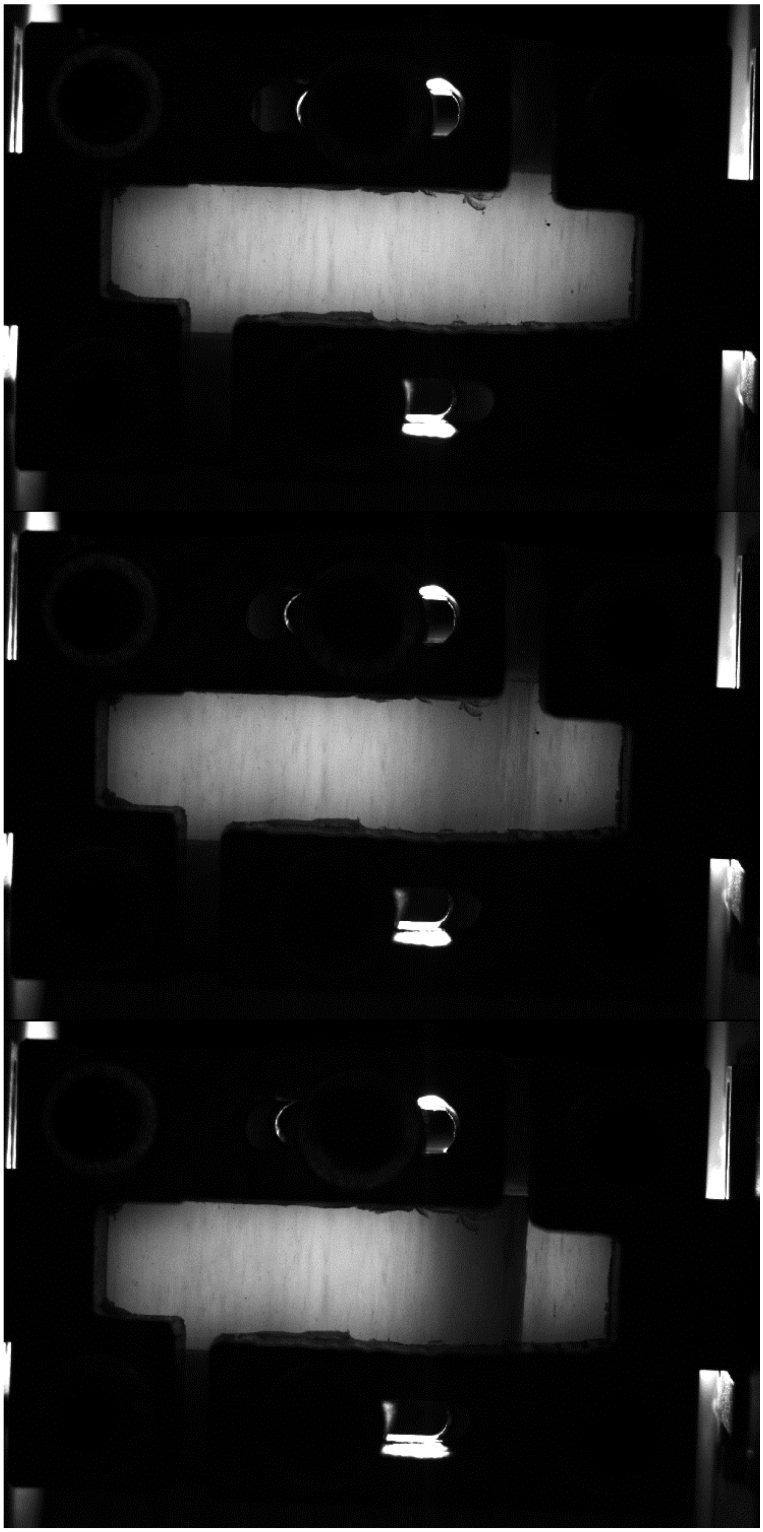

Figure 83. Camera images of a unidirectional transverse specimen at start of a test (top), prior to rupture (middle), and after rupture (bottom).

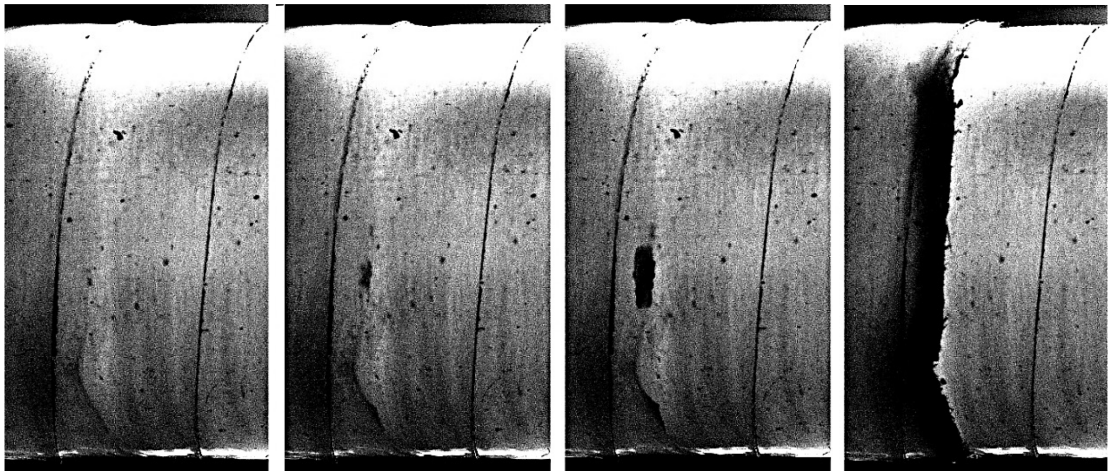

Figure 84. Camera images of a tube (lam021_F2c70_1) over its lifetime. Images have been post-processed to improve crack visibility.

Table 33, Table 34, and Table 35 show the test parameters for each test, the crack initiation lifetime N_C and the lifetime of specimen rupture N_R. The propagation lifetime of the crack N_P is the fraction of the specimen lifetime between the time of crack initiation and the time of ultimate specimen failure (rupture). Black cells in these tables indicate data not obtained due to test failure or out-of-view crack initiation.

Table 33. S-N setup and lifetime data for tubular specimens under $\lambda_{12} = 0.40$.

Tube ID	Test ID	Tab Torque [N · m]	Test Round	f_{load} [Hz]	$\frac{\sigma_{2,min}}{F_{2C}}$	N_C	N_R	N_P
11-1	lam040_F2c80_1	10.7	I	10	0.80	103	769	0.87
19-X1	lam040_F2c80_2	10.7	II	10	0.80	43	237	0.82
12-X1	lam040_F2c80_3	10.7	III	5	0.80	551	626	0.12
8-3	lam040_F2c70_1	10.7	I	10	0.70	2633	3243	0.19
18-X3	lam040_F2c70_2	10.7	II	10	0.70			
11-X1	lam040_F2c70_3	13	II	10	0.70	2713	2895	0.06
20-X4	lam040_F2c70_4	10.7	III	5	0.70	211	337	0.37
9-2	lam040_F2c60_1	10.7	I	10	0.60		256303	
18-X2	lam040_F2c60_2	10.7	I	10	0.60		81977	
17-X1	lam040_F2c60_3	10.7	II	10	0.60			
20-X1	lam040_F2c60_4	10.7	II	10	0.60		31168	
19-X3	lam040_F2c60_5	10.7	II	10	0.60		583	
18-X5	lam040_F2c60_6	10.7	II	10	0.60			
10-X2	lam040_F2c60_7	10.7	III	5	0.60	108923	381954	0.71
18-X6	lam040_F2c60_8	10.7	III	10	0.60	38923	751086	0.95
20-X5	lam040_F2c60_9	10.7	III	5	0.60			

Table 34. S-N setup and lifetime data for tubes under cyclic $\lambda_{12} = 0.21$ loading.

Tube ID	Test ID	Tab Torque [N · m]	Test Round	f_{load} [Hz]	$\frac{\sigma_{2,min}}{F_{2C}}$	N_C	N_R	N_P
9-X1	lam021_F2c80_1	10.7	I	10	0.80	4022	4728	0.15
10-X1	lam021_F2c80_2	10.7	II	10	0.80			
17-X4	lam021_F2c80_3	13	II	10	0.80	280	545	0.49
16-X2	lam021_F2c80_4	13	III	5	0.80	2	8	0.75
16-X3	lam021_F2c80_5	10.7	III	5	0.80		1560	
8-X1	lam021_F2c75_1	10.7	I	10	0.75	25423	45013	0.44
17-X3	lam021_F2c75_2	10.7	II	10	0.75	2422	5959	0.59
12-X2	lam021_F2c75_3	10.7	III	5	0.75			
12-X3	lam021_F2c75_4	10.7	III	5	0.75			
8-1	lam021_F2c70_1	10.7	I	10	0.70	10923	57149	0.81
17-X2	lam021_F2c70_2	10.7	II	10	0.70		117385	
18-X4	lam021_F2c70_3	10.7	II	10	0.70			
15-X1	lam021_F2c70_4	10.7	II	10	0.70			
19-X2	lam021_F2c70_5	10.7	II	10	0.70	7422	7484	0.01
16-X1	lam021_F2c70_6	10.7	III	5	0.70	2961	20089	0.85
18-X1	lam021_F2c60_1	10.7	I	10	0.60			

Table 35. S-N setup and lifetime data for coupons under cyclic $\lambda_{12} = 0.00$ loading.

Coupon ID	Test ID	f_{load} [Hz]	$\frac{\sigma^A_{2,min}}{F^A_{2C}}$	N_C	N_R	N_P
lam00_1	lam000_F2c80_1	10	0.80	5834	5940	0.02
lam00_4	lam000_F2c80_2	10	0.80	966	1074	0.10
lam00_6	lam000_F2c80_3	10	0.80	617	693	0.11
lam00_11	lam000_F2c80_4	10	0.80	750	854	0.12
lam00_2	lam000_F2c75_1	10	0.75	5327	7096	0.25
lam00_5	lam000_F2c75_2	10	0.75	2989	3442	0.13
lam00_7	lam000_F2c75_3	10	0.75	1227	1369	0.10
lam00_3	lam000_F2c70_1	10	0.70	191927	291491	0.34
lam00_8	lam000_F2c70_2	10	0.70	1928	2243	0.14
lam00_9	lam000_F2c70_3	10	0.70	11927	14623	0.18
lam00_10	lam000_F2c70_4	10	0.70	19927	23699	0.16
lam00_12	lam000_F2c70_5	10	0.70	4227	4934	0.14

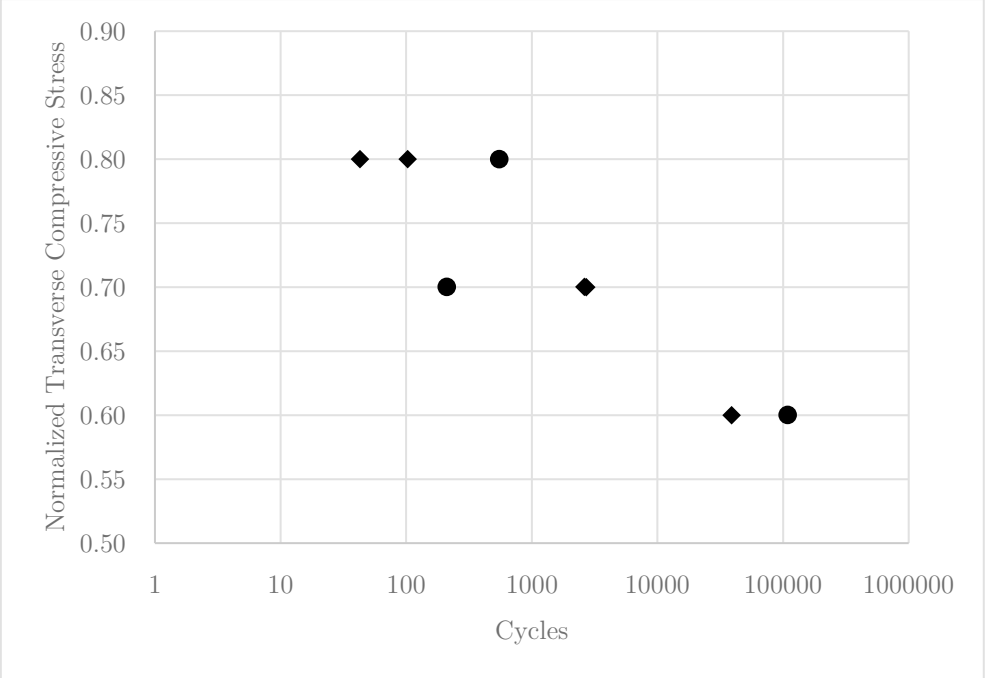

Figure 85. S-N data for lam $\lambda_{12} = 0.40$ (tubes). Diamond markers represent data points obtained at 10 Hz, while circle markers represent data points obtained at 5 Hz.

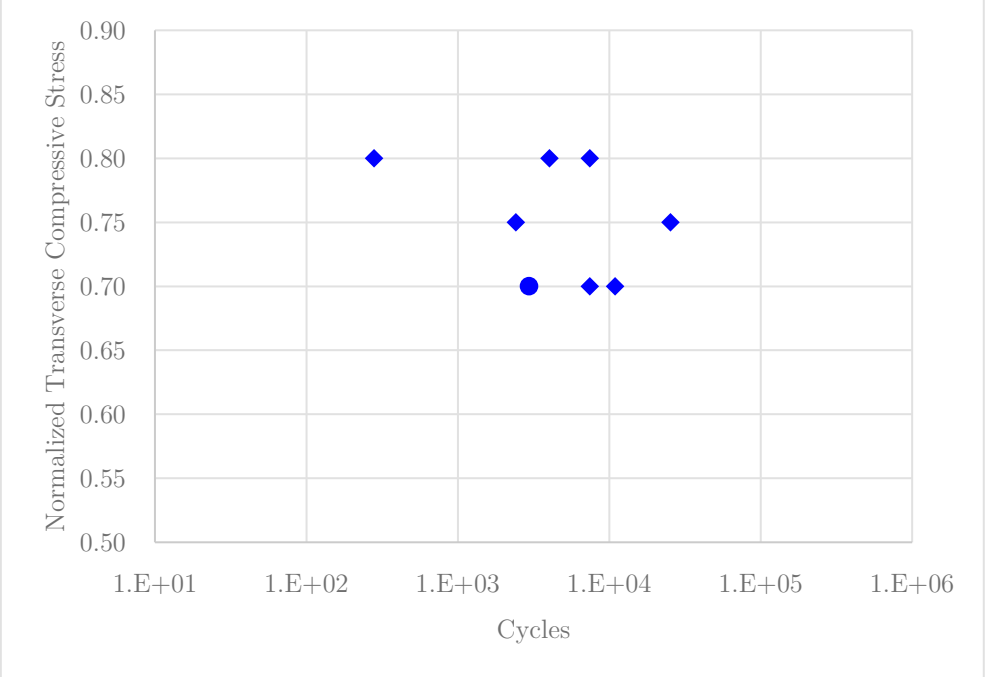

Figure 86. S-N data for lam $\lambda_{12} = 0.21$ (tubes). Diamond markers represent data points obtained at 10 Hz, while circle markers represent data points obtained at 5 Hz.

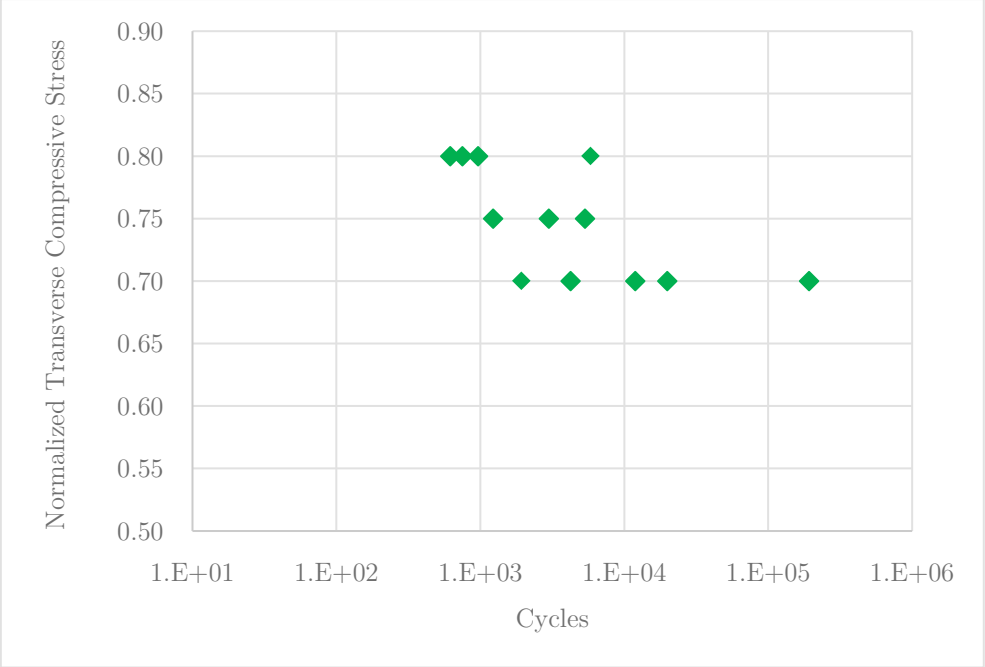

Figure 87. S-N data for lam $\lambda_{12} = 0.00$ (coupons).

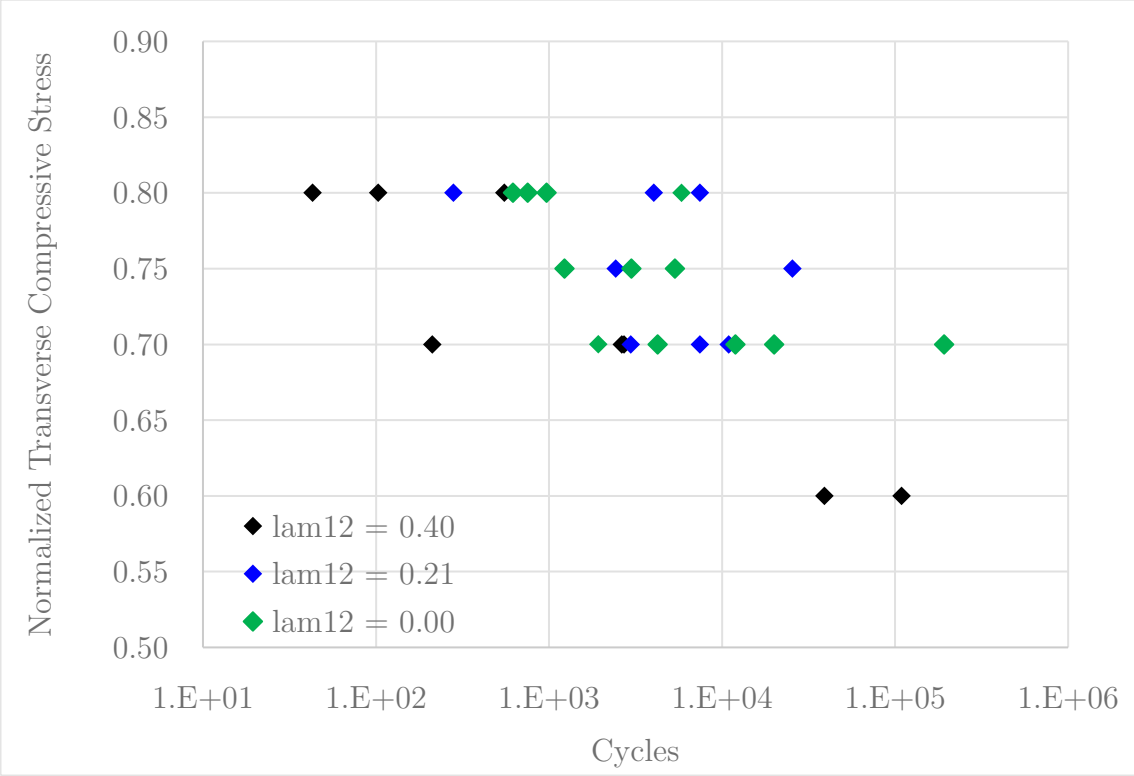

Figure 88. S-N data for all fatigue tests.

Comparing the results obtained from the tubular specimens ($\lambda_{12} = 0.40$ and $\lambda_{12} = 0.21$), it is evident that the crack initiation lifetime of the plies was shorted by approximately one order of magnitude when the presence of shear stress was increased between the two cases. Comparing tubular $\lambda_{12} = 0.21$ specimens and the rectangular unidirectional $\lambda_{12} = 0.00$ specimens did not reveal the same trend, with crack initiation lifetimes being well within each other's scatter. Consequently, either the increase in shear stress from 0% to 21% of the transverse stress had an insignificant effect on the S-N behaviour of these specimens, or the destructive effects of the additional shear stress were obscured by the geometric differences within the specimens (i.e. specimen curvature, differences in ply thickness, neighbouring ply effects, and stress concentration zones induced by the different test fixtures).

5.3.2 Stiffness Degradation

In addition to the direct visual imaging, sub-critical damage could be indirectly characterized by the degradation of stiffness over the lifetime of the specimen. As presented in Ref. [18], sudden and gradual changes in normalized stiffness over time are correlated with the initiation and multiplication of new cracks and the propagation of existing cracks, respectively.

Determination of the modulus requires strain mapping. Because the surface area of the tubes had to be available for crack viewing, strain could not be measured using DIC or extensometry. The limited number of specimens prioritized crack visualization over strain measurements. However, the material's stiffness over the course of the test could be characterized using the force, displacement, torque and rotary displacement data.

Both unidirectional transverse coupons and tubes exhibited very gradual increases in the peak-to-peak axial displacement and rotary displacement of the crossheads during the load-controlled fatigue tests, indicating gradual decreases in axial stiffness and rotary stiffness (shown below in Figure 89). While this suggests a corresponding change in the transverse modulus E_2 and the shear modulus G_{12}, such a relationship cannot be conclusively proven. The steady increase in the displacement – as opposed to the presence of multiple sudden increases – suggests that the observed behaviour is the result of a single crack which incrementally grew over the course of the test.

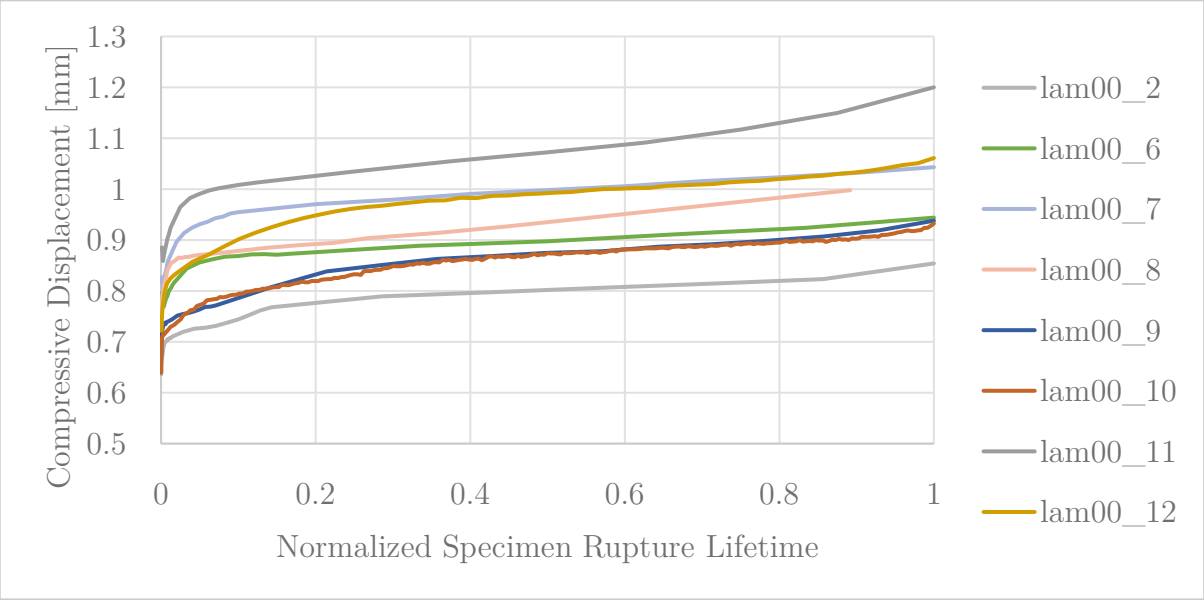

Figure 89. Change in cross-head displacement between peak loads in $\lambda_{12} = 0.00$ specimens. Tests which were restarted partially through the fatigue lifetime are omitted.

6 Discussion

6.1 Failure Modes and Surfaces

Failure modes during quasistatic testing match those that are typically observed in the literature, as shown in Figure 90.

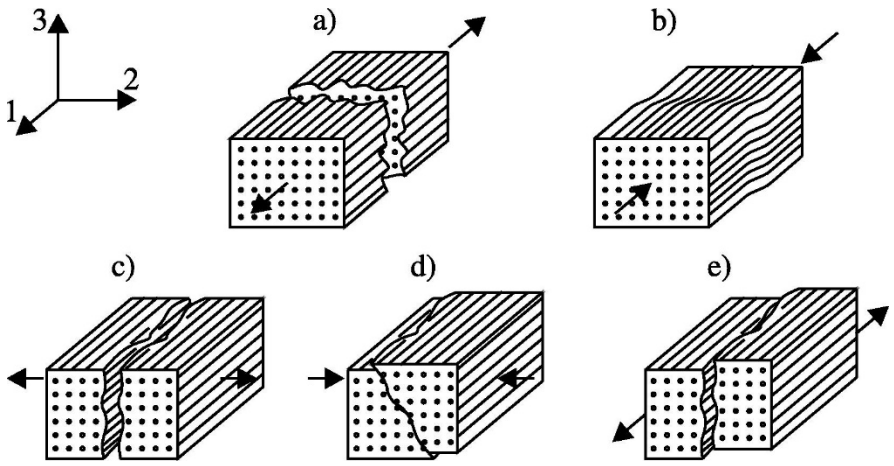

Figure 90. Failure modes of transversely isotropic laminate in (a) longitudinal tension, (b) longitudinal compression, (c) transverse tension, (d) transverse compression, and (e) in-plane shear (e) [95].

In longitudinal tension, individual weak fibres begin to fail one after another, transferring their stress to the other fibres and the matrix, which begins to split between fibres, resulting in a failed, broom-like specimen. In longitudinal compression, plies fail by the microbuckling of fibres, culminating in the formation of a kink-band.

In transverse tension, transverse compression, and shear loading, ply cracks begin to debond from the fibres and coalesce into a single large fracture. However, the locations and angles of the debonding vary. In transverse compression, a distinct fracture plane is observed at a 55° incline relative to the plane perpendicular to the loading direction. The difference in the fracture profiles around the circumference of a tube is schematically illustrated in Figure 91.

In longitudinal compressive loading, cracks typically will occur due to Poisson effects that induce transverse tensile failure. However, transverse compressive loading does not produce sufficient stress to cause splitting failure in the material due to the high longitudinal tensile strength of GFRPs. Consequently, the primary failure mode of the off-axis plies in this investigation will be transverse compressive failure.

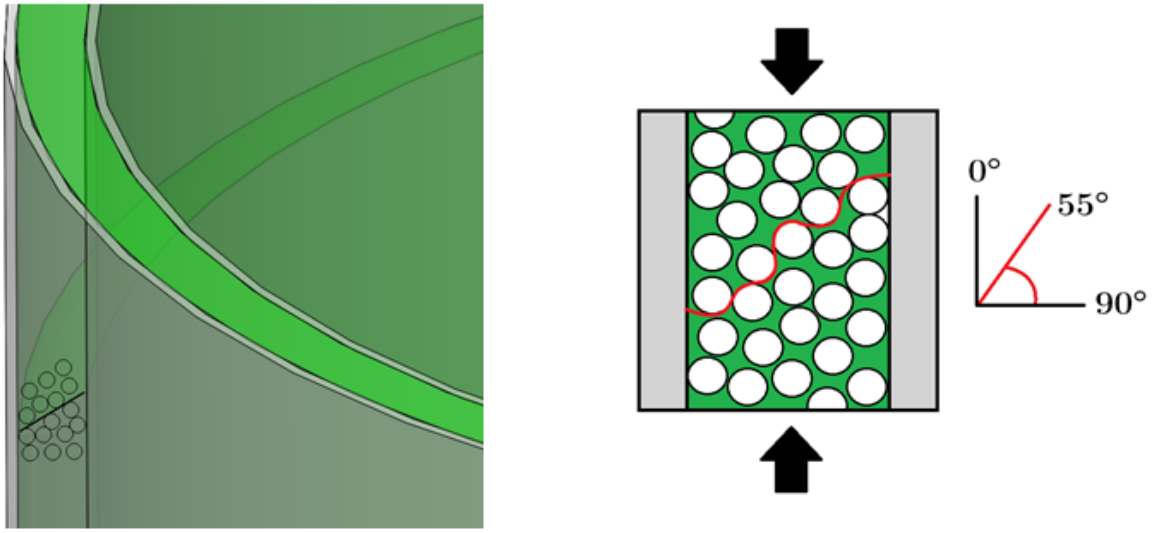

Figure 91. 3D (right) and 2D (left) schematics of circumferential propagation of transverse compressive cracks in tubes. The axes indicate the angle relative to the plane perpendicular to the loading direction, not the orientation of the fibres.

Under both quasistatic and cyclic combined loading, the most obvious difference between the compressive and tensile cases is the emergence of a single dominant crack in the former, and multiple cracks in the latter. As reported in literature and verified in the MD65-65 tensile specimens, tensile failure manifests as numerous transverse cracks, present along the entire length of the specimen [16]. By comparison, in both quasistatic and cyclic compression cases, damage would always progress from an initial failure locus. This finding was corroborated by a thermal camera, which showed cracks occurring in what would eventually be the failure locus.

Examination of fracture surfaces has several significant hurdles which hamper useful data collection. The first roadblock is that the preparation of the tubes for observation without damaging the fracture surface is extremely difficult. This is due to the following reasons:

- In compression, specimen rupture does not always cleanly separate the tube into multiple pieces. Parts above and below the failure surface can become jammed together. Pulling the pieces apart can cause additional damage to the fracture surface that is not representative of the true failure mode.
- The locking assemblies and cup fixtures are heavy, unstable on their stalks, and require loosening using Allen keys. If a specimen has failed and not separated into to pieces of its own accord, it is a single piece which is extremely weak at the failure surface (shown in Figure 92). Removing the tube from its unwieldy fixtures and removing the lighting apparatus without pulling apart the semi-intact specimen is extremely difficult.

The second roadblock to observing fracture surfaces is the inherent non-uniformity of the fracture surface. To observe the failure surface from the side, part of the tube must be removed such that a side-view can be achieved, as shown in Figure 93. However, there is no guarantee that a failure surface is uniform around the circumference of the tube. Microscopy of the failure surfaces of specimen QS02-1 (Figure 78) reveal that on opposite sides of the same specimen, the failure surfaces are *not* mirrored. Therefore, between the two points of observation, the failure surface "flips" over an unknown distance, or perhaps at a single point. As a result, it cannot be said with certainty if any given surface observed by microscopy is representative of the whole tube.

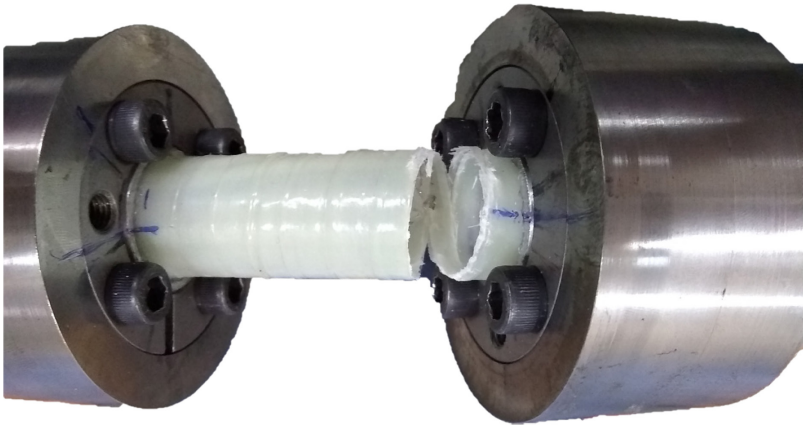

Figure 92. A semi-intact tube within the test fixtures.

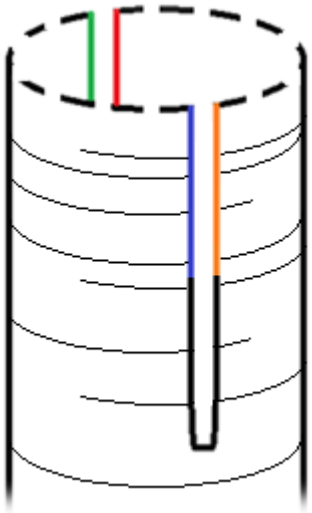

Figure 93. Schematic of a tube at the failure surface (dotted), sectioned to provide four visible regions (coloured) for fracture surface observation.

6.2 Feasibility of *in situ* Damage Monitoring in Compression

Part of the importance of this investigation was determining if visual monitoring of cracks in compression was possible. In tension, cracks are pulled apart, making them easier to visualize. It was initially unclear if cracks formed in compression would be visible at all, since they are not opened. Cracks formed in compression theoretically have no crack opening displacement, though they have a nonzero crack sliding displacement. Despite this, cracks were visible under cyclic loading, and to a lesser extent, under quasistatic loading.

However, an apparent mismatch between the loading and image capturing cameras prevented quantitative characterization of crack width relative to the applied load. To observe the change in crack width over the specimen lifetime, crack images should be taken at the same load each cycle (or set number of cycles). Otherwise, the crack may be appear to be very wide in one image and very narrow in the next. However, the equipment required to trigger image capturing by test frame outputs were not available. In test lam021_F2c70_1, the image capturing frequency was 0.01 Hz, theoretically one one-thousandth of the loading frequency (assumed to be exactly 10 Hz). Theoretically, if the frequencies were perfectly in phase, each image would be taken at precisely every thousandth peak load, and the decrease in stiffness in the damaged specimen would cause sequential images to show uniformly increasing deformation (i.e. each sequential frame should show slightly more twisting and compression than the previous frame). However, when combined into a video, it became clear that the entire specimen would "pulsate", changing from more to less to more deformed with each set of several frames. Test data revealed that the frequency of loading was controlled extremely precisely, suggesting that the images taken by the capture camera were taken at times not corresponding to peak loads. Figure 94 shows an arbitrary load vs. time curve, along with equally-spaced

image capture points representing the image capture frequency. As the test progresses, the images are different load levels throughout.

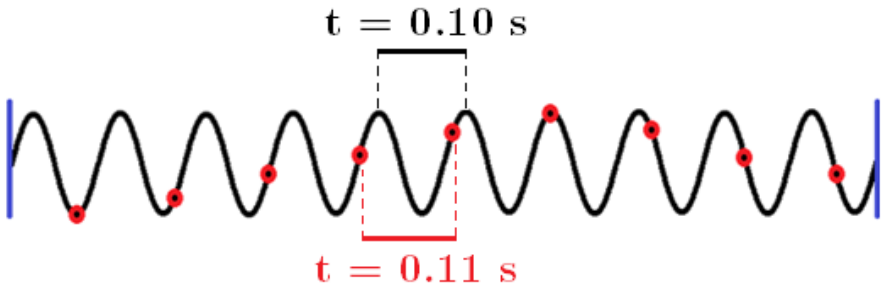

Figure 94. An arbitrary load vs. time curve (black), with slightly out-of-sync times of image capture (red).

The crack images from the test showed that once the initial crack was formed, it would become more visible as the magnitudes of the compressive load $|P|$ and the magnitude of the torque $|T|$ decreased. When $|P|$ and $|T|$ increased and stresses became more extreme, the crack appeared to close, but then reopen wider than before when $|P|$ and $|T|$ decreased Figure 95. This assumes that crack visibility is directly related to crack width, which is reasonable since crack depth can be assumed to be the thickness of the transverse plies, since they are relatively thin.

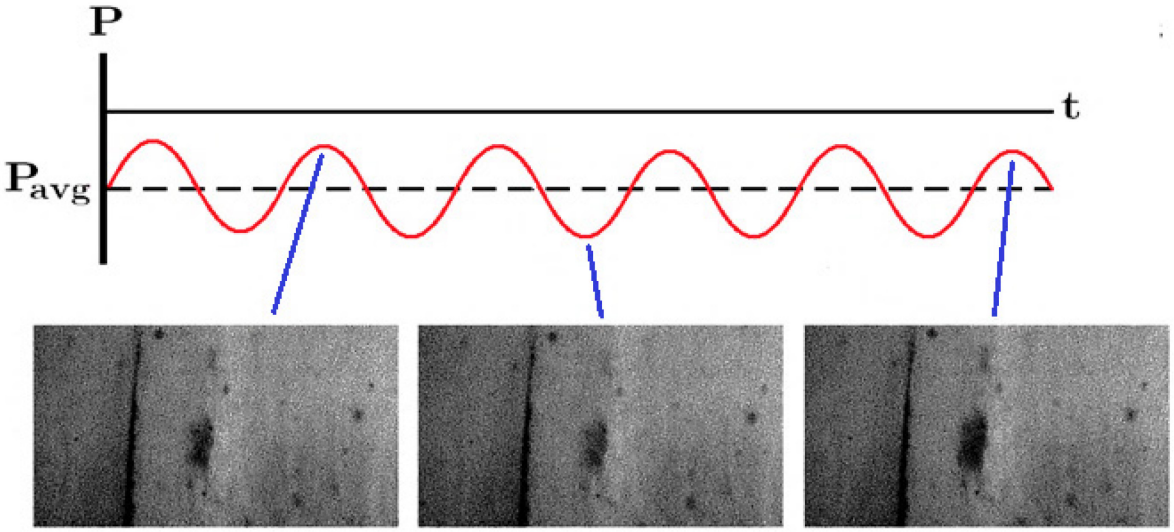

Figure 95. Load vs. time curve and images taken during crack pulsating showing crack opening, closing, and widened reopening at different load levels.

While the inconsistent load and torque levels are not useful to obtain qualitative data on crack width, this problem did provide some insight into the mechanism by which compressive cracks become visible. A mechanism proposed by this author hypothesises that during more intense compressive loads, the faces of an existing crack grind together and wear away a minute amount of material. When the loads are lessened, the crack faces are no longer forced against one another, and a void is formed where the material ground away would have been initially. During the next cycle, the void closes again (same peak load but with reduced stiffness, hence more displacement, and more material is ground away. Insufficient time has prevented more in-depth consideration of this phenomenon.

Another noteworthy aspect of monitoring crack initiation visually is the basis on which a researcher determines whether a crack has appeared or not. Determining whether a crack has occurred at all before failure is simple during cyclic loading, since the crack has a substantial amount of time to grow and become more visible before the specimen fails. When examining crack images, a researcher can be certain that a crack becomes visible (as shown in previous images in this document), establishing an upper bound on the cycle count at which the crack occurred. This is also true in quasistatic loading, but the existence of a crack is much more difficult to establish in quasistatic loading since the crack is so minute. However, what is more difficult is establishing the lower bound of crack initiation lifetime. Because the cracks are so minute, and manifest as gradual changes in local brightness, it can be difficult to determine the moment the change occurred. Figure 96 highlights an issue arising from this brightness change in the tubes vs. the unidirectional transverse specimens. The nature of transverse compression introduces an inclined fracture plane in all transverse plies. However, with a constant angle and different thicknesses, the length of the fracture plane is much longer in thicker specimens. As a result, thicker specimens have a much wider area that darkens over time

than the thin tube plies. If one uses contrast between the crack and its neighbouring regions to determine when cracks occur, the thin plies will appear to crack earlier, since the region of fracture is smaller, and thus produces more local contrast changes (see Figure 96).

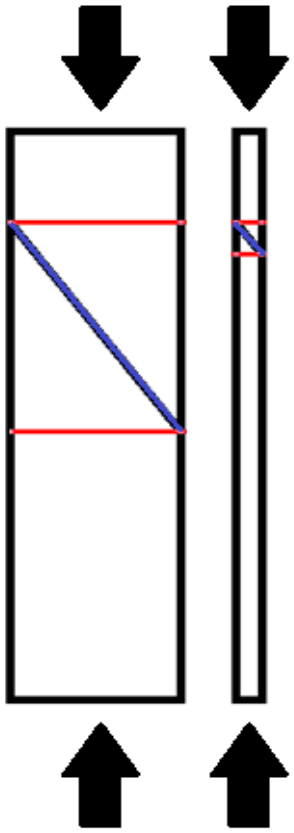

Figure 96. Schematic side-view comparison of the inclined transverse crack plane (blue) in thick (left) and thin (right) plies. The length of the fracture surface (distance between red regions) changes the relative contrast between crack areas and the neighbouring areas.

6.3 Stress-Life Data Scatter

The amount of scatter in the ply failure S-N data is substantial. The progression of damage in both metal and composite fatigue is sensitive to a wide variety of factors such as specimen geometry, defects, the presence of minute bending loads if the specimen is not inserted into the test frame properly, etc. These factors can all drastically influence the lifetime of specimens under theoretically identical stress states. Typically, fatigue studies involve a large sample size to mitigate the influence of these factors, though the number of specimens in this investigation were limited due to material and time constraints. However, the scatter in the S-N data obtained can be attributed to several critical factors beyond a simple shortage of specimens.

The first factor at play is the variations within the specimens themselves. Microscope imaging indicated that the surface wrinkles of the tubes were exclusively resin-rich areas, and that the wall thickness of and fibre-distribution within the transverse tube plies were relatively uniform, with few to no voids. However, minor wall thickness changes on the order of fractions of millimetres could still be measured. Additionally, because the tube was a closed section, only its ends could be measured, which may not be representative of the area of the plies at the region of ply failure. Loads and torques were applied to the specimens based on nominal area and wall thickness measurements taken as an average from multiple tubes. The discrepancy in area can introduce substantial variation, in contrast to typical metal dogbone specimens, which have easily-measured cross-section, and are machined to be virtually identical in dimension to one another.

The second factor that likely introduced substantial scatter into the S-N data was the method by which crack initiation lifetime measurements were made. Images taken during each test were examined frame by frame at the failure region (determined by the location of the final rupturing). As discussed in Section 4.5.2, the timing of each image could be

paired to a specific loading cycle within 1% of a specimen's total lifetime. Identifying the failure locus was simple by backtracking through the images, as the crack visibly expanded prior to failure over the course of the test. The progression of the crack is shown in Figure 97. Backtracking frame by frame would sequentially reduce the size of the crack, until a frame in which the crack was not visible.

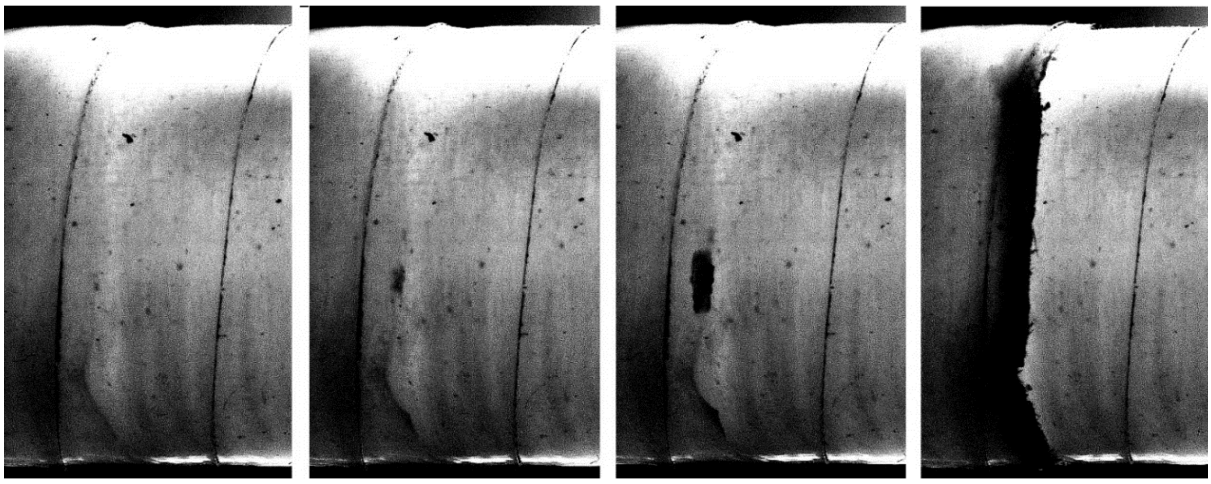

Figure 97. Images of a tube specimen during a cyclic test. From left to right: Prior to the start of the test, after crack initiation was established, immediately prior to rupture, and after rupture.

While identifying the failure locus was trivial, determination of the exact frame in which cracking initiates was subjective. A change in brightness at a specific location was the criterion for establishing crack initiation. However, as in Figure 97, several tests involved the initiation of a crack at a dark region already present within the specimen (either an internal defect, an artifact of the camera, or a contaminant on the specimen surface). Additionally, changes in brightness or contrast in such small areas can be difficult to detect, even with substantial image processing. Further, the exact manner in which a crack propagated within a specimen differed from specimen to specimen (this was not the case with the rectangular specimens, which all exhibited identical cracking mechanisms in the images taken). Figure 98 shows different cracking profiles in tubes immediately prior to failure. The disparity between these crack profiles is a substantial

barrier to the implementation of a hypothetical, image-processing based method for determining crack initiation using data such as the measurement of brightness or contrast changes from frame to frame.

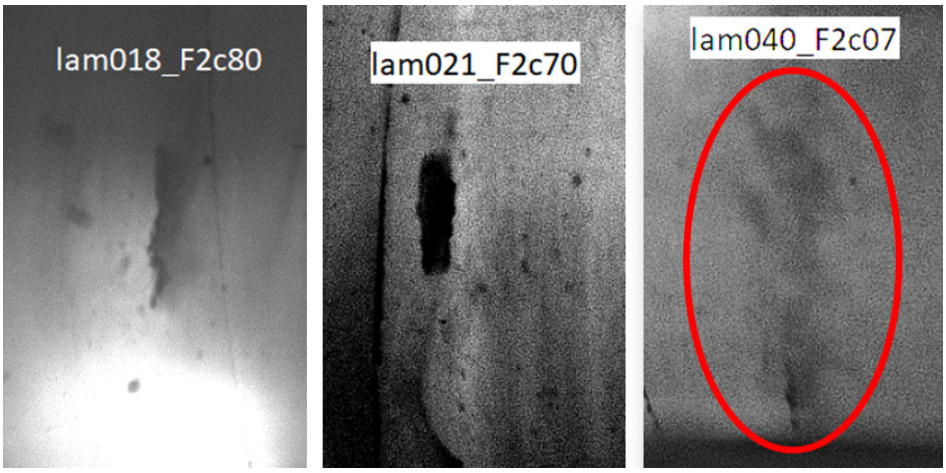

Figure 98. Differing crack profiles in three tube specimens.

6.4 Crack Propagation

The plots of crack initiation S-N curve and the specimen rupture S-N curve were initially predicted to make a wedge shape, as shown in Figure 99. It was thought that at stresses closer to the ultimate strength, ply failure would initiate sooner, and the specimen would experience a short propagation life under the high load. By comparison, specimens load at lower stresses would take longer to experience ply failure and would experience a much longer propagation life. Figure 100 shows a plot of the crack propagation lifetime based on the applied minimum transverse compressive stress for each of the different biaxiality ratios. The data is too limited and too sparse to draw any qualitative conclusions, though it is noted that the propagation lifetime is heavily subject to interpretation, based on the methods used to determine the time of crack initiation. Additional measurements made using a more consistent basis would allow a more complete understanding of this behaviour.

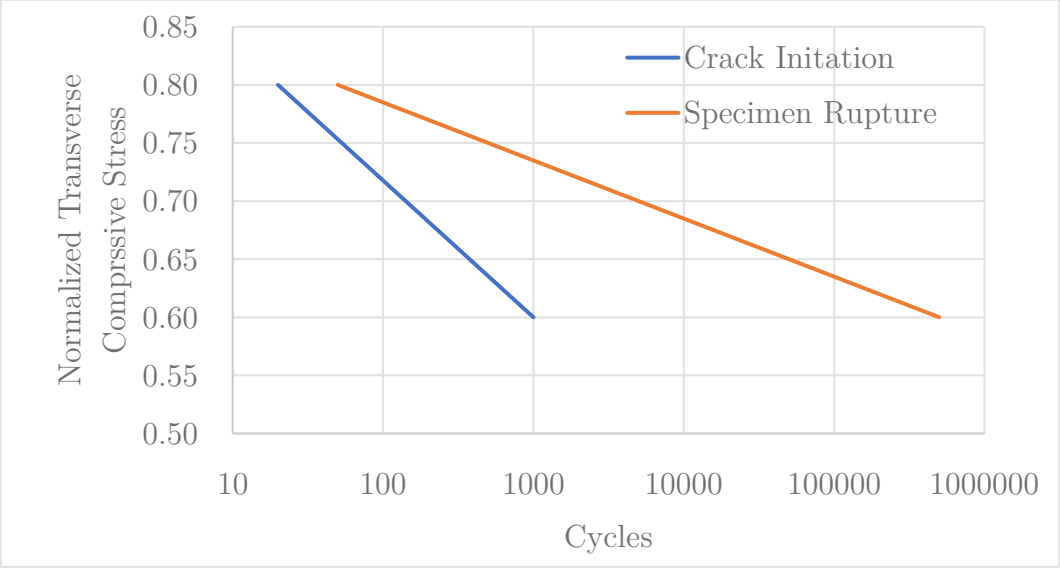

Figure 99. Qualitative prediction of crack initiation and rupture lifetime behaviour in cyclically loaded specimens.

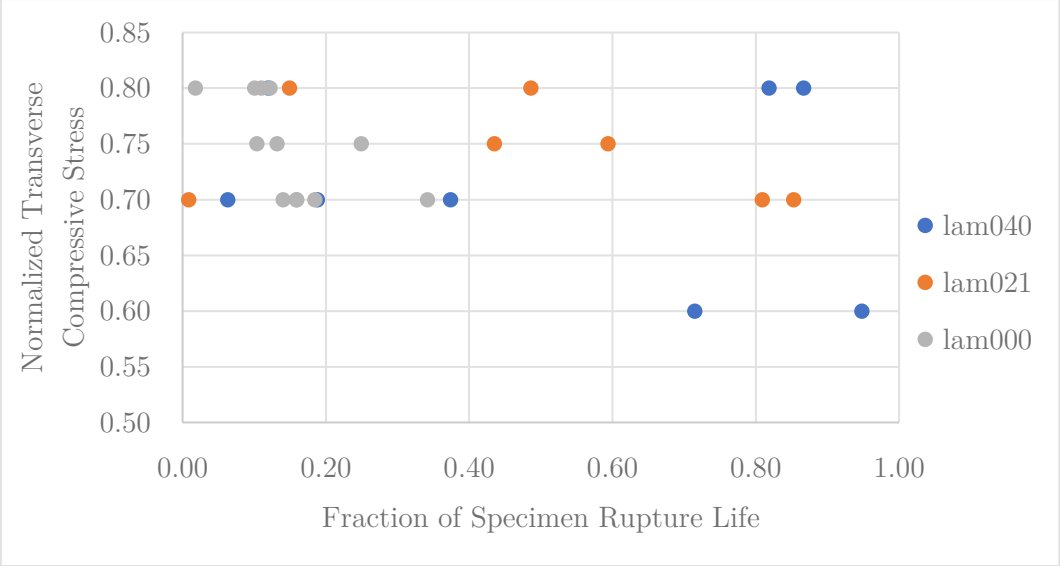

Figure 100. Plot of propagation lifetime as a function of the minimum applied transverse stress in tubular and coupon specimens.

It was predicted that unidirectional transverse plies would fail instantaneously at the moment of crack initiation, since they act as a single thick ply with no supporting layers. However, camera images showed the initiation of cracks prior to failure, giving these specimens a non-zero crack propagation life. There are two factors that may be influencing this behaviour. The first is that the unidirectional transverse specimens have twelve plies and are 3.5 mm thick on average. It is entirely possible that the specimen thickness is so large that a fracture plane cannot reasonably expand from a crack over such a wide area instantly. The second possible cause is that the included fracture plane was forcing the angled pieces of specimen away from each, but their movement was restricted by the anti-buckling fixture, which may have kept the entire specimen in one piece.

7 Conclusions

7.1 Conclusions

The objective of this investigation was to establish a fundamental understanding of damage initiation in multiaxial compressive stress states in tubular and rectangular laminates. Due to the limited time and number of specimens available for testing, quantitative conclusions could not be drawn, warranting additional experimentation. However, several qualitative conclusions were made from these results, which in light of the sparse nature of experimental work on the transverse compressive behaviour of laminates, are of great importance. Experimental work on the compressive behaviour of laminates is limited due in part to the numerous experimental complications associated with compressive testing, such as non-linear-elastic behavior, increased sensitivity to defects and misalignments, and buckling.

While not conclusions *per se*, the determination of optimal parameters and processes were the first critical findings of this investigation. The first of these processes was the establishment of a standard procedure for the bonding of aligned shell tabs to the tubes. Second was the design and machining of several of the fixtures used in this investigation, specifically the tube alignment fixtures and the windowed anti-buckling fixtures. Third was the development of a camera setup that allows the full characterization of tube surfaces, which can not only be used for crack monitoring, but also, theoretically, for digital image correlation.

The most fundamental of this investigation's qualitative conclusions is that compressive cracks can be visualized *in situ*. It was not initially known whether compression cracks would be visible, since there is no apparent crack opening displacement. It was theorized that infrared imaging would be required to determine where cracks initiated. In addition,

it was determined that as with purely tensile fatigue studies, the visibility (breadth) of a crack was greatest at the maximum load during cyclic testing (i.e. the least compressive load).

While only limited insight can be gleaned from the ply-failure S-N data, the detrimental effects of shear stress on specimens loaded in compression is clear and follows a generally similar trend as has been reported in tension. However, the magnitude of shear's effect on crack initiation lifetime in compression vs. tension has not yet been explored.

7.2 Recommendations

Additional experimentation is required to establish more a more concrete basis of modelling crack initiation in combined compression-shear loading. This section discusses elements of this investigation that can be improved going forward.

7.2.1 Recommendations for Going Forward

One of the most significant hurdles in this investigation was the quality of the cylinders, specifically the outer surface roughness. The poor surface quality necessitated a substantial time investment into shell tab and fixture machining, and the tab alignment process. While the processes for manufacturing the cylinders was performed meticulously by collaborators at the National Research Council, the cylinders were made by hand. Additional processing equipment would allow for more improved control of specimen quality. For example, a machine to precisely control the tension and winding angle of the shrink tape around the prepregs would decrease the presence of resin-rich bulges on the surfaces.

Another hurdle in this investigation was the limited availability of testing frames. While the convenience of a readily-available test frame cannot be overstated, the use of a single machine in highly-sensitive cyclic tests is recommended. Additionally, unforeseen complications necessitating troubleshooting occurred between almost every test (e.g. unpredicted buckling and improper test failure). For example, the dynamic windowed anti-buckling fixture in Section 4.3 was designed and machined in one day due the limited time available for testing on the Instron 8872. The fixture did prevent buckling, but experienced rapid wear in its Teflon layers because compression springs could not be found in the right length and stiffness in such a short time. The Teflon wear could

have increased friction between the fixture and specimen and introduced damage on the specimen surfaces.

Based on the apparently dramatic increase of *in situ* ply strengths, the use of a higher-capacity test frame is suggested. A test frame with higher load and torque capacity would allow for the testing of thicker laminates, which would have reduced *in situ* effects. A higher-capacity test frame could also test thin laminate with high *in situ* strengths, though the effects of the increased *in situ* strength on the S-N behavior are difficult to quantify.

Based on the S-bending present in compressive specimens, it is evident that not only do compression tests warrant anti-buckling fixtures, but also alignment fixtures such as the IITRI fixture, the Celanese fixture or a combined loading compression fixture described in ASTM D6641.

The lighting apparatus can be improved since it is no longer constrained by batteries, though space is still a limiting factor. The uniform dispersion of light is critical, since the presence of bright spots from LEDs greatly reduced the degree to which crack images could be postprocessed usefully.

Determination of modulus degradation is critical. With additional specimens, measurement of strain using an extensometer or digital image correlation can be done. Stiffness measurements provided a basis for further examination, but they are not as conclusive as local and global modulus measurements.

The cyclic loading of the specimens and the cyclic capturing of crack images were entirely independent processes that were semi-synchronized after the completion of the test. As a result, the loading and image capture frequencies were observed to be slightly different,

causing crack images to be taken under different load levels. Additionally, the camera was not necessarily capturing images at the peak loads, even if the loading and capture frequencies were identical. It is therefore recommended that to improve crack visibility, further work should incorporate image capturing equipment that can be triggered by test frame output (e.g. voltage triggered-image capturing, corresponding to peak loads). Image capturing at a range of stresses (not only peak stresses) could also shed more light on the effects of loading on crack visibility, and the possible mechanisms of the apparent crack widening under cyclic transverse compressive loading.

Determination of crack length and its effect on stiffness degradation is an element of this investigation that was not determined. Using a camera setup of two cameras and two mirrors, each tube was viewed from three different angles. While the entire tube was visible for the sake of determining if a crack was present, cracks that occur at the edge of the specimen relative to the camera are tangential to the light path of the camera, making crack growth difficult to characterize, since cracks grow towards the camera. A more complex array of viewing angles would improve crack length visibility.

To see the entire fracture surface as a whole and to prevent additional damage, fracture surfaces in the tubes should be viewed intact from above, not from the side after the specimen is sectioned. The use of a high resolution optical microscope is recommended, as is the use of an SEM if the specimen can be properly mounted and coated.

7.3 Areas for Future Investigation

Before research into different areas can begin, this investigation must first be concluded. Specifically, this includes several facets of additional experimentation and analysis:

- Additional cyclic crack-monitoring tests on tubes and multidirectional coupons to establish ply-failure S-N trends
- Comparison of ply-failure S-N trends between the two specimen types
- Strain measurements to quantify stiffness degradation during cyclic loading
- Development of a consistent, quantitative benchmark for establishing crack initiation lifetime with image-processing techniques

Beyond the quantitative conclusions that the experiments above can reveal, the qualitative findings of these experiments have revealed a variety of new avenues of research, which can be investigated using specimens made from the excess of prepreg obtained from Composite Materials Italy.

This investigation focused the fatigue behaviour of plies under constant amplitude, load-controlled tests. However, the contribution of different stress states to the progression of damage can be studied in cases such as variable-amplitude loading, combined shear and tension-compression loading, and strain-controlled loading. Additionally, the effects of shear stress on specimens in C-C, C-T, and T-T fatigue can be quantified.

Using extensometry or digital image correlation with the camera and mirror setup, strain mapping can be done on additional specimens to determine the effects of compressive cracking on local or global moduli.

The improved *in situ* transverse compressive and shear strengths observed in the MD16-65 laminates were unaccounted for in experimental design calculations, as this phenomenon is not present in the literature to any great degree, and certainly not in the form of experimental findings. Using panels with different layups and ply thicknesses, experimental investigation of the improved *in situ* strengths with respect to ply thickness and adjacent ply angle could be conducted. A deeper dive into this study could include a comparison of the *in situ* shear strengths of a sandwiched 45° loaded in tension and compression.

The modified Euler buckling formula using the out of plane bending stiffness D_{11}^{*} did not appear to accurately predict the loads at which buckling occurred. This is either due to the inception of buckling being extremely difficult to observe *in situ*, or otherwise unknown factors not considered in the translation from the buckling of homogenous materials to that of laminates. Using a device such as a laser distance measure, additional tests can be performed to determine at exactly what loads a given laminate buckles and develop a more accurate semi-empirical model for buckling behaviour.

Using a more complex system of cameras, crack growth due could be more accurately characterized (fewer surfaces tangential to the cameras). Crack length could be more easily measured, providing insight into the mechanisms of crack growth and their effects on specimen stiffness.

References

[1] Agarwal, B. D., Broutman, L. J., and Chandrashekhara, K., 2006, *Analysis and Performance of Fiber Composites*, John Wiley, Hoboken, N.J.

[2] Malnati, P., "A Hidden Revolution: FRP Rebar Gains Strength" [Online]. Available: https://www.compositesworld.com/articles/a-hidden-revolution-frp-rebar-gains-strength. [Accessed: 08-May-2018].

[3] "COMPOSITES 101 | Quartus Engineering" [Online]. Available: https://www.quartus.com/resources/composites-101/. [Accessed: 07-May-2018].

[4] Mishnaevsky, L., Branner, K., Petersen, H., Beauson, J., McGugan, M., and Sørensen, B., 2017, "Materials for Wind Turbine Blades: An Overview," Materials, **10**(11), p. 1285.

[5] Staff, "The Markets: Automotive (2017)" [Online]. Available: https://www.compositesworld.com/articles/the-markets-automotive-2016. [Accessed: 08-May-2018].

[6] "2016 McLaren 570S Dissected | Feature," Car Driv. [Online]. Available: http://www.caranddriver.com/features/2016-mclaren-570s-dissected-feature. [Accessed: 26-Apr-2018].

[7] 2009, "Aston Martin One-77 Supercar: Carbon Fiber In The Raw," Carbon Fiber Gear.

[8] "BMW i3 Pioneers Use of Carbon Fiber in Mass-Produced Cars," Automot. News [Online]. Available: http://www.autonews.com/article/20131115/COPY01/311159959/bmw-i3-pioneers-use-of-carbon-fiber-in-mass-produced-cars. [Accessed: 26-Apr-2018].

[9] "Boeing: 787 By Design" [Online]. Available: https://www.boeing.com/commercial/787/by-design/#/advanced-composite-use. [Accessed: 26-Apr-2018].

[10] Kluke, M., 2018, "The Joining of Composite Materials: The Best of Both Worlds," Reinf. Plast., **62**(2), pp. 79–81.

[11] Taylor, N. S., Jones, S. B., and Weld, M., 1989, "The Feasibility of Welding Thermoplastic Composite Materials," Constr. Build. Mater., **3**(4), pp. 213–219.

[12] Vassilopoulos, A. P., and Keller, T., 2011, *Fatigue of Fiber-Reinforced Composites*, Springer London, London.

[13] Kaddour, A., Hinton, M., Smith, P., and Li, S., 2013, "Mechanical Properties and Details of Composite Laminates for the Test Cases Used in the Third World-Wide Failure Exercise," J. Compos. Mater., **47**(20–21), pp. 2427–2442.

[14] Belinky, A., 1994, "High Cycle Compressive Fatigue of Unidirectional Glass/Polyester Performed at High Frequency," Master of Science, Montana State University.

[15] Tsai, S. W., and Pagano, N. J., 1968, *Invariant Properties of Composite Materials*, Technomic Publishing Company.

[16] Quaresimin, M., Carraro, P. A., Mikkelsen, L. P., Lucato, N., Vivian, L., Brøndsted, P., Sørensen, B. F., Varna, J., and Talreja, R., 2014, "Damage Evolution under Cyclic Multiaxial Stress State: A Comparative Analysis between Glass/epoxy Laminates and Tubes," Compos. Part B Eng., **61**, pp. 282–290.

[17] Quaresimin, M., and Carraro, P. A., 2013, "On the Investigation of the Biaxial Fatigue Behaviour of Unidirectional Composites," Compos. Part B Eng., **54**, pp. 200–208.

[18] Quaresimin, M., and Carraro, P. A., 2014, "Damage Initiation and Evolution in Glass/epoxy Tubes Subjected to Combined Tension–torsion Fatigue Loading," Int. J. Fatigue, **63**, pp. 25–35.

[19] Montesano, J., and Singh, C. V., 2015, "A Synergistic Damage Mechanics Based Multiscale Model for Composite Laminates Subjected to Multiaxial Strains," Mech. Mater., **83**, pp. 72–89.

[20] Owen, M. J., and Found, M. S., 1972, "Static and Fatigue Failure of Glass Fibre Reinforced Polyster Resins under Complex Stress Conditions," Faraday Spec. Discuss. Chem. Soc., **2**, p. 77.

[21] Owen, M. J., and Found, M. S., 1975, "The Fatigue Behaviour of a Glass-Fabric-Reinforced Polyester Resin under off-Axis Loading," J. Phys. Appl. Phys., **8**(5), pp. 480–497.

[22] Chang, F., Gordon, D., and Gardner, A., 1977, "A Study of Fatigue Damage in Composites by Nondestructive Testing Techniques," *Fatigue of Filamentary Composite Materials*, K. Reifsnider, and K. Lauraitis, eds., ASTM International, 100 Barr Harbor Drive, PO Box C700, West Conshohocken, PA 19428-2959, pp. 57-57–16.

[23] Francis, P. H., Walrath, D. E., Sims, D. F., and Weed, D. N., 1977, "Biaxial Fatigue Loading of Notched Composites," J. Compos. Mater., **11**(4), pp. 488–501.

[24] Parvizi, A., Garrett, K. W., and Bailey, J. E., 1978, "Constrained Cracking in Glass Fibre-Reinforced Epoxy Cross-Ply Laminates," J. Mater. Sci., **13**(1), pp. 195–201.

[25] Owen, M. J., and Griffiths, J. R., 1978, "Evaluation of Biaxial Stress Failure Surfaces for a Glass Fabric Reinforced Polyester Resin under Static and Fatigue Loading," J. Mater. Sci., **13**(7), pp. 1521–1537.

[26] Flaggs, D. L., and Kural, M. H., 1982, "Experimental Determination of the In Situ Transverse Lamina Strength in Graphite/Epoxy Laminates," J. Compos. Mater., **16**(2), pp. 103–116.

[27] Perevozchikov, V. G., Limonov, V. A., Protasov, V. D., and Tamuzh, V. P., 1989, "Static and Fatigue Strength of Unidirectional Composites under the Combined Effect of Shear Stress and Transverse Tension-Compression Stresses," Mech. Compos. Mater., **24**(5), pp. 638–644.

[28] Anderson, Y. A., Limonov, V. A., Tamuzh, V. P., and Perevozchikov, V. G., 1990, "Fatigue of Laminated Composites with Various Reinforcement Systems. 2. Planar Stress State and Calculation Model," Mech. Compos. Mater., **25**(4), pp. 442–449.

[29] Lafarie-Frenot, M. C., and Hénaff-Gardin, C., 1991, "Formation and Growth of 90° Ply Fatigue Cracks in Carbon/epoxy Laminates," Compos. Sci. Technol., **40**(3), pp. 307–324.

[30] Anderson, Y. A., Limonov, V. A., and Tamuzh, V. P., 1992, "Effect of Phase Asynchronism on the Fatigue Resistance of Laminated Fiber Composites in a Plane Stress State," Mech. Compos. Mater., **27**(5), pp. 521–529.

[31] Atcholi, K. E., Oytana, C., Varchon, D., and Perreux, D., 1992, "Superposed Torsion-Flexure of Composite Materials: Experimental Method and Example of Application," Composites, **23**(5), pp. 327–333.

[32] Andersons, J., Lomonov, V., Mikelsons, M., and Tamužs, V., 1994, "Strength and Durability of Mixed Glass-Fibre-Reinforced Laminates," Mech. Compos. Mater., **30**(1), pp. 22–29.

[33] Takemura, K., and Fujii, T., 1994, "Fatigue Strength and Damage Progression in a Circular-Hole-Notched GRP Composite under Combined Tension/torsion Loading," Compos. Sci. Technol., **52**(4), pp. 519–526.

[34] Fujii, T., Shiina, T., and Okubo, K., 1994, "Fatigue Notch Sensitivity of Glass Woven Fabric Composites Having a Circular Hole under Tension/Torsion Biaxial Loading," J. Compos. Mater., **28**(3), pp. 234–251.

[35] Fujii, T., and Lin, F., 1995, "Fatigue Behavior of a Plain-Woven Glass Fabric Laminate under Tension/Torsion Biaxial Loading," J. Compos. Mater., **29**(5), pp. 573–590.

[36] Wafa, M. N. A., Hamdy, A. H., and El-Midany, A. A., 1997, "Combined Bending and Torsional Fatigue of Woven Roving GRP," J. Eng. Mater. Technol., **119**(2), p. 180.

[37] Perreux, D., and Joseph, E., 1997, "The Effect of Frequency on the Fatigue Performance of Filament-Wound Pipes under Biaxial Loading: Experimental Results and Damage Model," Compos. Sci. Technol., **57**(3), pp. 353–364.

[38] Praveen, G. N., and Reddy, J. N., 1998, "Transverse Matrix Cracks in Cross-Ply Laminates: Stress Transfer, Stiffness Reduction and Crack Opening Profiles," Acta Mech., **130**(3–4), pp. 227–248.

[39] Ferry, L., 1999, "Fatigue Behaviour of Composite Bars Subjected to Bending and Torsion," Compos. Sci. Technol., **59**(4), pp. 575–582.

[40] Varna, J., 1999, "Damage in Composite Laminates with off-Axis Plies," Compos. Sci. Technol., **59**(14), pp. 2139–2147.

[41] Adden, S., Pfleiderer, K., Solodov, I., Horst, P., and Busse, G., 2008, "Characterization of Stiffness Degradation Caused by Fatigue Damage in Textile Composites Using Circumferential Plate Acoustic Waves," Compos. Sci. Technol., **68**(7–8), pp. 1616–1623.

[42] Quaresimin, M., Susmel, L., and Talreja, R., 2010, "Fatigue Behaviour and Life Assessment of Composite Laminates under Multiaxial Loadings," Int. J. Fatigue, **32**(1), pp. 2–16.

[43] Olsson, R., 2011, "A Survey of Test Methods for Multiaxial and out-of-Plane Strength of Composite Laminates," Compos. Sci. Technol., **71**(6), pp. 773–783.

[44] Schmidt, F., Rheinfurth, M., Protz, R., Horst, P., Busse, G., Gude, M., and Hufenbach, W., 2012, "Monitoring of Multiaxial Fatigue Damage Evolution in Impacted Composite Tubes Using Non-Destructive Evaluation," Compos. Part Appl. Sci. Manuf., **43**(3), pp. 537–546.

[45] Schmidt, F., Rheinfurth, M., Horst, P., and Busse, G., 2012, "Effects of Local Fibre Waviness on Damage Mechanisms and Fatigue Behaviour of Biaxially Loaded Tube Specimens," Compos. Sci. Technol., **72**(10), pp. 1075–1082.

[46] Schmidt, F., Rheinfurth, M., Horst, P., and Busse, G., 2012, "Multiaxial Fatigue Behaviour of GFRP with Evenly Distributed or Accumulated Voids Monitored by Various NDT Methodologies," Int. J. Fatigue, **43**, pp. 207–216.

[47] Capela, C., Ferreira, J. A. M., Febra, T., and Costa, J. D., 2015, "Fatigue Strength of Tubular Carbon Fibre Composites under Bending/torsion Loading," Int. J. Fatigue, **70**, pp. 216–222.

[48] Quaresimin, M., 2015, "50th Anniversary Article: Multiaxial Fatigue Testing of Composites: From the Pioneers to Future Directions: Multiaxial Fatigue Testing of Composites," Strain, **51**(1), pp. 16–29.

[49] Kosmann, N., Karsten, J. M., Schuett, M., Schulte, K., and Fiedler, B., 2015, "Determining the Effect of Voids in GFRP on the Damage Behaviour under Compression Loading Using Acoustic Emission," Compos. Part B Eng., **70**, pp. 184–188.

[50] Li, W., Cai, H., Li, C., Wang, K., and Fang, L., 2015, "Micro-Mechanics of Failure for Fatigue Strength Prediction of Bolted Joint Structures of Carbon Fiber Reinforced Polymer Composite," Compos. Struct., **124**, pp. 345–356.

[51] Quaresimin, M., Carraro, P. A., and Maragoni, L., 2015, "Influence of Load Ratio on the Biaxial Fatigue Behaviour and Damage Evolution in Glass/epoxy Tubes under Tension–torsion Loading," Compos. Part Appl. Sci. Manuf., **78**, pp. 294–302.

[52] Krishnan, P., Abdul Majid, M. S., Afendi, M., Gibson, A. G., and Marzuki, H. F. A., 2015, "Effects of Winding Angle on the Behaviour of Glass/epoxy Pipes under Multiaxial Cyclic Loading," Mater. Des., **88**, pp. 196–206.

[53] Quaresimin, M., Carraro, P. A., and Maragoni, L., 2016, "Early Stage Damage in off-Axis Plies under Fatigue Loading," Compos. Sci. Technol., **128**, pp. 147–154.

[54] Hörrmann, S., Adumitroaie, A., Viechtbauer, C., and Schagerl, M., 2016, "The Effect of Fiber Waviness on the Fatigue Life of CFRP Materials," Int. J. Fatigue, **90**, pp. 139–147.

[55] Dong, H., Li, Z., Wang, J., and Karihaloo, B. L., 2016, "A New Fatigue Failure Theory for Multidirectional Fiber-Reinforced Composite Laminates with Arbitrary Stacking Sequence," Int. J. Fatigue, **87**, pp. 294–300.

[56] Walsh, R. P., McColskey, J. D., and Reed, R. P., 1995, "Low Temperature Properties of a Unidirectionally Reinforced Epoxy Fibreglass Composite," Cryogenics, **35**(11), pp. 723–725.

[57] Kawai, M., Yajima, S., Hachinohe, A., and Kawase, Y., 2001, "High-Temperature off-Axis Fatigue Behaviour of Unidirectional Carbon-Fibre-Reinforced Composites with Different Resin Matrices," Compos. Sci. Technol., **61**(9), pp. 1285–1302.

[58] Ray, B. C., 2006, "Temperature Effect during Humid Ageing on Interfaces of Glass and Carbon Fibers Reinforced Epoxy Composites," J. Colloid Interface Sci., **298**(1), pp. 111–117.

[59] Aktaş, M., and Karakuzu, R., 2009, "Determination of Mechanical Properties of Glass-Epoxy Composites in High Temperatures," Polym. Compos., **30**(10), pp. 1437–1441.

[60] DiBenedetto, A. T., 2001, "Tailoring of Interfaces in Glass Fiber Reinforced Polymer Composites: A Review," Mater. Sci. Eng. A, **302**(1), pp. 74–82.

[61] Tan, W., Naya, F., Yang, L., Chang, T., Falzon, B. G., Zhan, L., Molina-Aldareguía, J. M., González, C., and Llorca, J., 2018, "The Role of Interfacial Properties on the Intralaminar and Interlaminar Damage Behaviour of Unidirectional Composite Laminates: Experimental Characterization and Multiscale Modelling," Compos. Part B Eng., **138**, pp. 206–221.

[62] Arteiro, A., Catalanotti, G., Melro, A. R., Linde, P., and Camanho, P. P., 2015, "Micro-Mechanical Analysis of the Effect of Ply Thickness on the Transverse Compressive Strength of Polymer Composites," Compos. Part Appl. Sci. Manuf., **79**, pp. 127–137.

[63] Loukil, M. S., Varna, J., and Ayadi, Z., 2013, "Engineering Expressions for Thermo-Elastic Constants of Laminates with High Density of Transverse Cracks," Compos. Part Appl. Sci. Manuf., **48**, pp. 37–46.

[64] Calcaterra, J., 1999, "Strength Degradation during Fatigue of Unidirectional and Cross-Ply SCS-6/Ti-15-3 Composites," Int. J. Fatigue, **21**(3), pp. 215–223.

[65] Lundmark, P., 2005, "Constitutive Relationships for Laminates with Ply Cracks in In-Plane Loading," Int. J. Damage Mech., **14**(3), pp. 235–259.

[66] Singh, C. V., and Talreja, R., 2009, "A Synergistic Damage Mechanics Approach for Composite Laminates with Matrix Cracks in Multiple Orientations," Mech. Mater., **41**(8), pp. 954–968.

[67] Montesano, J., and Singh, C. V., 2015, "Predicting Evolution of Ply Cracks in Composite Laminates Subjected to Biaxial Loading," Compos. Part B Eng., **75**, pp. 264–273.

[68] Montesano, J., and Singh, C. V., 2016, "Critical Stiffness Damage Envelopes for Multidirectional Laminated Structures under Multiaxial Loading Conditions," Mater. Des., **91**, pp. 218–229.

[69] González, C., and LLorca, J., 2007, "Mechanical Behavior of Unidirectional Fiber-Reinforced Polymers under Transverse Compression: Microscopic Mechanisms and Modeling," Compos. Sci. Technol., **67**(13), pp. 2795–2806.

[70] Canal, L. P., Segurado, J., and LLorca, J., 2009, "Failure Surface of Epoxy-Modified Fiber-Reinforced Composites under Transverse Tension and out-of-Plane Shear," Int. J. Solids Struct., **46**(11–12), pp. 2265–2274.

[71] Rasheed, H. A., 2015, *Strengthening Design of Reinforced Concrete with FRP*, CRC Press/Taylor & Francis Group, Boca Raton.

[72] Clements, L. L., and Moore, R. L., 1978, "Composite Properties for E-Glass Fibres in a Room Temperature Curable Epoxy Matrix," Composites, **9**(2), pp. 93–99.

[73] Naik, N. K., and Kumar, R. S., 1999, "Compressive Strength of Unidirectional Composites: Evaluation and Comparison of Prediction Models," Compos. Struct., **46**(3), pp. 299–308.

[74] Benzarti, K., Cangemi, L., and Dal Maso, F., 2001, "Transverse Properties of Unidirectional Glass/epoxy Composites: Influence of Fibre Surface Treatments," Compos. Part Appl. Sci. Manuf., **32**(2), pp. 197–206.

[75] Abdel-Magid, B., Ziaee, S., Gass, K., and Schneider, M., 2005, "The Combined Effects of Load, Moisture and Temperature on the Properties of E-Glass/epoxy Composites," Compos. Struct., **71**(3–4), pp. 320–326.

[76] Devendra, K., and Rangaswamy, T., 2013, "Strength Characterization of E-Glass Fiber Reinforced Epoxy Composites with Filler Materials," J. Miner. Mater. Charact. Eng., **1**(6), pp. 353–357.

[77] Uddin, M. F., and Sun, C. T., 2008, "Strength of Unidirectional Glass/epoxy Composite with Silica Nanoparticle-Enhanced Matrix," Compos. Sci. Technol., **68**(7–8), pp. 1637–1643.

[78] Dogan, A., and Atas, C., 2016, "Variation of the Mechanical Properties of E-Glass/epoxy Composites Subjected to Hygrothermal Aging," J. Compos. Mater., **50**(5), pp. 637–646.

[79] Bledzki, A. ., Kessler, A., Rikards, R., and Chate, A., 1999, "Determination of Elastic Constants of Glass/epoxy Unidirectional Laminates by the Vibration Testing of Plates," Compos. Sci. Technol., **59**(13), pp. 2015–2024.

[80] Soden, P., 1998, "Lamina Properties, Lay-up Configurations and Loading Conditions for a Range of Fibre-Reinforced Composite Laminates," Compos. Sci. Technol., **58**(7), pp. 1011–1022.

[81] Shokrieh, M. M., Heidari-Rarani, M., and Ayatollahi, M. R., 2012, "Delamination R-Curve as a Material Property of Unidirectional Glass/epoxy Composites," Mater. Des., **34**, pp. 211–218.

[82] Bertholet, J.-M., 1999, *Composite Materials: Mechanical Behavior and Structural Analysis*, Springer, New York.

[83] Vinson, J. R., and Sierakowski, R. L., 2002, *The Behavior of Structures Composed of Composite Materials*, Kluwer Academic Publishers, Dordrecht ; Boston.

[84] Nemeth, M., and Mikulas, M., 2009, "Simple Formulas and Results for Buckling-Resistance and Stiffness Design of Compression-Loaded Laminated-Composite Cylinders."

[85] Xie, M., and Adams, D. F., 1995, "Tab Adhesive in a Composite Compression Specimen," Polym. Compos., **16**(6), pp. 529–535.

[86] Bailey, P. B. S., and Lafferty, A. D., 2015, "Specimen Gripping Effects in Composites Fatigue Testing -– Concerns from Initial Investigation," Express Polym. Lett., **9**(5), pp. 480–488.

[87] Abdul Majid, M. S., Afendi, M., Daud, R., Gibson, A. G., Assaleh, T. A., Hale, J. M., and Hekman, M., 2015, "Acoustic Emission Monitoring of Multiaxial Ultimate Elastic Wall Stress Tests of Glass Fibre-Reinforced Epoxy Composite Pipes," Adv. Compos. Mater., **24**(1), pp. 1–16.

[88] Carraro, P. A., Zappalorto, M., and Quaresimin, M., 2016, "Health Monitoring of Cross-Ply Laminates: Modelling the Correlation between Damage Evolution and Electrical Resistance Change," Compos. Part Appl. Sci. Manuf., **82**, pp. 151–158.

[89] Scott, A. E., Mavrogordato, M., Wright, P., Sinclair, I., and Spearing, S. M., 2011, "In Situ Fibre Fracture Measurement in Carbon–epoxy Laminates Using High Resolution Computed Tomography," Compos. Sci. Technol., **71**(12), pp. 1471–1477.

[90] Hu, Y., Kar, N. K., and Nutt, S. R., 2015, "Transverse Compression Failure of Unidirectional Composites," Polym. Compos., **36**(4), pp. 756–766.

[91] Tsai, S. W., and Wu, E. M., 1971, "A General Theory of Strength for Anisotropic Materials," J. Compos. Mater., **5**(1), pp. 58–80.

[92] Hashin, Z., and Rotem, A., 1973, "A Fatigue Failure Criterion for Fiber Reinforced Materials," J. Compos. Mater., **7**(4), pp. 448–464.

[93] Puck, A., 1998, "FAILURE ANALYSIS OF FRP LAMINATES BY MEANS OF PHYSICALLY BASED PHENOMENOLOGICAL MODELS," Compos. Sci. Technol., **58**(7), pp. 1045–1067.

[94] L. Ribeiro, M., Afonso Agélico, R., de Medeiros, R., and Tita, V., 2013, "Finite Element Analyses of Low Velocity Impact on Thin Composite Disks," Int. J. Compos. Mater., **3**(6B), pp. 59–70.

[95] Läufer, J., Becker, V., and Wagner, W., 2017, "Gradient Enhancement of a Transversely Isotropic Continuum Damage Model," Compos. Struct., **181**, pp. 138–144.

Appendix A – Material Data Sheets

composite materials italy

Composite Materials (Italy) s.r.l. – Socio Unico
Via Quasimodo, 33 – 20025 Legnano (MI) ITALY
Phone: +39 0331.467.555
Fax: +39 0331.467.777
E-mail: info@composite-materials.it
www.composite-materials.it

UE 400 REM 38% 100CM

PROPERTIES

Dry Fabric:	*Unit*	*Typical Values*
Carbon Fiber	-	E glass
Fiber Density	g/cm^3	2.55
Nominal Fiber Areal Weigth	g/m^2	400
Uncured Prepreg:	***Unit***	***Typical Values***
Out life @ 23°C	days	30
Storage life @ -18°C	months	12
Nominal Area weight	g/m^2	645
Nominal Resin content	Wt %	38 (± 3)
Volatile content	Wt %	< 1
Nominal Width	mm	1000
Cured Ply Thickness *	mm	0.36
Tack	-	medium

(*) The tests were carried out @ 23°C and 60% R.H. on specimens cured in std conditions (dwell @125° for 60 minutes in autoclave. External pressure applied: 3 bar).

composite materials italy

Composite Materials (Italy) s.r.l. – Socio Unico
Via Quasimodo, 33 – 20025 Legnano (MI) ITALY
Phone: +39 0331.467.555
Fax: +39 0331.467.777
E-mail: info@composite-materials.it
www.composite-materials.it

EE 106 REM 40% 110CM

PROPERTIES

Dry Fabric:	*Unit*	*Typical Values*
Weaving Style	-	Crowsfoot Satin
Glass Fiber	-	E glass
Warp	threads/cm	24
Weft	threads/cm	23
Areal Weight	g/m^2	106 (± 4%)
Uncured Prepreg	***Unit***	***Typical Values***
Out Life @ 23°C	days	30
Storage Life @ -18°C	months	12
Nominal Area Weight	g/m^2	177
Nominal Resin Content	Wt %	40 (± 3)
Volatile Content	Wt %	< 1
Flow after 15 min @125°C, 3 bar	Wt %	17 ± 5
Nominal Width	mm	1100
Tack	-	Low
Cured Material Properties (*)	***Unit***	***Typical Value***
Cured Ply Thickness	mm	0.10

(*) The tests were carried out @ 23°C and 60% R.H. on specimens cured in std conditions (dwell @125° for 1 hour in autoclave. External pressure applied: 3 bar).

www.composite-materials.it

REM
EPOXY MATRIX

GENERAL FEATURES

REM a general use epoxy matrix, suitable to impregnate carbon, glass fabric and unidirectional. It can be processed both by hot press and autoclave cure.

MAIN CHARACTERISTICS

- Maximum Tg of 125°C (257°F).
- Suitable to impregnate a very wide range of support (UD, fabrics and multi-axial - carbon, glass, aramid and hybrids).
- Versatile in different manufacturing process and wide range of temperatures.

QUICK REFERENCE TIPS

It is suggested to vent the vacuum in autoclave process according to the curing cycle shown in the following pages in order to get the highest mechanical behaviour and to avoid both irregularities and pin holes on the surface.

The REM series is available in the following variants:

- **REMT**: higher viscosity for fabric prepregs
- **EU334**: modified tack, for high modulus fiber unidirectional prepreg
- **EU340**: higher viscosity
- **EU432**: modified tack for high modulus fiber unidirectional prepreg and low resin content

OPERATIONAL INSTRUCTIONS

CURE PROCESS RECOMMENDATIONS

This epoxy matrix system can be processed under a very wide range of temperature*. Just as indication, see below curing cycle:

Temperature °C (°F)	Time	Tg °C (°F) DSC	Tg °C (°F) E' DMA
125 (257)	60'	125 (257)	132.5 (271)

**Personalized cure cycle can be developed with CIT Technical Department, in order to fulfil customer manufacturing process optimization.*

AUTOCLAVE

Once determined the processing temperature and corresponding cure time, use these processing parameters in the following cure cycle:

Step	Temperature °C (°F)	Time (min)	Heating rate to isothermal °C/min (°F/min)	Pressure bar (psi)
1	25 (77)	–	–	Vacuum -0.8 (-11.6)
2	125 (257)	–	1÷3 (1.8÷5.4)	3÷7 (43÷102)
3	125 (257)	60	–	3÷7 (43÷102)
4	70 (158)	–	3÷5 (5.4÷9.0)	3÷7 (43÷102)
5	25 (77)	–	–	–

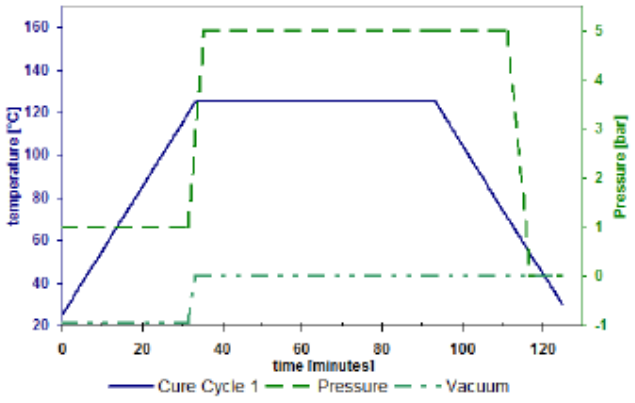

RESIN MATRIX

GENERAL PROPERTIES

Property	Unit	Value	Standard
Storage life @ -18°C (0°F)	months	12	
Out life @ 23°C (73°F)	days	30	
Prepreg volatiles	%wt	<1	ASTM D3530-97R03
Cured resin density	g/cm³	1.20	ASTM D792-00
Tg (DSC)	°C (°F)	125 (257)	ASTM D3418-03
Tg E' (DMA)*	°C (°F)	115 (257)	ASTM E1640-09
Tg Peak Tan δ (DMA)*	°C (°F)	132,5 (270,5)	ASTM E1640-09
Tack		medium	
Elastic Modulus	GPa	3.36	ASTM D790-03

*Laminate Fully Cured 60'@125°C

THERMO-MECHANICAL DMA ANALYSIS

DMA trace of REM laminate cured for 60' @ 125°C.

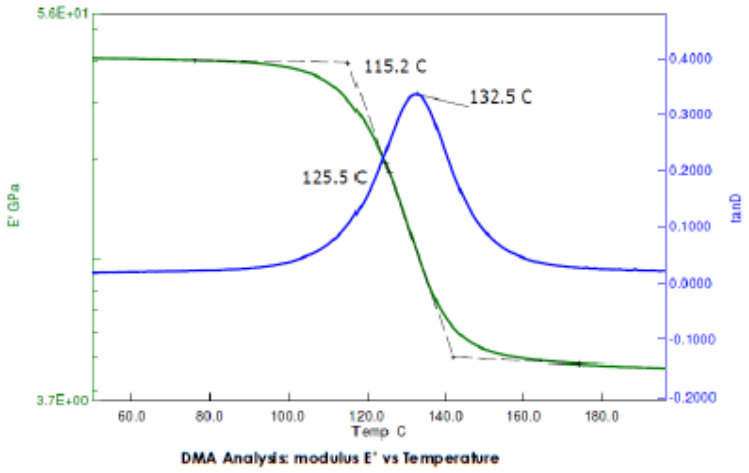

DMA Analysis: modulus E' vs Temperature

Modulus E' evaluated under 2°C/min heating rate, 1Hz oscillating frequency.

VISCOSITY PROFILE

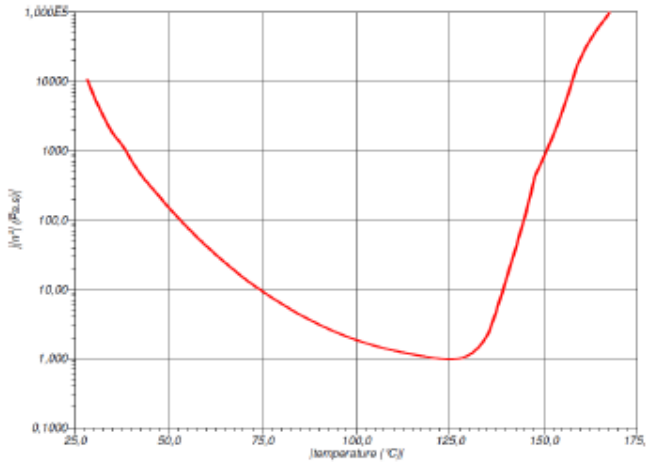

Viscosity profile: temperature vs complex viscosity

Resin complex viscosity is measured under 3°C/min heating rate, 1 Hz oscillating frequency.

GEL TIME

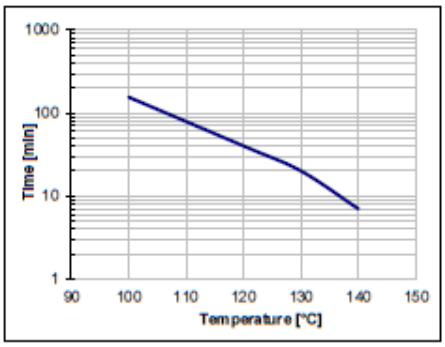

Temperature °C (°F)	Gel Time (min)
100 (212)	155
120 (248)	40
130 (266)	20
140 (284)	7

www.composite-materials.it

CURED PREPREG

Test carried out on a UD REM TAPE – 12KT700 Carbon Fiber at 36%wt resin content (54% fiber volume). Values are then normalized to 60% F.V.

Cured Material Property	Unit	Value Actual 54%F.V.	Value Normalized 60%F.V.	Standard
Tensile Modulus	GPa (Msi)	123 (17.8)	136 (19.8)	ASTM D3039-00
Tensile Strength	MPa (ksi)	2294 (333)	2549 (370)	
Poisson's ratio	–	0.34	–	
Flexural Modulus	GPa (Msi)	134 (19.5)	149 (21.7)	ASTM D790-03
Flexural Strength	MPa (ksi)	1857 (269)	2063 (299)	
Interlaminar Shear Strength	MPa (ksi)	81.5 (11.8)	–	ASTM D2344-00
Interlaminar Fracture Toughness G_{IC}	J/m^2 ($lb\text{-}in/in^2$)	800 (4.57)	–	ASTM D5528-01

(*) at 5% calculated shear strain

www.composite-materials.it

SAFETY CONSIDERATIONS

- This product contains epoxy resin.
- May cause allergic reaction.
- Avoid prolonged contact with skin.
- The use of latex gloves for handling is suggested.
- It is also suggested to work in an aerated environment.
- Scraps are to be cured and discarded following national law.

Note: For further information check the Material Safety Data Sheet.

DELIVERY FORM AND PACKAGING

Custom widths, roll size, and packaging are available on request.

Prepreg fabrics: Supplied on 75 mm (3") diameter cardboard cores with release paper on one side and polyethylene film separator on the other side. Rolls are sealed plastic bags and packed in cardboard boxes.

Standard width: 100 cm (39.4") or 127 cm (50").

Standard length: 50 m (54.7 In yds).

Unidirectional Prepreg: Supplied on 300 mm (12") diameter cardboard cores with release paper on one side and smooth polyethylene film separator on the other side. Rolls are sealed in plastic bags and packed in cardboard boxes.

Standard width: 60cm (23.6"), range from 30cm (11.8") up to 105cm (41.3")
Standard length: 100 m (109 In yds).

HANDLING AND CONDITIONING

- Stock rolls at -18 °C, sealed in original packages.
- Shop life at 23°C refers to rolls sealed in original packages.
- Before the use of the prepreg, get out the roll from the freezer and let it warm up to room temperature for 6 hours sealed in its original package.

IMPORTANT NOTICE:

The data and statements supplied in this datasheet are met to provide an overview of this product and its properties. Users should perform their own verification and testing to determine suitability of this material for their specific end use applications. NO WARRANTY OF FITNESS FOR A PARTICULAR PURPOSE IS EXPRESSED OR IMPLIED. Nothing herein is to be taken as permission to practice any patented invention without a licence.

Toray Group
Composite Materials (Italy) s.r.l. - Socio Unico
Via Quasimodo, 33 - 20025 Legnano (MI) ITALY
Capitale Sociale € 100.000 I.V. - R.E.A. MI n° 2052698
Iscrizione Registro Imprese C. F. n° 08844870967
P.IVA IT08844870967
Phone: +39 0331.467.555 • Fax: +39 0331.467.777
E-mail: info@composite-materials.it
www.composite-materials.it